

**Cu(I) complexes – Thermally activated delayed fluorescence.  
Photophysical approach and material design**

Rafał Czerwieniec, Markus J. Leitzl, Herbert H. H. Homeier, and Hartmut Yersin

Universität Regensburg, Institut für Physikalische Chemie,  
Universitätstr. 31, D-93040 Regensburg, Germany

*Coordination Chemistry Reviews* 325 (2016) 2–28  
<http://dx.doi.org/10.1016/j.ccr.2016.06.016>

This project has received funding from the European Union's Horizon 2020 research and innovation programme under the Marie Skłodowska-Curie grant agreement No. 645628

**Project Number:** 645628

**Project Acronym:** METCOPH

**Project title:** Metallocomplexes of macrocyclic compounds for photonic devices



# Cu(I) complexes – Thermally activated delayed fluorescence. Photophysical approach and material design

Rafał Czerwieniec<sup>a</sup>, Markus J. Leitl<sup>a</sup>, Herbert H. H. Homeier, and Hartmut Yersin\*

## Dedication

Dedicated to Dr. Tobias Fischer, a former member of our research group, an excellent young scientist, and a friend who passed away too early in August 2015.

## Abstract

Cu(I) complexes often show transitions of distinct metal-to-ligand charge transfer (MLCT) character. This can lead to small energy separations between the lowest singlet  $S_1$  and triplet  $T_1$  state. Hence, thermally activated delayed fluorescence (TADF) and, if applied to electroluminescent devices, *singlet harvesting* can become highly effective. In this contribution, we introduce the TADF mechanism and identify crucial parameters that are necessary to optimize materials' properties, in particular, with respect to short emission decay times and high quantum yields at ambient temperature. In different case studies, we present a photophysical background for a deeper understanding of the materials' properties. Accordingly, we elucidate strategies for obtaining high quantum yields. These are mainly based on enhancing the intrinsic rigidity of the complexes and of their environment. Efficient TADF essentially requires small energy separations  $\Delta E(S_1-T_1)$  with preference below about  $1000 \text{ cm}^{-1}$  ( $\approx 120 \text{ meV}$ ). This is achievable with complexes that exhibit small spatial HOMO-LUMO overlap. Thus, energy separations below  $300 \text{ cm}^{-1}$  ( $\approx 37 \text{ meV}$ ) are obtained, giving short radiative TADF decay times of less than  $5 \mu\text{s}$ . In a case study, it is shown that the TADF properties may be tuned or the TADF effect can even be turned off. However, very small  $\Delta E(S_1-T_1)$  energy separations are related to small radiative rates or small

oscillator strengths of the  $S_1 \rightarrow S_0$  transitions due to the (required) small HOMO-LUMO overlap, as discussed in a further case study. In this respect, large spin-orbit coupling (SOC) of the triplet state to higher lying singlet states can induce an additional phosphorescence decay path that leads to a luminescence consisting of TADF and phosphorescence, thus representing a combined singlet harvesting and triplet harvesting mechanism. This gives an overall reduction of the decay time. Finally, in a strongly simplified model, the SOC efficiency is traced back to easily obtainable results from DFT calculations.

## 1. Introduction

The potential use of Cu(I) complexes for commercial applications, especially, in the fields of light generation by electroluminescence, such as organic light emitting diodes (OLEDs) [1-6] and light emitting electrochemical cells (LEECs) [7-12], as well as in the areas of sensing of oxygen or temperature [13-19] and as photocatalysts [20-26] strongly stimulated scientific and fundamental research in recent years. This did not only lead to a much deeper understanding of photophysical and chemical properties of the Cu(I) compounds, but led also to the development of an enormous number of new materials with strongly improved properties, for example, with respect to an application as OLED emitters. [5,27-43] Moreover, material design strategies could be developed for engineering of highly efficient emitters and even new emission mechanisms could be proposed [44,45].

For OLED emitters, it is crucial that all generated singlet and triplet excitons are harvested and transferred into light. Almost two decades ago, it was recognized that third row transition metal complexes, in particular, with Ir(III), Pt(II), and Os(II) central metal ions, are well suited for such processes. [1-5 46-56] This is a consequence of

efficient spin-orbit coupling (SOC) between the lowest triplet state and higher lying singlet states [1-4,46,47,57]. In particular, SOC induces fast intersystem crossing (ISC) to the lowest triplet state (order of several tenths of fs [58,59]) and can lead to relatively high radiative rates of transitions from the triplet state to the singlet ground state for otherwise spin-forbidden transitions. Thus, rates of the order of  $10^5 \text{ s}^{-1}$  become possible. [1,2,4,60] Accordingly, these materials are called triplet emitters. It is of particular importance that, when these triplet emitters are applied in OLEDs, all singlet and triplet excitons can be harvested in the lowest triplet state. Hence, this mechanism is denoted as *triplet harvesting effect* [46, 55]. With these emitter materials, such as  $\text{Ir}(\text{ppy})_3$  (with ppy = 2-phenylpyridinate) and many related complexes, almost 100 % internal quantum efficiencies could be obtained. [49,53]

However, these triplet emitters are based on high-cost precious metals. This may become a crucial factor, when OLED lighting goes into mass production. [4,61,62] Therefore, alternative materials, such as Cu(I) complexes [2-6,27,29-41,43-45,61,63-92] or purely organic molecules [92-107] came into the focus of research. In the scope of this work, we will concentrate on Cu(I) compounds.

At first glance, Cu(I) complexes seem to show substantial photophysical problems with respect to OLED applications: (i) Compared to iridium, the 1st row transition metal copper induces much weaker spin-orbit coupling [108]. As a consequence, transitions between the excited triplet state and the singlet ground state are largely forbidden. Thus, long phosphorescence decay times of several 100  $\mu\text{s}$  up to a few ms are frequently found [2,4,5,17,38,61,65,67,69,73,109-111]. With such long decay times, OLEDs would suffer from strong saturation effects and photochemical reactions that may become significant in reducing the device stability [112-115]. (ii) After the

electronic excitation, Cu(I) complexes often display flattening distortions of the molecular structure. [116-125] Such rearrangements are usually connected with an increase of non-radiative deactivation or even quenching of the emission due to a strong increase of the Franck-Condon factors of the low-lying vibrational modes of the excited state and the highly excited vibrational modes of the electronic ground state [126-128]. However, these shortcomings may largely be suppressed by optimizing properties of the thermally activated delayed fluorescence (TADF) (introduced in section 2 and discussed in detail in section 4) and by designing relatively rigid molecular structures, as will be addressed in section 3. We will focus in this contribution on corresponding optimization strategies being illustrated by case studies. It will further be shown that the TADF behavior, being strongly dependent on the energy separation between the lowest singlet and triplet state, can be varied over a very large range by chemical “tuning” (section 4). In this respect, we will discuss in section 5 a correlation existing for charge transfer states between this energy separation and the allowedness of the transition from the thermally activated singlet state to the electronic ground state. By further case studies in sections 6 and 7, it will be demonstrated that SOC can strongly influence the emission behavior of the complexes. In these case studies, we will analyze corresponding SOC paths and uncover strategies to improve the material's emission properties resulting in a combined singlet harvesting and triplet harvesting mechanism.

## **2. Thermally activated delayed fluorescence and singlet harvesting**

The TADF mechanism represents a molecular property that was initially described based on the emission behavior of eosin. Therefore, the observed delayed fluorescence was originally denoted as E-type (eosin-type) fluorescence.[129,130] By

use of Figure 1, this effect is illustrated for Cu(I) complexes. Let us first discuss an optical excitation process. For example, an energetically higher lying singlet state is excited. Subsequently, a very fast internal conversion (IC) to the  $S_1$  state of the order of  $10^{-12}$  s [126,131,132] takes place (not shown in the diagram). ISC ( $S_1 \rightarrow T_1$ ) is also very effective and relatively short  $\tau(\text{ISC})$  times, lying between approximately 3 and 30 ps depending on the individual Cu(I) complex and its local environment [81,120,123,124,133], have been reported. Accordingly, a significant prompt fluorescence ( $S_1 \rightarrow S_0$ ) is not detected [4,5,44,45,61,65,67-72], but a very bright long-lived phosphorescence ( $T_1 \rightarrow S_0$ ) is frequently observed at low temperature.

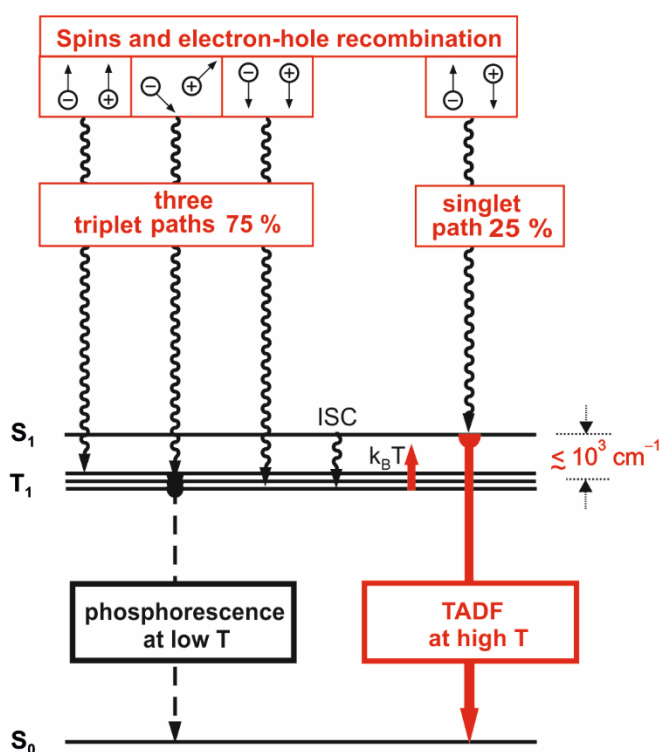


**Fig. 1** Schematic diagram to illustrate the molecular mechanism of thermally activated delayed fluorescence (TADF) and the singlet harvesting mechanism occurring in OLEDs. [2,4] Note that the triplet state  $T_1$ , consisting of three substates, is slightly split, mostly of less than  $1\text{-}2 \text{ cm}^{-1}$  but in a special case even  $15 \text{ cm}^{-1}$ . [44]  $k_B$  = Boltzmann constant,  $T$  = temperature. (For details, see sections 4 and 6).

With temperature increase, the  $S_1$  state can be populated depending on the thermal energy that is available according to  $k_B T$  ( $\approx 210 \text{ cm}^{-1}$  at  $T = 300 \text{ K}$ ,  $26 \text{ meV}$ ) and the energy separation  $\Delta E(S_1-T_1)$ . In a situation of a fast equilibration – as usually realized in Cu(I) complexes above  $T \approx 15 \text{ K}$  [4,5,44,45,61,63,68-72] – population of the higher lying state is governed by a Boltzmann distribution, whereby “fast” means that the thermal equilibration is faster than all emission processes. (See also below in this section.) As a consequence of this process of up-ISC (or reverse ISC, RISC) and the (mostly) relatively short-lived  $S_1$  state, the  $T_1$  state can efficiently be depopulated at higher temperature and a strongly dominating  $S_1$  fluorescence can be observed. Since the population of the  $S_1$  state is fed from the long-lived triplet reservoir, this type of fluorescence is also long-lived. Hence, this emission is denoted as thermally activated delayed fluorescence.<sup>1</sup> It is remarked that the energy separation  $\Delta E(S_1-T_1)$  strongly governs the TADF properties. Although the  $\Delta E(S_1-T_1)$  value for eosin is as large as  $\approx 10 \text{ kcal/mol}$  ( $\approx 3500 \text{ cm}^{-1}$ ;  $\approx 0.43 \text{ eV}$ ) [130] one still detects TADF. However, for practical use of TADF compounds in OLEDs,  $\Delta E(S_1-T_1)$  values should be much smaller and – to give the reader a rough orientation – should not exceed considerably  $10^3 \text{ cm}^{-1}$  ( $0.12 \text{ eV}$ ). A number of examples are presented below.

In an OLED device, the excitation occurs after electron-hole recombination. In this process, 75 % triplet and 25 % singlet excitons are formed [46,47,55,134]. Thus, one singlet path and three triplet paths populate the  $S_1$  and the  $T_1$  state, respectively. [55] Subsequently, fast thermal equilibration processes, governed by the Boltzmann distribution, occur. Owing to the fact that in most cases the singlet state  $S_1$  decays much faster than the  $T_1$  state, the triplet state is frequently not efficiently emitting at ambient temperature. In this situation, almost all excitations are transferred to or

---

<sup>1</sup> For several novel complexes also a phosphorescence decay path is observed, leading to a combined TADF and phosphorescence at ambient temperature (see sections 4.2 and 6).

harvested in the singlet state  $S_1$ , which then can show efficient TADF. Hence, the TADF effect for an electro-luminescent device has been denoted as *singlet harvesting effect*. [2-5,32, 44,45,61,65,68,69,71-73,87,88,92,135] (Compare footnote 1.)

For OLED use, the TADF decay time  $\tau(\text{TADF})$  is crucial and should be as short as possible, obviously at high emission quantum yields. This is required to minimize, for example, saturation and annihilation effects and triplet-polaron quenching causing a roll-off of the OLED efficiency with increasing current density [112-115,136-138], and photochemical reactions in reactive excited states. The overall decay time  $\tau(T)$  of a molecular system with two excited states that are thermally equilibrated is determined by a Boltzmann-like relation<sup>2</sup> [2,3,5,38,44,45,61,65]. Compare also Refs. [139-141].

$$\tau(T) = \frac{3 + \exp[-\Delta E(S_1 - T_1)/(k_B T)]}{3/\tau(T_1) + [1/\tau(S_1)]\exp[-\Delta E(S_1 - T_1)/(k_B T)]} \quad (1)$$

Herein,  $\tau(S_1)$  and  $\tau(T_1)$  represent the singlet state and the triplet state decay times, respectively, and  $\Delta E(S_1 - T_1)$  is the energy separation between these states. At very low temperature, the exponential terms disappear and the measured decay time  $\tau(T)$  equals the phosphorescence decay time  $\tau(T_1)$ , while at high temperature (and long  $\tau(T_1)$ ) the term containing  $\tau(T_1)$  can be neglected and one essentially obtains the decay time of the thermally activated delayed fluorescence  $\tau(\text{TADF})$ . Examples (and exceptions) are discussed below.

The emission decay time as expressed by eq. (1) depends on three parameters that are determined by the individual emitter compound (and its environment). A short

---

<sup>2</sup> It is assumed that all molecular parameters  $\tau(T_1)$ ,  $\tau(S_1)$ , and  $\Delta E(S_1 - T_1)$  are temperature independent. Further, as taken into account, the triplet state consists of three substates, mostly of essentially the same energy.



discussion of these parameters is illustrative and, as shown below, can help in designing suitable TADF emitters:

### $\Delta E(S_1-T_1)$

The energy separation between the lowest singlet and triplet excited state is crucial and should be as small as possible. For this situation, Cu(I) complexes are well suited, since they frequently exhibit low-lying metal-to-ligand charge transfer (MLCT) states of  $^3\text{MLCT}$  and  $^1\text{MLCT}$  character. In this situation, a distinct charge separation between excited and non-excited electron occurs. As a consequence, the quantum mechanical exchange interaction [142] [143, p. 86] and hence, also the singlet-triplet splitting becomes small. For example, in section 4, we will investigate the resulting properties in detail. Moreover, in section 5 we will point to a relation that exists between  $\Delta E(S_1-T_1)$  and the allowedness of the  $S_1 \leftrightarrow S_0$  transition or the  $S_1$  decay rate.

### $\tau(S_1)$

The  $S_1 \leftrightarrow S_0$  allowedness, displayed, for example, by the (radiative) fluorescence decay time  $\tau(S_1)$  should be as short as possible. However, for most materials investigated so far, a short  $\tau(S_1)$  time is related to a large  $\Delta E(S_1-T_1)$  value. This is not a favorable situation and therefore, special efforts are required to overcome this shortcoming. (Compare the discussion in sections 5 and 6.)

### $\tau(T_1)$

The (radiative) emission decay time of the triplet state should also be “tuned” to be as short as possible. In this way, an effective radiative decay channel can be opened in addition to the TADF path. To achieve this aim, SOC of the  $T_1$  state to higher lying

singlet states should be enhanced. Based on case studies (sections 4.2 and 6), we will show that this can be realized. [44,45]

For completeness, it is remarked that application of eq. (1) to decay time data measured at different temperatures opens experimental access to all the parameters discussed above. In particular, it becomes possible to detect energy separations that are much smaller than the spectral resolution accessible for a given compound. For example, energy separations between states being as small as only a few  $\text{cm}^{-1}$  can be resolved despite the MLCT emission bands being as broad as several thousand  $\text{cm}^{-1}$ . (Compare sections 4 and 6 and refs. [2,4,5,139-141])

The amount of the energy separation  $\Delta E(S_1-T_1)$  has a particularly strong impact on the emission properties of the TADF materials. Accordingly, this feature represents one of the main topics of this study. Thus, compounds discussed in this contribution are classified according to their  $\Delta E(S_1-T_1)$  values (Figure 2). In the different case studies, we will refer to these materials and use them as examples for discussion of different aspects of their photophysical behavior. In Table 1, we summarize the compounds, their abbreviations, and the experimentally determined  $\Delta E(S_1-T_1)$  values.

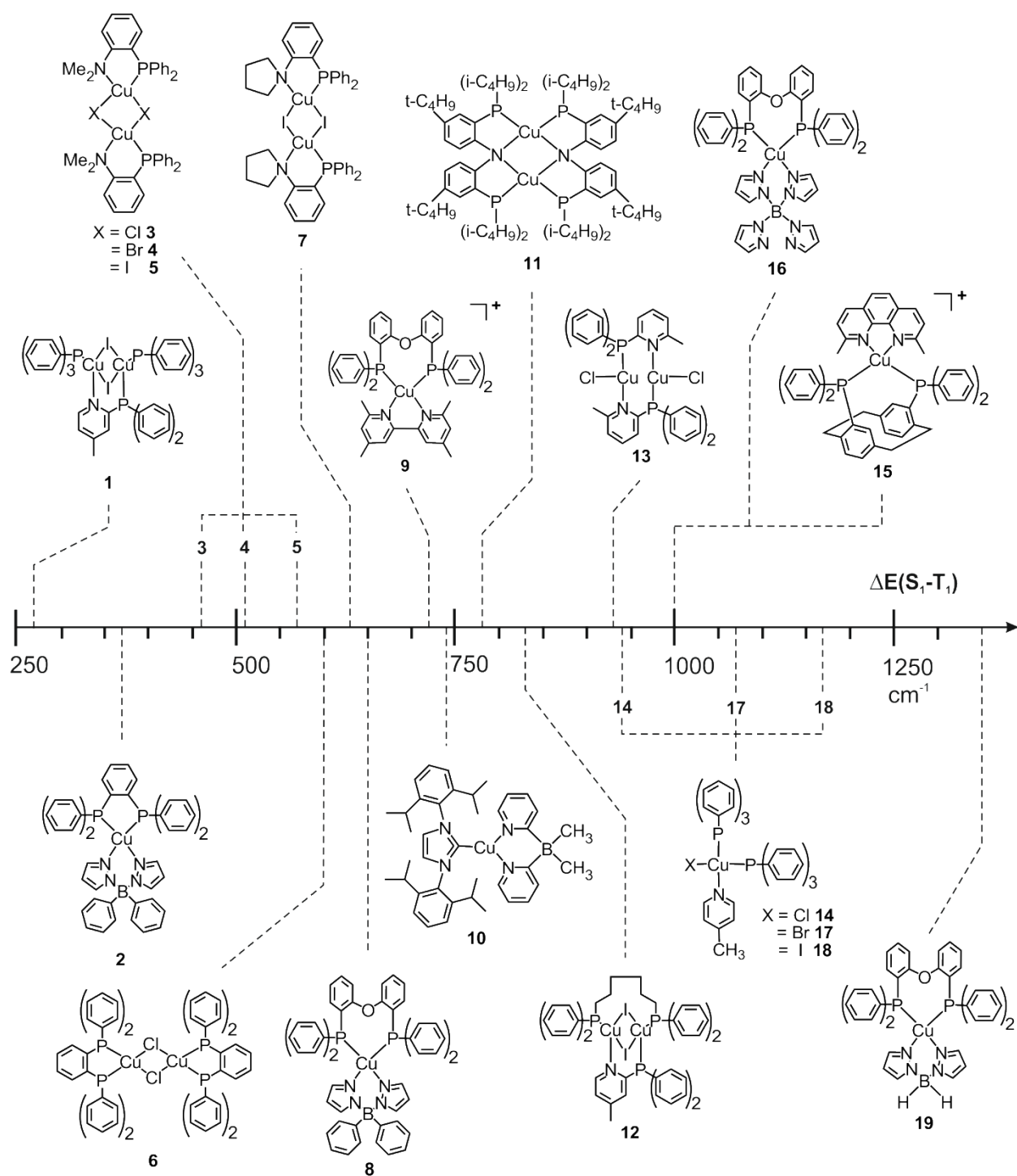


**Fig. 2:** Chemical structures of the TADF compounds discussed in this contribution. They are arranged according to the energy separations between the lowest singlet  $S_1$  and triplet  $T_1$  state  $\Delta E(S_1-T_1)$ . These states are essentially of  ${}^1\text{MLCT}$  and  ${}^3\text{MLCT}$  character, respectively. Related abbreviations of the compounds and the values of  $\Delta E(S_1-T_1)$  are given in Table 1.

**Table 1** Cu(I) compounds and singlet-triplet energy separations. The related chemical structures are displayed in Figure 2.

	Compound	$\Delta E(S_1-T_1)$ [cm <sup>-1</sup> ]	Ref.
1	Cu <sub>2</sub> I <sub>2</sub> [MePyrPHOS)(PPh <sub>3</sub> ) <sub>2</sub>	270	[5, 29]
2	Cu(dppb)(pz <sub>2</sub> Bph <sub>2</sub> )	370	[34, 67, 144]
3	[Cu( $\mu$ -Cl)(PNMe <sub>2</sub> ) <sub>2</sub> ]	460	[73]
4	[Cu( $\mu$ -Br)(PNMe <sub>2</sub> ) <sub>2</sub> ]	510	[73]
5	[Cu( $\mu$ -I)(PNMe <sub>2</sub> ) <sub>2</sub> ]	570	[73]
6	Cu <sub>2</sub> Cl <sub>2</sub> (dppb) <sub>2</sub>	600	[69, 78]
7	[Cu( $\mu$ -I)(PNpy)] <sub>2</sub>	630	[73]
8	Cu(pop)(pz <sub>2</sub> Bph <sub>2</sub> )	650	[2, 65, 68, 147]
9	Cu(tmbpy)(pop) <sup>+</sup>	720	[72]
10	(IPr)Cu(py <sub>2</sub> -BMe <sub>2</sub> )	740	[45, 66]
11	[Cu(PNP <sup>t</sup> Bu)] <sub>2</sub>	786	[38]
12	Cu <sub>2</sub> I <sub>2</sub> (MePyrPHOS)(dpph)	830	[5, 32]
13	Cu <sub>2</sub> Cl <sub>2</sub> (N <sup>^</sup> P) <sub>2</sub>	930	[44, 145]
14	CuCl(PPh <sub>3</sub> ) <sub>2</sub> (4-Mepy)	940	[74]
15	Cu(dmp)(phanephos) <sup>+</sup>	1000	[61, 146]
16	Cu(pop)(pz <sub>4</sub> B)	1000	[65, 147]
17	CuBr(PPh <sub>3</sub> ) <sub>2</sub> (4-Mepy)	1070	[74]
18	CuI(PPh <sub>3</sub> ) <sub>2</sub> (4-Mepy)	1170	[74]
19	Cu(pop)(pz <sub>2</sub> BH <sub>2</sub> )	1300	[4, 65, 147]

### 3. Controlling of excited state distortions as a strategy for designing strongly emissive materials

MLCT excitations promote significant geometry reorganizations of the excited molecules with respect to the geometries of the electronic ground states. In particular, in copper(I) complexes flattening deformations [116,119,120,123,124,148] occur, which have been identified as the main mechanism responsible for non-radiative relaxations to the ground state and, thus, the main reason for emission quenching. For many bis-diimine complexes, it was demonstrated that a judicious use of sterically demanding ligands can partly block such excited-state reorganizations and, thus, reduce subsequent undesired quenching. This leads to an increase of the emission quantum yield. [38,61,65, 72,109,122,149,153] In this section, we present two case studies discussing neutral and cationic copper(I) complexes and exemplifying the validity of this strategy for chemical engineering of strongly emissive TADF materials.

The charge-transfer character of the lowest excited states of the complexes can be easily elucidated by inspection of their frontier orbitals resulting from DFT calculations, as shown in Figure 3 for Cu(pop)(pz<sub>2</sub>Bph<sub>2</sub>) **8** (with pop = bis[(2-diphenylphosphino)phenyl] ether and pz<sub>2</sub>Bph<sub>2</sub> = diphenylbis(pyrazolyl)borate)). HOMO and LUMO, calculated for the optimized ground-state geometry, exhibit distinctly different spatial distributions within the molecule. The HOMO consists of a copper 3d atomic orbital perturbed by bonding with the phosphorus and nitrogen atoms. The LUMO represents a π\* orbital of the pop ligand. The low-energy transitions resulting from TD-DFT computations S<sub>1</sub> ↔ S<sub>0</sub> and T<sub>1</sub> ↔ S<sub>0</sub> are dominated by the HOMO → LUMO one-electron excitation. Therefore, the lowest singlet and triplet excited states are assigned to be of metal-to-ligand charge-transfer (MLCT, dπ\*) character with S<sub>1</sub> = <sup>1</sup>MLCT and T<sub>1</sub> = <sup>3</sup>MLCT. For this complex, the chromophoric ligand is the pop ligand, while the bispyrazolyl ligand pz<sub>2</sub>Bph<sub>2</sub> is involved only to a small extent. [65]

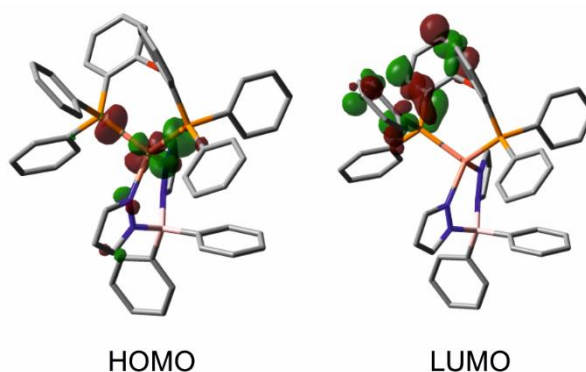


**Fig. 3.** Highest occupied molecular orbital (HOMO) and lowest unoccupied molecular orbital (LUMO) of Cu(pop)(pz<sub>2</sub>Bph<sub>2</sub>) **8** displayed for the DFT-optimized ground state (S<sub>0</sub>) geometry. Calculations were performed on the B3LYP/def2-svp [150,151] level of theory. Hydrogen atoms are omitted for clarity. [65]

Figure 4 shows emission spectra of Cu(pop)(pz<sub>2</sub>Bph<sub>2</sub>) **8** and Cu(pop)(pz<sub>2</sub>BH<sub>2</sub>) **19** (pz<sub>2</sub>BH<sub>2</sub> = bis(1-pyrazolyl)borate) measured at ambient temperature in different

environments: as powders, doped in polymer (PMMA) films, and dissolved in dichloromethane. Independent of the matrix, the emission spectra are broad and unstructured (even down to cryogenic temperatures, e.g. 1.6 K). [65] This is in accordance with the MLCT nature of the emitting state. The spectral positions of these emissions depend on the environment. In powder and in PMMA blue to white-blue emissions are observed with band maxima at 464 and 466 nm, respectively, for **8** and 436 and 462 nm for **19**, whereas in CH<sub>2</sub>Cl<sub>2</sub>, the emissions are significantly shifted to longer wavelengths and are centered at 498 nm (Cu(pop)(pz<sub>2</sub>Bph<sub>2</sub>) **8**, green) and 535 nm (Cu(pop)(pz<sub>2</sub>BH<sub>2</sub>) **19**, yellow), respectively. The bandwidths of the powder spectra are slightly smaller than in PMMA and in CH<sub>2</sub>Cl<sub>2</sub>. These effects indicate the importance of solute-solvent or dopant-matrix interactions.

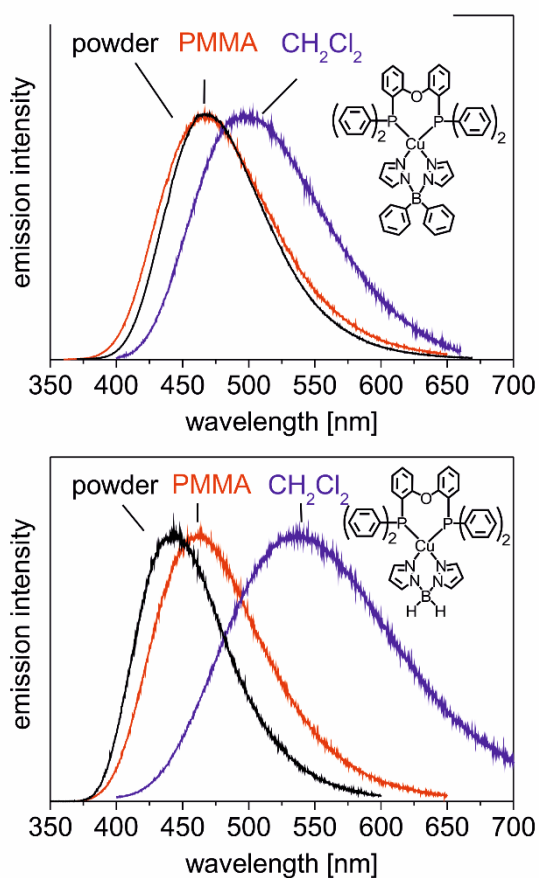


**Fig. 4.** Ambient-temperature luminescence spectra (normalized) of Cu(pop)(pz<sub>2</sub>Bph<sub>2</sub>) **8** and Cu(pop)(pz<sub>2</sub>BH<sub>2</sub>) **19** measured for powder samples (black), in poly(methyl

methacrylate) (PMMA) polymer films (blue), and in degassed dichloromethane solutions (green lines), respectively. Adapted with permission from [65]. Copyright (2011) American Chemical Society.

Both complexes are strongly emissive in the solid phase (powder) and in polymer films. The quantum yields determined for Cu(pop)(pz<sub>2</sub>Bph<sub>2</sub>) (**8**) are  $\phi_{\text{PL}} = 90\%$  (powder) and 41 % (PMMA), and for Cu(pop)(pz<sub>2</sub>BH<sub>2</sub>) (**19**) 45 % (powder) and 35 % (PMMA), respectively. (Table 2) Thus, in polymer samples, the quantum yields are smaller than in powder samples. A further drop of the quantum yield is observed for liquid solutions. In degassed dichloromethane,  $\phi_{\text{PL}}$  amounts to 8 and 9 % for Cu(pop)(pz<sub>2</sub>Bph<sub>2</sub>) **8** and Cu(pop)(pz<sub>2</sub>BH<sub>2</sub>) **19**, respectively. These drops of  $\phi_{\text{PL}}$  values are accompanied by significant variations of the emission decay times  $\tau$ . For instance, for Cu(pop)(pz<sub>2</sub>Bph<sub>2</sub>) **8**, the emission decay time in CH<sub>2</sub>Cl<sub>2</sub> is about seven times shorter than in powder. Obviously, these strong dependences of  $\phi_{\text{PL}}$  and  $\tau$  on the environment are caused by a distinct change of the nonradiative relaxation rate  $k^{\text{nr}}$ , determined from

$$k^{\text{nr}} = \frac{1 - \phi_{\text{PL}}}{\tau} \quad (2)$$

while going from a rigid situation to a much more flexible liquid solution. (Table 2) The respective  $k^{\text{nr}}$  values determined for Cu(pop)(pz<sub>2</sub>Bph<sub>2</sub>) **8** increase from  $7.7 \cdot 10^3 \text{ s}^{-1}$  (powder) to  $5.1 \cdot 10^5 \text{ s}^{-1}$  (solution). This represents a matrix-related increase of  $k^{\text{nr}}$  by a factor of almost 70. The non-radiative rate  $k^{\text{nr}}$  of Cu(pop)(pz<sub>2</sub>BH<sub>2</sub>) **19** grows in by about 25 times. For comparison, the matrix-related changes of the radiative rates  $k^{\text{r}}$ , calculated as

$$k^{\text{r}} = \frac{\phi_{\text{PL}}}{\tau} \quad (3)$$

are much smaller. The largest observed decrease of  $k^r$  (complex **8**, powder compared to PMMA) is smaller than a factor of four. This effect may be induced by small changes of the TADF properties by polarity differences of the various environments.

An MLCT transition is characterized by a significant electron density shift from the Cu(I) ion, with a  $d^{10}$  configuration, to the ligand. This results in a partial oxidation of the metal. Since for a  $d^9$  configuration, usually a square-planar-like coordination is preferred, a four-fold coordinated Cu(I) complex has the tendency to undergo a flattening distortion. [109,116,120-124]. Such a structural rearrangement results in a shift of the excited state to lower energy. Moreover, non-radiative relaxation processes to the ground state become more efficient due to enhanced vibrational coupling. [126-128] The geometry rearrangement in the excited state occurs most easily in fluid solution, but it is partly hindered in an organic polymer (PMMA) and, even more, in powder samples. Obviously, high local rigidity of the environment cage significantly hinders larger distortions in polymer or crystal. However, minor geometry changes are still possible also in rigid environments (see below).

**Table 2.** Ambient temperature luminescence data for complexes **8** and **19**.  $\lambda_{\max}$  = emission maximum,  $\tau$  = emission decay time, and  $\phi_{\text{PL}}$  = emission quantum yield. The radiative rates  $k^r$  and the nonradiative rates  $k^{\text{nr}}$  were calculated according to the eqs. (3) and (2), respectively. Experimental data from ref. [65].

	Cu(pop)(pz <sub>2</sub> Bph <sub>2</sub> ) <b>8</b>					Cu(pop)(pz <sub>2</sub> BH <sub>2</sub> ) <b>19</b>				
	$\lambda_{\max}$ [nm]	$\tau$ [ $\mu\text{s}$ ]	$\phi_{\text{PL}}$ [%]	$k^r$ [ $\text{s}^{-1}$ ]	$k^{\text{nr}}$ [ $\text{s}^{-1}$ ]	$\lambda_{\max}$ [nm]	$\tau$ [ $\mu\text{s}$ ]	$\phi_{\text{PL}}$ [%]	$k^r$ [ $\text{s}^{-1}$ ]	$k^{\text{nr}}$ [ $\text{s}^{-1}$ ]
powder	464	13	90	$6.9 \cdot 10^4$	$7.7 \cdot 10^3$	436	20	45	$2.3 \cdot 10^4$	$2.8 \cdot 10^4$
PMMA	466	23	41	$1.8 \cdot 10^4$	$2.6 \cdot 10^4$	462	22	35	$1.6 \cdot 10^4$	$3.0 \cdot 10^4$



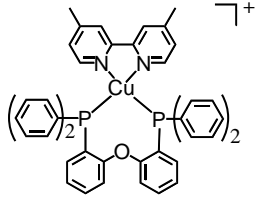
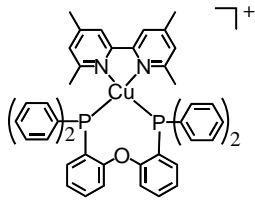
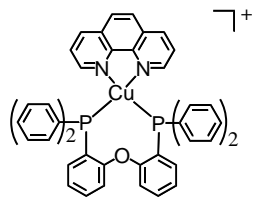
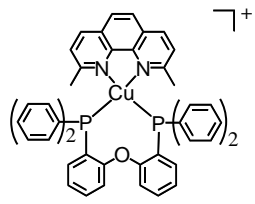
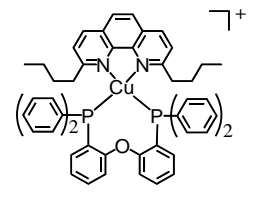
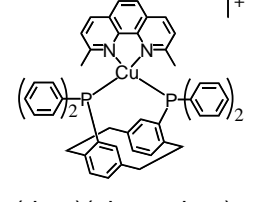
CH<sub>2</sub>Cl<sub>2</sub> 498 1.8 8 4.4 ·10<sup>4</sup> 5.1 ·10<sup>5</sup> 535 1.3 9 6.9 ·10<sup>4</sup> 7.0 ·10<sup>5</sup>

Interestingly, the red shift of the emission, when comparing powder with fluid samples, is almost three times larger for complex **19** ( $\lambda_{\text{max}}$  shifts from 436 to 535 nm,  $\approx 4200 \text{ cm}^{-1}$ ) than that for complex **8** ( $\lambda_{\text{max}}$  shifts from 464 to 498 nm;  $\approx 1500 \text{ cm}^{-1}$ ). Both complexes display the same coordination of the metal ion and have the same chromophoric ligand (pop), but the molecules differ in distant parts (relative to the Cu-pop fragment) of the spectator ligand. Complex **8** displays two phenyl groups of the pz<sub>2</sub>Bph<sub>2</sub> ligand instead of only two hydrogen atoms of pz<sub>2</sub>BH<sub>2</sub>. Thus, the observed differences in the photophysical behavior show that modifications of the molecular structure may significantly influence the luminescence properties of the complex. In the case of complex **8**, the bulky phenyl groups seem to restrict the flexibility of the pz<sub>2</sub>Bph<sub>2</sub> ligand, as compared to the much smaller pz<sub>2</sub>BH<sub>2</sub>. Apparently, the phenyl groups serve as an “internal” rigidification of the molecule, in addition to the effects exerted by the rigid matrix.

Similar trends are observed for cationic heteroleptic Cu(I) complexes displayed in Table 3. Several of these mixed-ligand complexes exhibit intrinsic rigidity due to the steric requirements of the chelating diphosphine and diimine ligands. In particular, the diphosphine ligands pop and phanephos<sup>3</sup> with relatively wide P-Cu-P bite angles form rigid “semicages” for the metal ion coordinated by the second ligand. [61,152-154] Moreover, as can be seen, for instance, for the molecular structure of Cu(dmp)(phanephos)<sup>+</sup> **15**, small aliphatic groups in the 2 and 9 positions of phenanthroline (Figure 5 and Table 3) and the 6 and 6' positions of bipyridine (Table 3, compound **9**) proved to be crucial for “anchoring” of the diimine ligands with the framework provided by the bulky groups of the second ligand.

<sup>3</sup> phanephos = 4,12-bis(diphenylphosphino)-[2.2]-paracyclophane

**Table 3.** Ambient temperature emission data for cationic Cu(I) complexes.  $\lambda_{\max}$  = emission maximum,  $\tau$  = emission decay time, and  $\phi_{\text{PL}}$  = emission quantum yield. The radiative rates  $k^r$  and the non-radiative rates  $k^{\text{nr}}$  were calculated according to eq. (3) and (2), respectively.

Compound	environ- -ment	$\lambda_{\max}$ [nm]	$\tau$ [ $\mu\text{s}$ ]	$\phi_{\text{PL}}$ [%]	$k^r$ [ $\text{s}^{-1}$ ]	$k^{\text{nr}}$ [ $\text{s}^{-1}$ ]	Ref. <sup>a</sup>
 Cu(dmbpy)(pop) <sup>+</sup>	C <sub>2</sub> H <sub>5</sub> OH powder	655 575	0.02 - <sup>b</sup>	<<1 9	- - <sup>b</sup>	5.0·10 <sup>7</sup> - <sup>b</sup>	[72, 158, 159]
 Cu(tmbpy)(pop) <sup>+</sup> <b>9</b>	C <sub>2</sub> H <sub>5</sub> OH powder	575 555	2.5 11	6 55	2.4·10 <sup>4</sup> 5.0·10 <sup>4</sup>	3.8·10 <sup>5</sup> 4.1·10 <sup>4</sup>	[72, 159]
 Cu(phen)(pop) <sup>+</sup>	CH <sub>2</sub> Cl <sub>2</sub>	700	0.19	0.18	9.5·10 <sup>3</sup>	5.3·10 <sup>6</sup>	[8, 26, 27, 89, 153, 155, 156, 157]
 Cu(dmp)(pop) <sup>+</sup>	CH <sub>2</sub> Cl <sub>2</sub> powder	570 538	14 18	15 80	1.1·10 <sup>4</sup> 4.4·10 <sup>4</sup>	6.1·10 <sup>4</sup> 1.1·10 <sup>4</sup>	[68, 153, 156, 157]
 Cu(dbp)(pop) <sup>+</sup>	CH <sub>2</sub> Cl <sub>2</sub>	560	16	16	1.0·10 <sup>4</sup>	5.3·10 <sup>4</sup>	[11, 39, 98, 153, 157]
 Cu(dmp)(phanephos) <sup>+</sup> <b>15</b>	CH <sub>2</sub> Cl <sub>2</sub> PMMA powder	558 535 530	10 20 14	40 65 80	4.0·10 <sup>4</sup> 3.3·10 <sup>4</sup> 5.7·10 <sup>4</sup>	6.0·10 <sup>4</sup> 1.8·10 <sup>4</sup> 1.4·10 <sup>4</sup>	[61, 146]

<sup>a</sup> Citations refer to the compounds.

<sup>b</sup> The emission decay kinetics distinctly deviate from a mono-exponential decay. Therefore, the  $\tau$ ,  $k^r$ , and  $k^{\text{nr}}$  parameters were not determined.

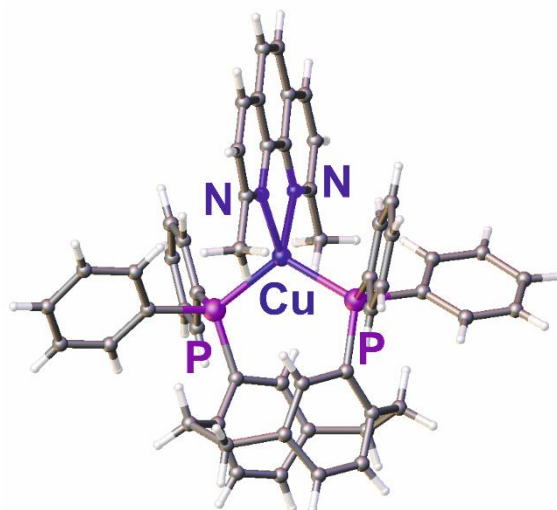


**Fig. 5.** Perspective drawing of  $\text{Cu}(\text{dmp})(\text{phanephos})^+$  **15**, resulting from x-ray crystallography studies. The counter anion  $\text{PF}_6^-$  and solvent molecules present in the crystal structure are omitted. The P-Cu-P bite angle is  $116^\circ$ . The methyl groups in positions 2 and 9 of phenanthroline provide significant sterical hindrance for flattening distortions occurring upon MLCT excitation. Adapted from [61] with permission from The Royal Society of Chemistry.

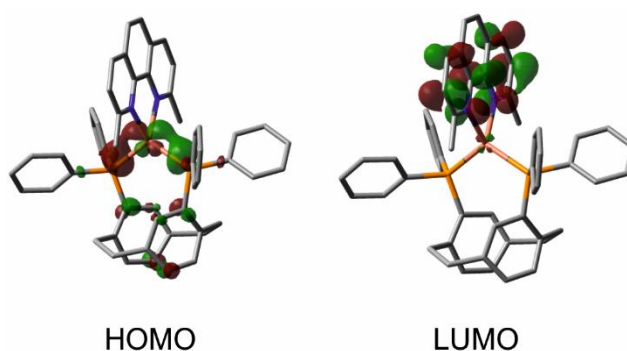


**Fig. 6.** Highest occupied molecular orbital (HOMO) and lowest unoccupied molecular orbital (LUMO) of  $\text{Cu}(\text{dmp})(\text{phanephos})^+$  **15**, displayed for the DFT-optimized ground state ( $S_0$ ) geometry. Calculations were performed on the B3LYP/def2-svp [150,151] level of theory. Hydrogen atoms are omitted for clarity. HOMO and LUMO exhibit distinctly different spatial distributions. The HOMO is mainly composed of the copper 3d and phosphorus  $\text{sp}^3$  atomic orbitals, while the LUMO represents a  $\pi^*$  orbital of the dmp ligand. Adapted from [61] with permission from The Royal Society of Chemistry.

The lowest excitations of all cationic complexes shown in Table 3 have distinct MLCT character with significant electron density shifts from copper (HOMO) towards the diimine ligands (LUMO). (Figure 6) Thus, flattening distortions upon excitation can be anticipated which, for several complexes, result in quenching of the emission. Indeed, the complexes  $\text{Cu}(\text{dmbpy})(\text{pop})^+$  and  $\text{Cu}(\text{phen})(\text{pop})^+$  are only very weakly emissive in solution with quantum yields of less than 1% and non-radiative rates  $k^{\text{nr}}$  of the order of  $10^6\text{-}10^7 \text{ s}^{-1}$ . The radiationless relaxations to the ground state can be suppressed to some degree by increasing the (external) rigidity induced by the matrix. However, even for the powder material, complexes comprising diimine ligands without any substitution that induces sterical hinderences with the second ligand, represent poor emitters. For instance, the  $\phi_{\text{PL}}$  value of the powder sample of  $\text{Cu}(\text{dmbpy})(\text{pop})^+$  at ambient temperature amounts to only about 9 % (Table 3), which is much below the requirements for emitter materials for efficient OLEDs.

$\text{Cu}(\text{dmbpy})(\text{pop})^+$  and  $\text{Cu}(\text{phen})(\text{pop})^+$  can be modified by introducing methyl groups into the 6 and 6' positions of bipyridine and the 2 and 9 positions of phenanthroline, giving  $\text{Cu}(\text{tmbpy})(\text{pop})^+$  **9** and  $\text{Cu}(\text{dmp})(\text{pop})^+$ , respectively (Table 3). Such modified diimine ligands should have stronger steric interactions with the pop ligand and thus, limit excited state distortions. Consequently, the efficiency of radiationless deactivation to the ground state should be reduced and the emission red shift induced by distortions of the molecular geometry should be less pronounced. Indeed, both effects, the increase of  $\phi_{\text{PL}}$  (accompanied by an increase of the emission decay time  $\tau$ ) as well as the blue shift of the emission, as compared to the unsubstituted complexes, are observed. In solution, the quantum yields of  $\text{Cu}(\text{tmbpy})(\text{pop})^+$  **9** and  $\text{Cu}(\text{dmp})(\text{pop})^+$

increase to 6 and 15 % (from distinctly less than 1 % in the case of Cu(dmbpy)(pop)<sup>+</sup> **9** and Cu(phen)(pop)<sup>+</sup>), respectively. The emission spectra are blue shifted to  $\lambda_{\max} = 575$  and 570 nm, compared to 655 and 700 nm for Cu(dmbpy)(pop)<sup>+</sup> and Cu(phen)(pop)<sup>+</sup>, respectively. [72,153] Apparently, such a ligand modification with methyl groups results in a reduction of the nonradiative rate  $k^{\text{nr}}$  by two orders of magnitude. For Cu(dbp)(pop)<sup>+</sup>, with the 2 and 9 positions of phenanthroline substituted with *n*-butyl groups being sterically more demanding than the methyl group, further decrease of the nonradiative rate is expected to occur. Indeed, the effects on  $k^{\text{nr}}$  are slightly more distinct than for Cu(dbp)(pop)<sup>+</sup> with  $k^{\text{nr}} = 5.3 \cdot 10^4 \text{ s}^{-1}$  than for Cu(dmp)(pop)<sup>+</sup> with  $k^{\text{nr}} = 6.1 \cdot 10^4 \text{ s}^{-1}$  (both in CH<sub>2</sub>Cl<sub>2</sub>). This strategy has also been successfully applied to homoleptic phenanthroline Cu(I) complexes. [149] Moreover, such substitutions prevent solvent molecules from coming closer to the metal center, and thus, are expected to reduce solvent-related excited-state relaxations.[160,161] It is remarked that introduction of sterically more demanding groups, such as branched aliphatic groups (e.g. *t*-butyl) instead of methyl or *n*-butyl in the 2 and 9 positions of phenanthroline prevents formation of a stable Cu-pop complex.

Cu(dmp)(phanephos)<sup>+</sup> **15** represents a further example in which excited state distortions are hindered owing to mutual sterical interactions of the substituted phenanthroline (dmp) and the bulky diphosphine ligand (phanephos). This compound exhibits a distinctly higher quantum yield in solution ( $\phi_{\text{PL}}(\text{CH}_2\text{Cl}_2) = 40 \%$ ) than Cu(dmp)(pop)<sup>+</sup> and Cu(dbp)(pop)<sup>+</sup>. Interestingly, this improvement does not result from a reduction of the radiationless relaxation processes. The value of  $k^{\text{nr}} = 6.0 \cdot 10^4 \text{ s}^{-1}$  for **15** is almost equal to  $k^{\text{nr}}$  of Cu(dmp)(pop)<sup>+</sup> and Cu(dbp)(pop)<sup>+</sup>. (Table 3) Thus, the increase of the quantum yield of **15** is related to an increase of the radiative rate  $k^{\text{r}}$  by a

factor of four as compared to  $\text{Cu(dmp)(pop)}^+$ . This effect may be a consequence of a higher TADF efficiency of  $\text{Cu(dmp)(phanephos)}^+$  **15** than for the other two compounds.

Similarly to the neutral complexes discussed above, the excited state distortions of complex **15** can be further reduced by increasing the matrix rigidity. Thus, the emission is blue shifted from  $\lambda_{\text{max}} = 558$  nm in dichloromethane to  $\lambda_{\text{max}} = 535$  and 530 nm in PMMA and for a powder sample, respectively. However, the value of  $\Delta\lambda_{\text{max}} = 28$  nm ( $\approx 950$   $\text{cm}^{-1}$ ) (fluid solution  $\rightarrow$  powder) is relatively small. (Table 3.) In parallel, the radiationless relaxation rates in powder are only four times smaller than in solution. Thus, both results indicate that in  $\text{Cu(dmp)(phanephos)}^+$  **15**, the excited state distortions are already confined at the molecular level. [61]

For completeness, it is remarked that aliphatic groups (methyl, *n*-butyl) have electron-donating character. Thus, introduction of such groups might increase the LUMO energy and consequently lead to a blue shift of the corresponding transitions. Indeed, slight blue shifts of the MLCT absorptions are observed both from  $\text{Cu(dmbpy)(pop)}^+$  towards  $\text{Cu(tmbpy)(pop)}^+$  [72] and from  $\text{Cu(phen)(pop)}^+$  towards  $\text{Cu(dmp)(pop)}^+/\text{Cu(dbp)(pop)}^+$  [153]. In emission, blue shifts of similar size would be expected. However, they are much larger, pointing to molecular rigidity effects as the main origin of these shifts, but not to electron donating effects of the alkyl groups. The dominance of the steric effects is also evident in electrochemistry of  $\text{Cu(phen)(pop)}^+$ ,  $\text{Cu(dmp)(pop)}^+$ , and  $\text{Cu(dbp)(pop)}^+$ . [153] Electron donating groups, such as methyl or *n*-butyl, are expected to stabilize the oxidized form of the complex, but cyclic voltammetry data reveal that the oxidation potential for the Cu(II)/Cu(I) redox couple shifts from  $\text{Cu(phen)(pop)}^+$  to  $\text{Cu(dmp)(pop)}^+$  by 0.15 V and to  $\text{Cu(dbp)(pop)}^+$  by 0.16 V towards more positive potentials. This behavior occurs because in complexes with dmp and dbp, the ligand

framework resists rearrangements to a more flattened structure which would be more appropriate for the oxidized Cu(II) species. [153]

Summing up, reducing the extent of the excited-state geometry distortions occurring upon MLCT excitation is essential for enhancement of the emission quantum yields. This can be achieved by optimizing the matrix material to limit such distortions of the doped emitter molecules. A promising strategy is also based on chemical modifications to achieve higher molecular rigidity by using steric requirements of the ligands. In the latter approach, excited state distortions are already hindered at the molecular level. (Figure 7) As a consequence, these complexes exhibit relatively high quantum yields also in fluid solution.

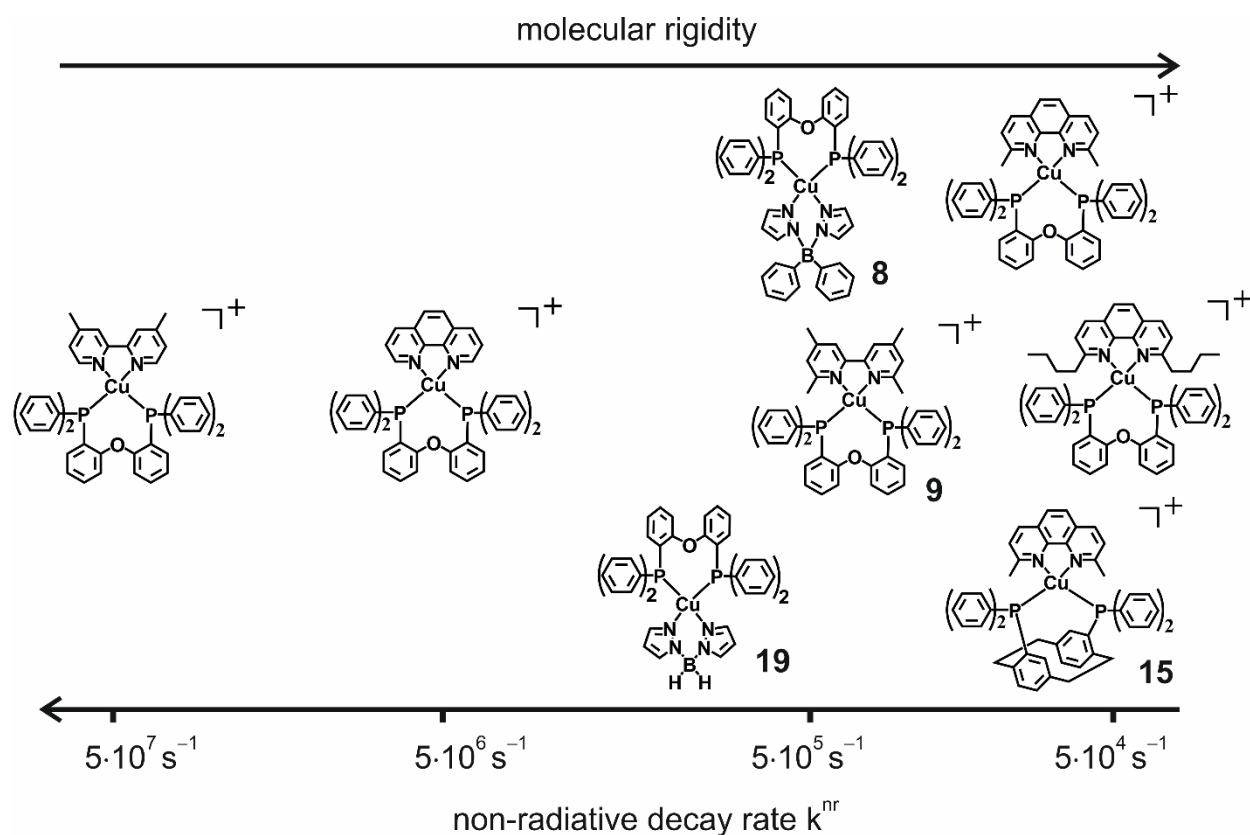


**Fig. 7.** Copper complexes displaying different molecular rigidity which correlates with the non-radiative emission decay rate  $k^{nr}$  in solution. This correlation may be used as a very rough measure of excited state geometry changes with respect to the electronic

ground state geometry being a main source of emission quenching. (Data from Tables 2 and 3)

It is remarked that the emission of the Cu(I) complexes discussed in this chapter represents a thermally activated delayed fluorescence (TADF)<sup>4</sup> at ambient temperature and that the radiative and non-radiative rates,  $k^r$  and  $k^{nr}$ , calculated from the experimental  $\phi_{PL}$  and  $\tau$  values, may refer to the relaxations from the  $T_1$  and  $S_1$  states to the ground state. In this section it was not discussed which radiationless or radiative path prevails, but it is obvious that both non-radiative processes, from  $S_1$  to  $S_0$  as well as from  $T_1$  to  $S_0$ , may be suppressed to a large extent in properly engineered complexes.

The occurrence of excited state geometry distortions has another important consequence. Typically, powder samples are not well suited to investigate molecular luminescence as additional inter-molecular effects, for example, energy transfer to impurities, may strongly influence the emission properties, especially the decay behavior. However, the geometry distortions are sufficient, even in the solid phase, to lower the excited state energy to such an extent that the resonance condition for energy transfer to adjacent non-excited molecules is no longer fulfilled. [4,5,65,73] Therefore, the excitation may be regarded as trapped at the initially excited emitter molecule. Consequently, even powder samples can be used to study emission properties of these MLCT compounds. Such a self-trapping effect [162,163] is the basis for the studies of temperature dependent emission properties presented in the next sections. (Figure 8)

---

<sup>4</sup> For a detailed discussion see section 4.



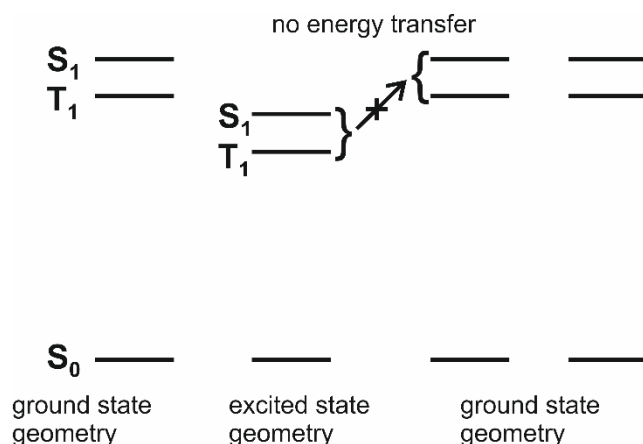


**Fig. 8.** Schematic illustration of the exciton self-trapping effect in solid samples (100 % emitter material) of Cu(I) complexes. Upon MLCT excitation, significant lowering of the  $S_1$  and  $T_1$  energies occurs. Thus, the resonance condition for energy transfer is not met.

#### 4. Case study: Characterization of selected TADF compounds and controlling TADF

In this section, we present at first a study of two Cu(I) complexes, Cu(dppb)(pz<sub>2</sub>Bph<sub>2</sub>) **2** and Cu(pop)(pz<sub>2</sub>Bph<sub>2</sub>) **8**, that appear structurally similar but exhibit distinctly different though in both cases highly efficient TADF. [65,67] In the second part, a material, (IPr)Cu(py<sub>2</sub>-BMe<sub>2</sub>) **10** [45,66], clearly showing TADF behavior is presented, but “slight” structure variations, giving (Bzl-3,5Me)Cu(py<sub>2</sub>-BMe<sub>2</sub>) **10a** [45,66] (chemical structure displayed in Figure 17 below), result in “tuning-off” the TADF. We will show that this behavior can be simulated by a quantum mechanical approach. [45]

##### 4.1 Efficient TADF of selected Cu(I) complexes

###### Cu(dppb)(pz<sub>2</sub>Bph<sub>2</sub>)

The emission behavior of  $\text{Cu}(\text{dppb})(\text{pz}_2\text{Bph}_2)$  **2** has been discussed in detail in refs.[67,164]. However, before presenting experimental data, it is suitable to introduce to the compound's properties by use of DFT calculations. An inspection of the frontier orbitals shows that the HOMO is largely derived from a 3d atomic orbital of the Cu(I) center with contributions from the coordinating phosphorus atoms, whereas the LUMO is mainly distributed over the *o*-phenylene ring of the dppb (= 1,2-bis(diphenylphosphino)benzene) ligand. (Figure 9) As a consequence, the related transitions are assigned the MLCT character involving dppb as chromophoric ligand. It has been shown by TD-DFT calculations that the resulting singlet state  $S_1$  and triplet state  $T_1$  are to more than 90% of HOMO-LUMO character. Therefore, these states are assigned as  $^1\text{MLCT}$  ( $S_1$ ) and  $^3\text{MLCT}$  ( $T_1$ ) states, respectively. [67]

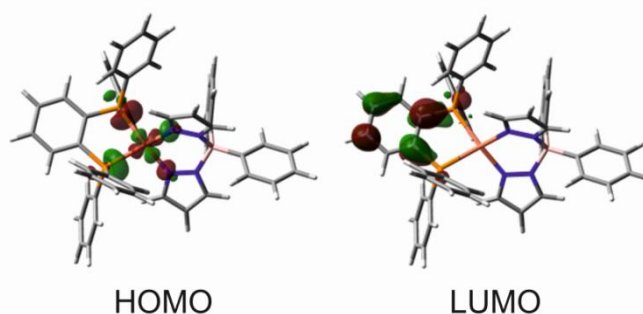


**Fig. 9** HOMO and LUMO of  $\text{Cu}(\text{dppb})(\text{pz}_2\text{Bph}_2)$  **2** resulting from DFT calculations for the triplet state geometry at the B3LYP/def2-svp [150,151] theory level. Adapted with permission from [67]. Copyright (2015) American Chemical Society.

The spatial separation of HOMO and LUMO (Figure 9) indicates a small exchange integral [142] and therefore, a small energy separation between  $^1\text{MLCT}$  and  $^3\text{MLCT}$ . Indeed, TD-DFT calculations (gas phase) give a value of  $\Delta E(S_1-T_1) \approx 560 \text{ cm}^{-1}$  (69 meV) [67], but the experimentally determined energy separation is even significantly smaller ( $370 \text{ cm}^{-1}$  (46 meV), see below).

The emission properties of compound **2** were studied in ref. [67] over a wide temperature range from  $T = 1.5$  K to 300 K. Figure 10 reproduces emission spectra and decay curves of a powder sample of **2** at different temperatures. The complex shows intense green-yellow luminescence with high emission quantum yield of  $\phi_{\text{PL}} = 70\%$  at ambient temperature and of about 100% at  $T = 80$  K and probably also at least down to  $T \approx 30$  K. The spectra are broad and unstructured even at 1.5 K. [67] This is in line with the MLCT character of the corresponding transitions. Moreover, one does not observe any significant spectral change apart from a blue shift of the emission maximum with temperature increase from 548 nm (1.5 K, 30 K) to 535 nm (80 K, 300 K) of 13 nm ( $\approx 440 \text{ cm}^{-1}$ ). (Figure 10) This blue shift is a consequence of a thermal activation of the energetically higher lying  $S_1$  state above  $T \approx 50$  K. On the other hand, the emission decay time and the radiative decay rate change drastically. (Figures 10 and 11) For  $\approx 30 \text{ K} \leq T \leq 50 \text{ K}$ , the decay time amounts to  $\tau(T_1) = 1200 \text{ }\mu\text{s}$  staying almost constant (plateau) and then decreases with increasing temperature to  $\tau(300 \text{ K}) = 3.3 \text{ }\mu\text{s}$ . Thus, according to eq. (3), an increase of the radiative rate from  $k^r(30 \text{ K}) = 8.3 \cdot 10^2 \text{ s}^{-1}$  to  $k^r(300 \text{ K}) = 2.1 \cdot 10^5 \text{ s}^{-1}$  is observed representing an increase by a factor of more than 250.

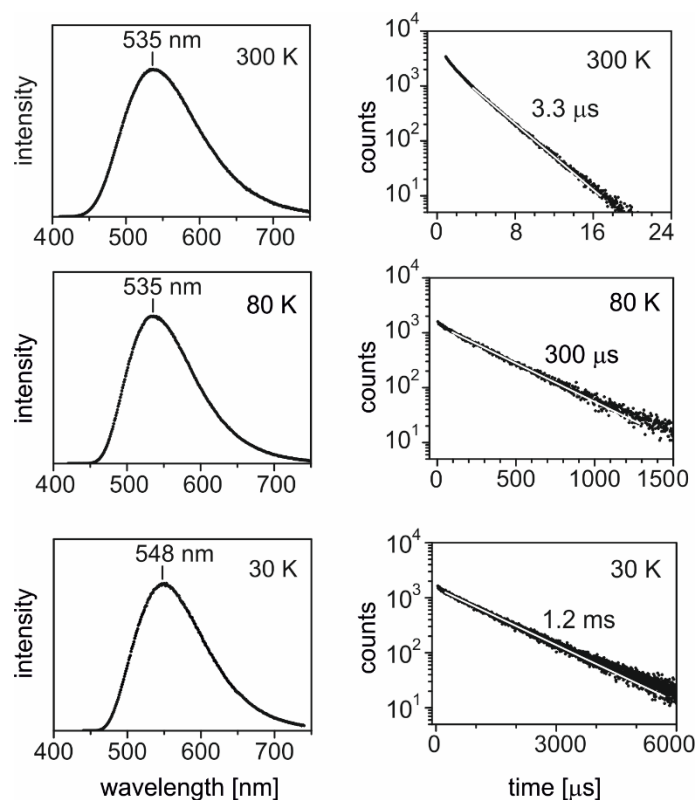


**Fig. 10** Emission spectra and decay behavior of Cu(dppb)(pzzBph<sub>2</sub>) **2** powder at different temperatures. Adapted with permission from [67]. Copyright (2015) American Chemical Society.

In Figure 11, the emission decay time is plotted versus temperature (together with a plot for compound **8** that is discussed below). At low temperature, i.e. in the range of the plateau up to  $T \approx 50$  K only a long-lived phosphorescence ( $T_1 \rightarrow S_0$ ) with  $\tau(T_1) = 1200 \mu\text{s}$  is observed. With increasing temperature, fast up-ISC (RISC) to the  $S_1$  state takes place and opens the additional radiative TADF process via the decay path from the  $S_1$  state. This leads to a drastic decrease of the emission decay time and to the observed blue shift of the emission spectrum, since the emitting  $S_1$  state lies higher in energy than the  $T_1$  state.

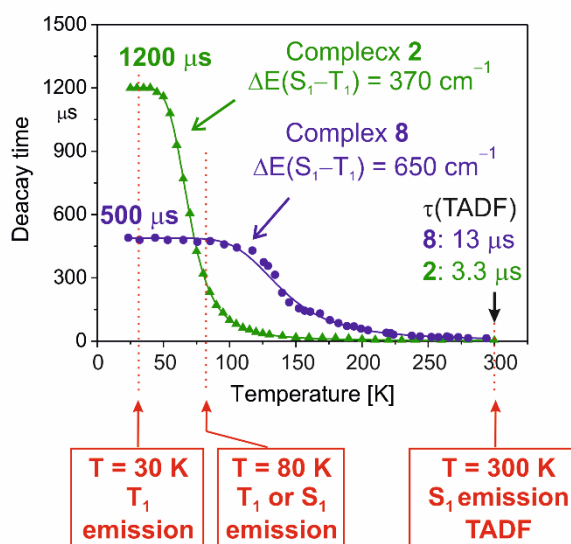


**Fig. 11** Luminescence decay times of Cu(dppb)(pz<sub>2</sub>Bph<sub>2</sub>) **2** (green triangles) and Cu(pop)(pz<sub>2</sub>Bph<sub>2</sub>) **8** (blue points) versus temperature for powder samples. The dominant emission mechanisms near 30, 80, and 300 K are indicated. Adapted with permission from [67]. Copyright (2015) American Chemical Society.

According to fast up- and down-ISC processes, i.e. faster than the emission decay times, a thermal equilibration between the energy states is present. Thus, we can apply eq. (1) to fit the experimental data. As seen in Figure 11 the fit is excellent. Fixing the emission decay time of  $\tau(T_1) = 1.2$  ms (experimental value in the range of the plateau), one obtains the fit parameters for the activation energy<sup>5</sup> of  $\Delta E(S_1-T_1) = 370$  cm<sup>-1</sup> (46 meV) and for the S<sub>1</sub> decay time of  $\tau(S_1) = 180$  ns. [67] It is noted that the prompt fluorescence (S<sub>1</sub>→S<sub>0</sub>) was not observed even at low temperature. This is a consequence of the very fast down-ISC process of only several ps. [81,116,120,123,124,133,165,166] From the decay time  $\tau(S_1)$  resulting from the fit, one can determine the radiative rate for this S<sub>1</sub>↔S<sub>0</sub> transition according to eq. (3). With  $\phi_{PL} = 70\%$  and  $\tau(S_1) = 180$  ns a value of  $k^r(S_1 \leftrightarrow S_0) = 3.9 \cdot 10^6$  s<sup>-1</sup> is obtained. A corresponding consideration has also been carried out in Ref [61] for compound **15**. For

<sup>5</sup> The activation energy determined to 370 cm<sup>-1</sup> is slightly smaller than the value of 440 cm<sup>-1</sup> obtained from the energy difference between the low-temperature and the high-temperature emission spectra. Such a deviation is not unusual, since the potential energy surfaces of the triplet and singlet state may be slightly shifted with respect to each other.

this complex, the rate was independently estimated from the absorption spectrum using the Strickler-Berg relation [167]. The rates resulting from both emission and absorption data agree fairly well with each other.

For compound **2**, one obtains the energy level diagram as displayed in Figure 12.

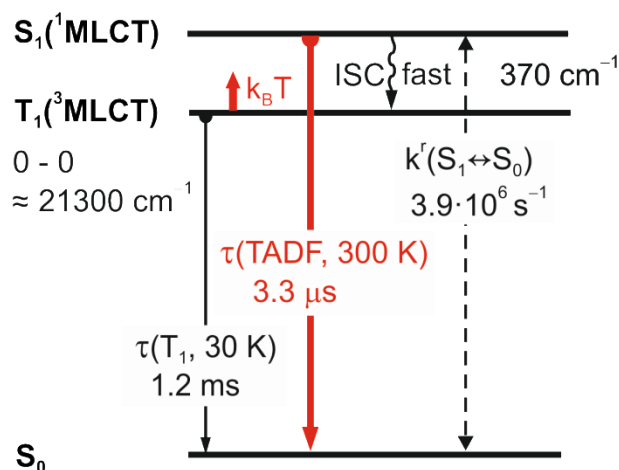


**Fig. 12** Energy level diagram for the lowest states and emission decay times as well as the rate for the  $S_1 \rightarrow S_0$  transition for  $\text{Cu}(\text{dppb})(\text{pz}_2\text{Bph}_2)$  **2** (powder). The zero-field splitting of the triplet state  $T_1$  being less than  $\approx 1 \text{ cm}^{-1}$  ( $\approx 0.1 \text{ meV}$ ) [67], is not illustrated in this diagram.

It is emphasized that  $\text{Cu}(\text{dppb})(\text{pz}_2\text{Bph}_2)$  **2** has a very long decay time of the triplet state of  $\tau(T_1) = 1.2 \text{ ms}$ . Nevertheless, the ambient temperature decay time amounts only to  $\tau(\text{TADF}) = 3.3 \text{ }\mu\text{s}$ . With the measured quantum yield of  $\phi_{\text{PL}} = 70\%$ , a radiative decay time of  $\tau^r(\text{TADF}) = 4.7 \text{ }\mu\text{s}$  is obtained. This value belongs to the shortest ones reported for Cu(I) complexes so far. Obviously, a small energy separation of  $\Delta E(S_1-T_1)$  is of crucial importance to induce short-lived TADF.

Interestingly, compound **2** and its derivatives have already been applied as emitters in OLEDs (being processed by vacuum deposition). For these devices, high external quantum efficiencies of almost 18 % were reported. [34]

### **Cu(pop)(pz<sub>2</sub>Bph<sub>2</sub>) **8****

DFT calculations carried out for a gas phase show, similarly to compound **2**, that the HOMO is largely located at the Cu(I) center, while the LUMO lies on the chromophoric pop ligand. (Figure 4) From TD-DFT calculations for the optimized triplet state geometry it follows that the lowest excited singlet and triplet state, <sup>1</sup>MLCT(S<sub>1</sub>) and <sup>3</sup>MLCT(T<sub>1</sub>), are largely of HOMO→LUMO character. The calculated energy separation between these states amounts to 920 cm<sup>-1</sup> (114 meV). Again, the experimentally determined activation energy is with  $\Delta E(S_1-T_1) = 650 \text{ cm}^{-1}$  (80 meV) distinctly smaller. However, both of these values are still small enough to expect occurrence of an efficient TADF.

The luminescence properties of Cu(pop)(pz<sub>2</sub>Bph<sub>2</sub>) **8** were investigated in the temperature range  $1.6 \leq T \leq 300 \text{ K}$ . [2,4,65] In order to minimize effects of flattening distortions occurring upon the MLCT excitation (section 3), powder samples were studied. In the whole temperature range, the emission spectra of compound **8** are broad and unstructured, as expected for MLCT transitions. At 1.6 K, the complex emits with  $\lambda_{\text{max}} = 474 \text{ nm}$  (Figure 13). With temperature increase to  $T \approx 100 \text{ K}$ , the emission maximum does not markedly change. However, with further temperature increase, the spectra become broader and a blue shift is observed. Above  $T = 200 \text{ K}$ , the emission maximum approaches the ambient temperature value of  $\lambda_{\text{max}} = 464 \text{ nm}$ . The spectral blue shift occurring with temperature increase amounts to 10 nm.

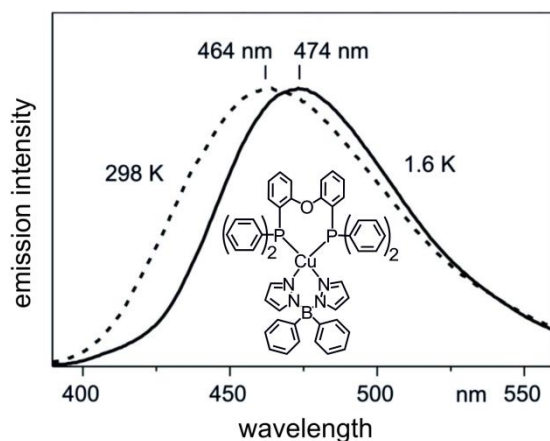


**Fig. 13** Emission spectra of Cu(pop)(pz<sub>2</sub>Bph<sub>2</sub>) **8** (powder) at 1.6 and 298 K.  $\lambda_{\text{exc}} = 355$  nm,  $\phi_{\text{PL}}(300 \text{ K}) = 90\%$ ,  $\phi_{\text{PL}}(77 \text{ K}) \approx 100\%$ . [2,65] Adapted with permission from [65]. Copyright (2011) American Chemical Society.

It is remarked that even the  $T = 1.6 \text{ K}$  spectrum shows a half-width of almost  $3500 \text{ cm}^{-1}$ . Accordingly, no spectral details can be resolved. However, applying the technique of measuring the temperature dependence of the emission decay time, a resolution of energy splittings even of the order of  $1 \text{ cm}^{-1}$  can be obtained under specific conditions. This is due to the small energy steps that can be adjusted by temperature variation. For example, the thermal energy change of  $k_B\Delta T$  for  $\Delta T = 1 \text{ K}$  corresponds to only  $0.7 \text{ cm}^{-1}$ . In several cases, thermal energies of this order of magnitude can induce distinct changes of the emission decay properties due to thermally induced population changes of electronic states with different decay times.

The emission decay of compound **8** shows a very characteristic behavior at low temperature and a pronounced decrease of the decay time with temperature increase. At  $T = 1.6 \text{ K}$ , the decay profile is clearly non-exponential (Figure 14). It can be described by a tri-exponential decay function with the individual components of  $2 \text{ ms}$  ( $\tau(\text{I})$ ),  $600 \mu\text{s}$  ( $\tau(\text{II})$ ), and  $170 \mu\text{s}$  ( $\tau(\text{III})$ ). A similar behavior has already been discussed for other Cu(I) complexes [65,73] as well as, for example, for Pt(II) [18,59,168-173],



Pd(II) [59,174,175], Rh(III) [176,177], Ir(III) [178] and Re(I) [179] complexes. Thus, at  $T = 1.6$  K, the three components are assigned to originate from the three different triplet substates I, II, and III. At  $T = 1.6$  K, these states are not thermally equilibrated due to very slow spin-lattice relaxation (SLR) processes at an energy separation between the substates of  $\Delta E(\text{ZFS}) \approx 1 \text{ cm}^{-1}$  or less. [18,59,179-182] In this situation, the individual emission decay times of the three substates are much shorter than the SLR times. With temperature increase to  $T \approx 20$  K or  $\approx 40$  K, however, these SLR processes become significantly faster and a fast thermalization of the three substates takes place. As a consequence, a mono-exponential decay results and an average decay time  $\tau_{\text{av}}$  is observed. This average value can be expressed by [2-5,59,65,73,180,182]

$$\tau_{\text{av}} = 3\left(\tau(\text{I})^{-1} + \tau(\text{II})^{-1} + \tau(\text{III})^{-1}\right)^{-1} \quad (4)$$

Inserting the three decay components given above into eq. (4), an average decay time  $\tau_{\text{av}}(T_1)$  of slightly less than  $400 \mu\text{s}$  is obtained. Within limits of experimental and fitting error, this value corresponds sufficiently well to the decay time of  $500 \mu\text{s}$  measured at  $T = 40$  K. (Figures 11 and 14)

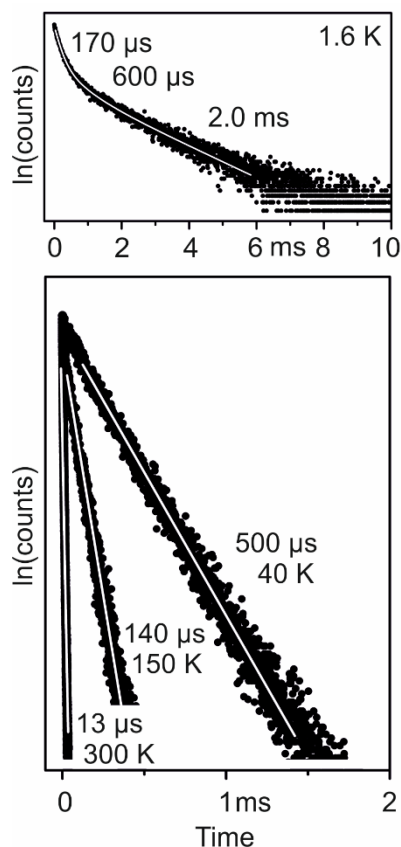


**Fig. 14** Emission decay of Cu(pop)(pz<sub>2</sub>Bph<sub>2</sub>) **8** (powder) at different temperatures after pulsed excitation at  $\lambda_{\text{exc}} = 355$  nm (pulse width 7 ns) and detected at 470 nm. Note the different time scales. Adapted with permission from [65]. Copyright (2011) American Chemical Society.

In Figure 11, we reproduce the dependence of the emission decay time of **8** versus temperature for the range of  $T = 30$  to 300 K. The decay is almost constant between about 30 and 100 K (plateau) and amounts to about 500  $\mu\text{s}$ . Accordingly, this value is assigned to represent the decay time  $\tau(T_1)$  of the emitting <sup>3</sup>MLCT state. Obviously, this decay time is also very long, especially, if compared to Ir(III) or Pt(II) complexes with the values of a few  $\mu\text{s}$  (showing significant MLCT character of the emitting triplet states). [1,2,4,57,60,183,184] This is related not only to the smaller SOC constant of copper, being about five times smaller than that of iridium or platinum [108], but also to the less efficient SO mixing routes with higher lying <sup>1</sup>MLCT states (see also section 7).

With further temperature increase (above  $T = 100$  K) and remaining high emission quantum yield (Table 2), the decay time becomes distinctly shorter and drops to  $\tau(\text{TADF}) = 13 \mu\text{s}$  (Figures 11 and 14). This observation, together with the blue shift of the emission spectra (Figure 13), indicates – as already studied for compound **2** – that a higher lying electronic state with a distinctly greater deactivation rate becomes thermally populated. As discussed above and in analogy to a number of other investigations with Cu(I) complexes [2,4,5,44,45,61,67,68,72,73,109,110,185,186], this higher lying state is assigned to the lowest excited singlet state  $S_1$  of  $^1\text{MLCT}$  character. Above 200 K, the singlet state emission strongly dominates. It represents a thermally activated delayed fluorescence [2,65,67,68]. As the emission quantum yields amount to  $\phi_{\text{PL}}(77 \text{ K}) \approx 100\%$  with  $\tau(77 \text{ K}) = 500 \mu\text{s}$  and to  $\phi_{\text{PL}}(300 \text{ K}) = 90\%$  with  $\tau(300 \text{ K}) = 13 \mu\text{s}$  [63], the radiative rate (eq. (3)) is determined to increase from  $k^r(77 \text{ K}) = 2 \cdot 10^3 \text{ s}^{-1}$  to  $k^r(300 \text{ K}) = 7 \cdot 10^4 \text{ s}^{-1}$ , i.e. by a factor of 35.

The fitting procedure applying eq. (1) to the measured decay time data of Cu(pop)(pz<sub>2</sub>Bph<sub>2</sub>) **8** (Figure 11) gives values of  $\Delta E(S_1-T_1) = 650 \text{ cm}^{-1}$  (80 meV) and of  $\tau(S_1) = 170 \text{ ns}$  for the  $S_1$  decay time. These data together with the data given above are summarized in an energy level diagram. (Figure 15)

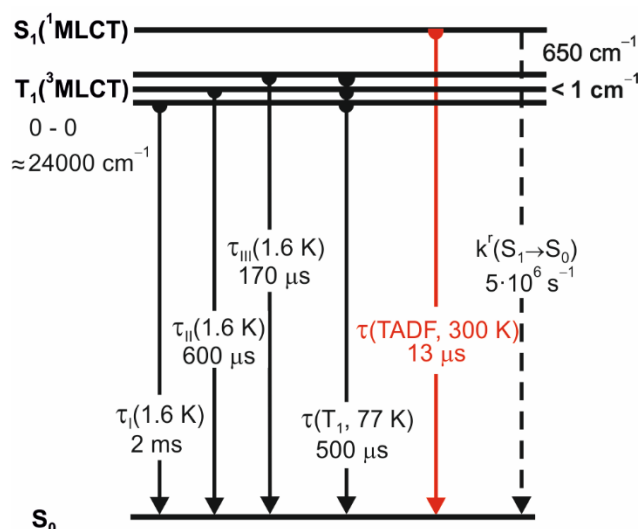


**Fig. 15** Energy level diagram of Cu(pop)(pz<sub>2</sub>Bph<sub>2</sub>) **8** powder for the lowest states and emission decay times as well as the rate of the S<sub>1</sub>→S<sub>0</sub> transition. The radiative rate of the prompt fluorescence from S<sub>1</sub>, being not directly observable in our investigations, is calculated by use of eq. (3) inserting τ(S<sub>1</sub>) = 170 ns and φ<sub>PL</sub>(300 K) = 90%.

A comparison of emission properties of the two compounds **2** and **8** is instructive in several respects: (i) Both compounds show efficient TADF at ambient temperature. However, because of the large difference in ΔE(S<sub>1</sub>-T<sub>1</sub>) of 370 cm<sup>-1</sup> (≈ 46 meV) (**2**) compared to 650 cm<sup>-1</sup> (≈ 80 meV) (**8**), the temperature behavior of the decay time is rather different. (Fig. 11) With temperature decrease, TADF is frozen out below T ≈ 100 K for compound **8**, while for compound **2**, this is reached only below T ≈ 30 K. Accordingly, at T = 80 K, the emission of compound **2** with a decay time of τ(80 K) ≈ 300 μs cannot be assigned as a phosphorescence. It represents dominantly a TADF with an intensity ratio of TADF/phosphorescence of about 75%/25% at T = 80 K. [67] Therefore, assignments with respect to the emission characteristics as phosphorescence or fluorescence (TADF) might be problematic for Cu(I) compounds, if investigated only at 300 K and 80 K, as often reported. Similar arguments hold also for the assignments of the spectral shifts between phosphorescence and TADF. (Figure 10) (ii) The very small value of ΔE(S<sub>1</sub>-T<sub>1</sub>) = 370 cm<sup>-1</sup> for compound **2** is responsible for

the large radiative TADF rate at  $T = 300 \text{ K}$  of  $k^r(300 \text{ K}) = 2.1 \cdot 10^5 \text{ s}^{-1}$  being only by a factor of about three smaller than the radiative rate of the well-known  $\text{Ir}(\text{ppy})_3$  complex. [4,60] Moreover, due to the largely forbidden nature of the  $T_1 \rightarrow S_0$  transition with a radiative rate of only  $k^r(30 \text{ K}) = 8.3 \cdot 10^2 \text{ s}^{-1}$ , the TADF effect induces a rate increase by more than a factor of 250 with temperature increase from  $T = 30 \text{ K}$  to  $300 \text{ K}$ . The effect is much less pronounced for compound **8** with a rate increase by a factor of 35 from  $k^r(80 \text{ K}) = 20 \cdot 10^2 \text{ s}^{-1}$  to  $k^r(300 \text{ K}) = 6.9 \cdot 10^4 \text{ s}^{-1}$ . Compound **2** attains a much larger TADF transition rate at ambient temperature than compound **8**. (iii) The rate of the radiative decay for the triplet state to the singlet ground state is dictated by the efficiency of SOC. (This is also valid for the size of ZFS, [2,4,57,183,184], section 7) Both compounds **2** and **8** exhibit relatively long triplet state decay times of  $1200 \mu\text{s}$  (**2**) and  $500 \mu\text{s}$  (**8**), respectively. Hence, only weak SOC is effective for both compounds. Nevertheless, this difference can be explained qualitatively in the scope of a perturbation theory model. SO induced mixing of  $^1\text{MLCT}$  and  $^3\text{MLCT}$  resulting from the same HOMO-LUMO excitation is not relevant (extended El-Sayed rule [187]) [2,4,5,57,187-192]. However, if a different d-orbital is involved, such as in a different  $^1\text{MLCT}$  state, SOC can become effective and induce singlet character to the triplet state. Accordingly, the  $T_1 \leftrightarrow S_0$  transition can become distinctly allowed. TD-DFT calculations show that the next higher lying singlet MLCT state – involving a different d-orbital than the lowest  $^3\text{MLCT}$  ( $T_1$ ) state – is  $S_6$  for compound **2** and  $S_2$  for compound **8** with energy separations of  $1.54 \text{ eV}$  ( $\approx 1240 \text{ cm}^{-1}$ ) for **2** and  $0.79 \text{ eV}$  ( $\approx 6400 \text{ cm}^{-1}$ ) for **8**. [65,67] Both energy separations to mixing states are very large, hence the  $T_1 \rightarrow S_0$  rates are small for both compounds. But the values show that compound **2** should exhibit an even smaller triplet rate than compound **8**. Indeed, this is observed. For a more detailed discussion of SO mixing routes see section 7.

## 4.2 Controlling of singlet-triplet splitting

In the previous section, we presented two selected Cu(I) compounds, which exhibit different  $\Delta E(S_1-T_1)$  values according to spatially different HOMO-LUMO distributions. In this section, we want to study two largely similar Cu(I) complexes, Cu(IPr)(py<sub>2</sub>-BMe<sub>2</sub>) **10** and Cu(Bzl-3,5Me)(py<sub>2</sub>-BMe<sub>2</sub>) **10a**, with IPr = 1,3-bis(2,6-diisopropylphenyl)imidazol-2-ylidene, Bzl-3,5Me = 1,3-bis(3,5-dimethylphenyl)-1H-benzo-[d]imidazol-2-ylidene, and py<sub>2</sub>-BMe<sub>2</sub> = di(2-pyridyl)dimethylborate. (Structure formulas are displayed in Figure 17.) In these complexes, the angular orientations of HOMO and LUMO are strongly different. This has a drastic influence on  $\Delta E(S_1-T_1)$  with the consequence that **10** is a TADF compound, while **10a** does not show any TADF at ambient temperature due to a very large  $\Delta E(S_1-T_1)$  energy separation. In the second part of this section, we will simulate the drastic  $\Delta E(S_1-T_1)$  changes by a theoretical model based on TD-DFT calculations.

### 4.2.1 Compounds with and without TADF at ambient temperature

DFT calculations performed for the ground state optimized molecular geometries of Cu(IPr)(py<sub>2</sub>-BMe<sub>2</sub>) **10** and Cu(Bzl-3,5Me)(py<sub>2</sub>-BMe<sub>2</sub>) **10a** reveal that the HOMOs of both complexes consist predominantly of copper d orbitals mixed with  $\pi$  contributions from the di(2-pyridyl)dimethylborate ligand, whereas the LUMOs are localized mainly on the N-heterocyclic carbene ligands IPr and Bzl-3,5Me, respectively. [45,66] (Figure 16) Therefore, for both complexes, significant MLCT character mixed with ligand-to-ligand charge transfer (LLCT) character can be anticipated for the lowest electronic excitations. Moreover, TD-DFT calculations predict for both complexes that the lowest excited states are dominated by HOMO-LUMO transitions, and thus, substantiate the (M+L)LCT assignments. [66] Expansion of the aromatic system from IPr in **10** towards Bzl-3,5Me in **10a**, results in a significantly lower lying LUMO energy of **10a**, while the

HOMO distribution and energy are essentially not affected. Thus, the calculated HOMO-LUMO gap of **10a** is significantly smaller than of compound **10**. This effect is manifested in the emission spectra. A significant red shift of the emission of the Bzl-3,5Me complex **10a** compared to the IPr complex **10** is observed. (Figure 17) This shows the relevance of the DFT calculations performed for the studied systems.

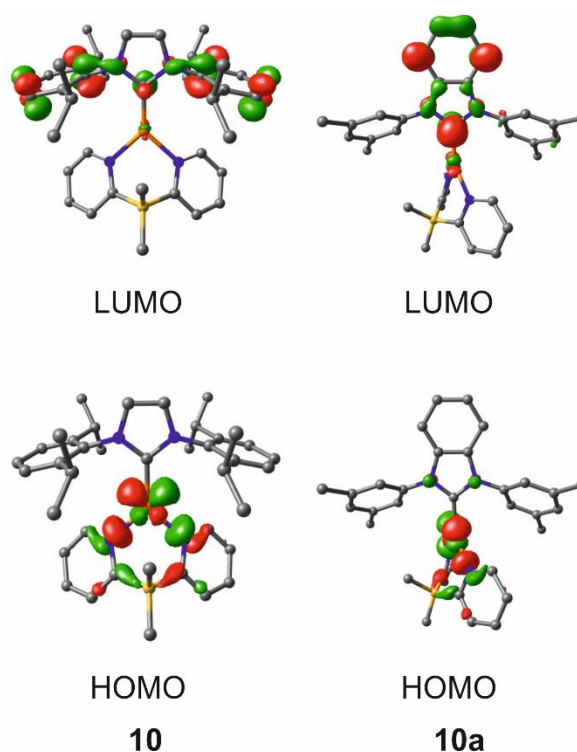


**Figure 16** HOMO and LUMO frontier orbitals of Cu(IPr)(py<sub>2</sub>-BMe<sub>2</sub>) **10** and Cu(Bzl-3,5Me)(py<sub>2</sub>-BMe<sub>2</sub>) **10a** resulting from DFT calculations based on ground state optimized molecules. Computations were performed at the B3LYP/def2-svp [150,151] level of theory. Compare ref. [66]

Powders of complexes **10** and **10a** display intense blue and yellow luminescence at ambient temperature with short emission decay times of 11  $\mu$ s and 18  $\mu$ s and remarkably high quantum yields of 76 % and 73 %, respectively. [45] The spectra shown in Figure 17 are broad and featureless with maxima at 475 nm (**10**) and 575 nm

(10a). The shapes of the spectra suggest that the emissions originate from charge transfer transitions, as predicted by TD-DFT calculations.

When cooling from ambient temperature to 77 K, a red-shift of the emission from 475 to 490 nm ( $\approx 650 \text{ cm}^{-1}$ ) is observed for compound **10**. In addition, the emission decay time increases by a factor of about 3 from 11  $\mu\text{s}$  to 34  $\mu\text{s}$ , whereas the radiative rate  $k^r$  decreases by almost the same factor from  $6.9 \cdot 10^4$  to  $2.7 \cdot 10^4 \text{ s}^{-1}$ . (Table 4) The smaller radiative rate determined at  $T = 77 \text{ K}$  suggests that the emitting state is the triplet state  $T_1$ . However, it is remarked that a triplet decay time of 34  $\mu\text{s}$  is extraordinarily short compared to other Cu(I) compounds. (Compare section 4.1, Table 7 (below) and Refs. [4,5,39,57,65,72,73].) This indicates that spin-orbit coupling is particularly effective in compound **10**. (Compare also sections 6 and 7.) The observed changes of the emission decay time (or the radiative rate) and the spectral shift of the emission upon temperature change indicate that the ambient-temperature emission of **10** represents largely TADF.

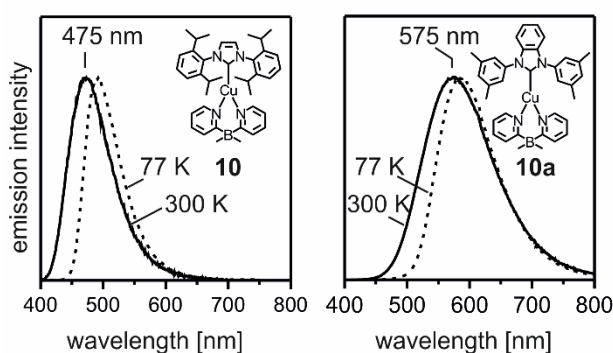


**Fig. 17.** Normalized emission spectra of copper complexes Cu(IPr)(py<sub>2</sub>-BMe<sub>2</sub>) **10** and Cu(Bzl-3,5Me)(py<sub>2</sub>-BMe<sub>2</sub>) **10a** as powders at ambient temperature (solid lines) and at 77 K (dashed lines). Adapted with permission from [45]. Copyright (2014) American Chemical Society.



**Table 4.** Emission properties of Cu(IPr)(py<sub>2</sub>-BMe<sub>2</sub>) **10** and Cu(Bzl-3,5Me)(py<sub>2</sub>-BMe<sub>2</sub>) **10a** as powders.  $\lambda_{\max}$ ,  $\tau$ , and  $\phi_{\text{PL}}$  are the emission maximum, decay time, and quantum yield, respectively. Experimental data from Ref. [45]

	Cu(IPr)(py <sub>2</sub> -BMe <sub>2</sub> ) <b>10</b>		Cu(Bzl-3,5Me)(py <sub>2</sub> -BMe <sub>2</sub> ) <b>10a</b>	
	300 K	77 K	300 K	77 K
$\lambda_{\max}$ [nm]	475	490	575	585
$\phi_{\text{PL}}$ [%]	76	91	73	80
$\tau$ [ $\mu\text{s}$ ]	11	34	18	21
$k^{\text{r}}$ [ $\text{s}^{-1}$ ] <sup>a</sup>	$6.9 \cdot 10^4$	$2.7 \cdot 10^4$	$4.1 \cdot 10^4$	$3.8 \cdot 10^4$
$k^{\text{nr}}$ [ $\text{s}^{-1}$ ] <sup>a</sup>	$2.2 \cdot 10^4$	$0.3 \cdot 10^4$	$1.5 \cdot 10^4$	$1.0 \cdot 10^4$

<sup>a</sup> The radiative and non-radiative rates,  $k^{\text{r}}$  and  $k^{\text{nr}}$ , were calculated according to eqs. (2) and (3).

In contrast, when cooling compound **10a** from ambient temperature to 77 K, the emission decay time changes only slightly from 18  $\mu\text{s}$  to 21  $\mu\text{s}$ , while the  $k^{\text{r}}$  change from  $4.1 \cdot 10^4 \text{ s}^{-1}$  to  $3.8 \cdot 10^4 \text{ s}^{-1}$  is negligible. (Table 4) This indicates that for complex **10a** the TADF mechanism is not effective and that also the emission at ambient temperature is a phosphorescence stemming from the T<sub>1</sub> state. The slight blue shift of the high energy flank observed on heating may be explained by a small thermal broadening of the spectrum due an involvement of energetically higher lying vibronic emission components in the powder sample (compare Ref [193]).<sup>6</sup> This behavior is in contrast to that of complex **10** for which the entire spectrum is shifted. (Figure 17)

Figure 18 shows the dependence of the emission decay time of Cu(IPr)(py<sub>2</sub>-BMe<sub>2</sub>) **10** on temperature. The decays are mono-exponential in the entire temperature range with exception of very low temperatures between 1.3 K and about 25 K, where spin-lattice relaxations (SLR) effects [180,181] are observed. [45] The data displayed show only

<sup>6</sup> Further support for this rationalization comes from studies in poly(methyl methacrylate) (PMMA). In this polymer doped with complex **10a** investigated at ambient temperature and 77 K, no such spectral shifts are observed besides a slight narrowing upon cooling.

the long component, which corresponds to the thermalized emission of the three triplet substates.

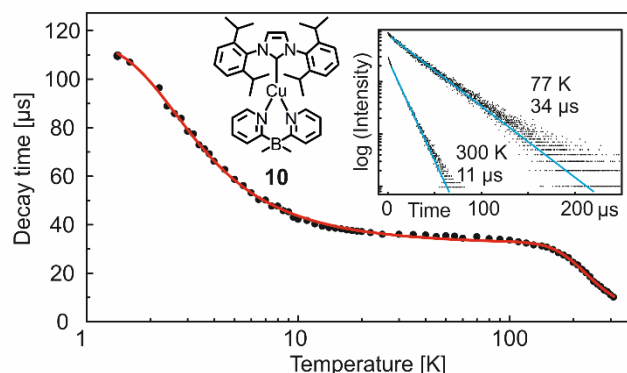


**Fig. 18.** Emission decay time of Cu(IPr)(py<sub>2</sub>-BMe<sub>2</sub>) **10** versus temperature. The sample (powder) was excited at  $\lambda_{exc} = 378$  nm and the detection was at  $\lambda_{exc} = 490$  nm. The red line represents a fit of eq. (5) to the experimental data. Fit parameters are:  $\tau(I) \approx \tau(II) = 116 \mu s$ ,  $\tau(III) = 13 \mu s$ ,  $\tau(S_1) = 160$  ns,  $\Delta E(III-I) = 4$  cm<sup>-1</sup>, and  $\Delta E(S_1-T_1) = 740$  cm<sup>-1</sup>. The inset shows decay curves at T = 77K and 300 K. Adapted with permission from [45]. Copyright (2014) American Chemical Society.

At temperatures between 1.3 K and 10 K a significant reduction of the decay time from 110 to  $\approx 40 \mu s$  is observed for compound **10**. A similar behavior is well-known from other transition metal compounds, such as Ir(III), Pt(II), and Au(I) compounds, and can be related to the zero field splitting (ZFS) of the triplet state T<sub>1</sub>. [2,4,57,59,60,173,180, 183,184,194-198] Apart from the fast SLR component (see below), the emission decay time is governed by a Boltzmann distribution between the three triplet substates I, II, and III. According to the mono-exponential decay, these states are in a thermal equilibrium (after several  $\mu s$  [181], p. 194]). Thus, at very low temperature (T = 1.3 K), the emission stems dominantly from the energetically lowest substate I (and II), whereas with slightly increasing temperature, the higher lying triplet substate III is thermally populated. Since the radiative rates corresponding to the transitions from the energetically higher lying triplet substates (e.g. substate III) to the ground state S<sub>0</sub> are frequently larger than the rates corresponding to the lowest substate(s), the averaged

emission decay time decreases with increasing temperature. [4,44,57,59,60,173,180,181,194] From  $T = 10$  K to about 100 K, the emission decay decreases very slowly with increasing temperature forming a “plateau” with an average value of 34  $\mu\text{s}$  (measured at 77 K). Above 100 K, a further significant decrease of the decay time to 11  $\mu\text{s}$  at  $T = 300$  K is observed. Since the quantum yield does not follow this trend, decreasing only slightly from 91 % at 77 K to 76 % at ambient temperature (Table 4), this reduction of the  $\tau$  values indicates that TADF becomes operative due to a thermal population of the energetically higher lying and short-lived  $S_1$  state. Additionally, a blue shift of the emission from  $\lambda_{\text{max}} = 490$  nm (at 77 K) to 475 nm (300 K) occurs as the  $S_1$  state lies energetically higher than the  $T_1$  state.

The measured data, as displayed in Figure 18, can be fitted with a modified Boltzmann type function (eq. 5) [44,45].

$$\begin{aligned} \tau(T) = & \\ = & \left[ 1 + e^{-\frac{\Delta E(\text{II-I})}{k_B T}} + e^{-\frac{\Delta E(\text{III-I})}{k_B T}} + e^{-\frac{\Delta E(S_1-T_1)}{k_B T}} \right] \times \\ \times & \left[ \tau(\text{I})^{-1} + \tau(\text{II})^{-1} e^{-\frac{\Delta E(\text{II-I})}{k_B T}} + \tau(\text{III})^{-1} e^{-\frac{\Delta E(\text{III-I})}{k_B T}} + \tau(S_1)^{-1} e^{-\frac{\Delta E(S_1-T_1)}{k_B T}} \right]^{-1} \end{aligned} \quad (5)$$

In this equation,  $\tau(T)$  refers to the emission decay time at a given temperature  $T$ ,  $\tau(\text{I})$ ,  $\tau(\text{II})$ , and  $\tau(\text{III})$  represent the individual decay times of triplet substates I, II, and III,  $\Delta E(\text{III-I})$  and  $\Delta E(\text{II-I})$  are the energy separations between the triplet substates.  $\tau(S_1)$  is the decay time of the singlet state  $S_1$ , and  $\Delta E(S_1-T_1)$  is the energy separation between the  $S_1$  and  $T_1$  state.  $k_B$  is the Boltzmann constant.

The fitting procedure results in  $\Delta E(\text{ZFS}) = \Delta E(\text{III-I}) = 4 \text{ cm}^{-1}$ . This value is relatively large for a Cu(I) complex. (Compare compound **13**, section 6.1.) However, by this procedure, it could not be determined where substate II is energetically located with respect to substates I and III. If it is assumed that the substates I and II are very close in energy, i.e.  $\Delta E(\text{II-I}) \approx 0 \text{ cm}^{-1}$ , the emission decay times of the three triplet substates of  $\tau(\text{I}) \approx \tau(\text{II}) = 116 \text{ }\mu\text{s}$  and  $\tau(\text{III}) = 13 \text{ }\mu\text{s}$  are obtained. These results, especially the value of  $\Delta E(\text{ZFS}) = 4 \text{ cm}^{-1}$  and the average emission decay time of  $\tau_{\text{av}} = 32 \text{ }\mu\text{s}$  (determined by use of eq. (4) with  $\tau(\text{I}) = \tau(\text{II}) = 116 \text{ }\mu\text{s}$  and  $\tau(\text{III}) = 13 \text{ }\mu\text{s}$ ) match well with an empirical ordering scheme that correlates  $\Delta E(\text{ZFS})$  with the average phosphorescence decay time.[2,4,183] Such a correlation is possible, since both values are largely determined by the efficiency of SOC.[2,4,183] From this perspective, it is not surprising that a ZFS of  $4 \text{ cm}^{-1}$  is found for a compound with a relatively short triplet decay time of  $32 \text{ }\mu\text{s}$ . For completeness, the observed short component of  $2 \text{ }\mu\text{s}$  at  $T = 1.3 \text{ K}$ , resulting from a relatively slow SLR time, fits well to the small zero-field splitting of  $4 \text{ cm}^{-1}$ . Details of this correlation are discussed in Refs [59,180, 181]. In sections 6 and 7, we will discuss effects of SOC in more detail.

The energy splitting between the triplet  $T_1$  and singlet state  $S_1$  is  $\Delta E(S_1-T_1) = 740 \text{ cm}^{-1}$  (92 meV). This value is in good agreement with the blue shift of the emission spectrum when heating from 77 to 300 K amounting to about  $650 \text{ cm}^{-1}$ . The emission decay time of the singlet state  $S_1$  is  $\tau(S_1) = 160 \text{ ns}$  emphasizing the singlet nature of this state. It is remarked that in contrast to the delayed fluorescence, a prompt fluorescence was not observed for this compound as intersystem crossing from the  $S_1$  to the  $T_1$  state, probably being of the order of 10 ps, [81,123,124,133,165,166] is much faster than the prompt  $S_1 \rightarrow S_0$  emission.

Remarkably, the decrease of the emission decay time with increasing temperature due to an activation of the singlet  $S_1$  state by factor of three is significantly less pronounced than that for the complexes **2** and **8** discussed in section 4.1 and many other TADF Cu(I) complexes. (Compare also Table 7 below.) For example, Cu(dppb)(pz<sub>2</sub>Bph<sub>2</sub>) **2** shows a TADF induced increase of the radiative rate by a factor as large as 250. [67] However, the  $T_1 \rightarrow S_0$  transition of the later complex with  $\tau(T_1) = 1.2$  ms is strongly forbidden, whereas complex **10** exhibits a much shorter  $T_1$  decay time of only 34  $\mu$ s, due to stronger SOC to higher lying singlet states. Therefore, complex **10** is much less susceptible to a reduction of the decay time by involving the TADF process at higher temperatures.

Complex **10a** displays a similar decay behavior as compound **10** at temperatures below 100 K. The (thermalized) decay time drops drastically from about 1 ms at 1.3 K to  $\approx 60$   $\mu$ s at 5 K. (Figure 19) Above  $T \approx 30$  K, the decay time is almost constant and forms a plateau with a value of  $\tau \approx 20$   $\mu$ s up to 300 K. In contrast to the behavior of compound **10**, no distinct reduction of the decay time at  $T > 100$  K is observed. Also the radiative rate with  $k^r \approx 4 \cdot 10^4$  s<sup>-1</sup> is essentially constant. (Table 4) This allows us to assign the emission of complex **10a** as a phosphorescence stemming from the  $T_1$  state in the entire temperature range up to 300 K. An emission via the TADF mechanism as in the case of complex **10** does not occur indicating that the energy splitting  $\Delta E(S_1-T_1)$  is larger than 3000 cm<sup>-1</sup>, as for such a large value no significant thermal activation is expected at  $T = 300$  K. [45]

Taking into account that the term involving the singlet state  $S_1$  in eq.(5) may be neglected, we obtain the following equation for a Boltzmann type analysis of the experimental  $\tau(T)$  data, similar to that performed for complex **10**: [2,4]

$$\tau(T) = \left[ 1 + e^{-\frac{\Delta E(\text{II-I})}{k_B T}} + e^{-\frac{\Delta E(\text{III-I})}{k_B T}} \right] \times \left[ \tau(\text{I})^{-1} + \tau(\text{II})^{-1} e^{-\frac{\Delta E(\text{II-I})}{k_B T}} + \tau(\text{III})^{-1} e^{-\frac{\Delta E(\text{III-I})}{k_B T}} \right]^{-1} \quad (6)$$

The different terms are defined below eq. (5).

A fitting procedure of this equation to the experimentally determined decay times gives  $\Delta E(\text{ZFS}) = \Delta E(\text{III-I}) = 5 \text{ cm}^{-1}$ , which is even slightly larger than that of complex **10**. [45]

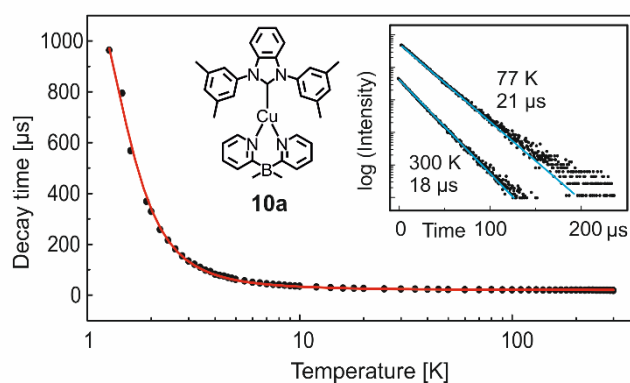


**Fig. 19.** Emission decay time of  $\text{Cu}(\text{Bzi-3,5Me})(\text{py}_2\text{-BMe}_2)$  **10a** (powder) *versus* temperature. The sample was excited at  $\lambda_{\text{exc}} = 355 \text{ nm}$  and the emission was detected at  $600 \text{ nm}$ . The red line represents a fit of eq. (6) to the experimental data. Fit parameters are:  $\tau(\text{I}) \approx \tau(\text{II}) = 1.5 \text{ ms}$ ,  $\tau(\text{III}) = 7 \text{ } \mu\text{s}$ , and  $\Delta E(\text{III-I}) = 5 \text{ cm}^{-1}$  (with  $\Delta E(\text{II-I}) \approx 0 \text{ cm}^{-1}$ ). The inset shows decay curves at  $T = 77 \text{ K}$  and  $300 \text{ K}$ .<sup>7</sup> Adapted with permission from [45]. Copyright (2014) American Chemical Society.

It is concluded that despite seemingly similar chemical composition of the two compounds, only complex **10**, but not complex **10a**, exhibits thermally activated delayed fluorescence. In fact, as summarized in Figure 20, complex **10** exhibits at

<sup>7</sup> The decay behavior at  $T = 1.3 \text{ K}$  (not reproduced in Figure 19, but see Ref. [45]), consists of a short component of  $\tau(\text{SLR}) = 2 \text{ } \mu\text{s}$  and a thermalized component of about  $1 \text{ ms}$ .

ambient temperature *two radiative decay paths* which are thermally equilibrated: one via the S<sub>1</sub> state as TADF and one via the T<sub>1</sub> state as phosphorescence. Complex **10a** exhibits *only phosphorescence* even at ambient temperature.

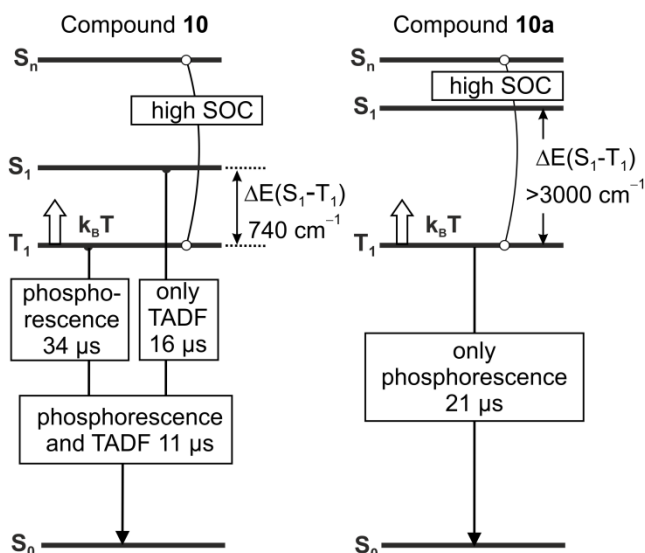


**Fig. 20.** Energy level diagrams of Cu(IPr)(py<sub>2</sub>-BMe<sub>2</sub>) **10** and Cu(Bzl-3,5Me)(py<sub>2</sub>-BMe<sub>2</sub>) **10a** (powders). At ambient temperature, compound **10a** shows only emission from the triplet state, while compound **10** additionally exhibits TADF. The triplet states exhibit zero-field splittings as large as 4 and 5 cm<sup>-1</sup> for compounds **10** and **10a**, respectively, (not displayed in the diagram) reflecting effective spin orbit coupling of the T<sub>1</sub> state to higher singlet and triplet states. The phosphorescence decay times result from the decay in the plateau region. The combined emission decay represents the measured value at T = 300 K, while the “only TADF” decay time is calculated according to:  $\tau(\text{phosphorescence and TADF})^{-1} = \tau(\text{phosphorescence})^{-1} + \tau(\text{only TADF})^{-1}$ . [45]

#### 4.2.2 Tuning of TADF by variation of the torsion angle

The observation of distinctly different energy separations  $\Delta E(S_1-T_1)$  for the complexes **10** and **10a** with “similar” chemical formulas was a surprising result. The compounds differ in two aspects: (i) Size of the  $\pi$ -aromatic system of the N-heterocyclic carbene (NHC) ligands: simple five-member imidazole ring of IPr in **10** versus a fused

benzimidazole of Bzl-3,5Me in **10a**. (ii) Aliphatic substituents on the pendant phenyl rings of the NHC ligands: *i*-propyl groups at the 2,6-positions in IPr of **10** versus methyl groups at the 3,5-positions in Bzl-3,5Me (**10a**). In particular, the latter difference is unlikely to have strong (electronic) impact on the singlet-triplet splitting. However, the alkyl groups can exert steric control over the mutual orientation of the two ligands towards each other. Indeed, as it can be seen in Figure 21, the IPr and py<sub>2</sub>-BMe<sub>2</sub> ligands in molecule of **10** are almost coplanar, whereas in complex **10a**, a significant twist around the Cu-C bond connecting Cu(I) with the NHC ligand occurs. This is expressed by large torsion angles between the Bzl-3,5Me and py<sub>2</sub>-BMe<sub>2</sub> ligand planes of  $\angle \text{N-C-Cu-N}$  being as large as 62° to 71°, as revealed by an x-ray diffraction study (two molecules in the unit cell of **10a**). [66]

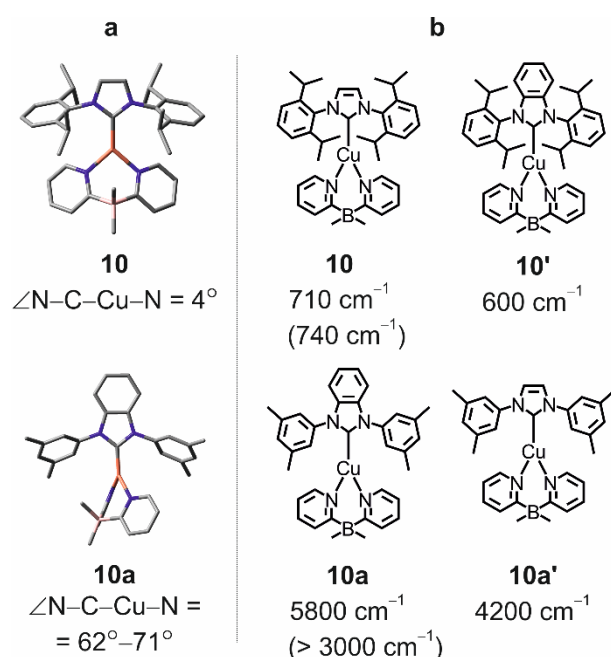


**Fig. 21.** (a) Perspective drawings of the molecules **10** and **10a** as obtained from x-ray crystal analyses (hydrogen atoms are omitted for clarity) [66]. Below the structures torsion angles between the planes of the ligands  $\angle \text{N-C-Cu-N}$  are given. (b) Chemical structures of compounds **10**, **10a**, **10'**, and **10a'** for which TD-DFT calculations were performed. [45] Below the formulas, the calculated singlet-triplet separations  $\Delta E(S_1-T_1)$  are given and compared with the  $\Delta E(S_1-T_1)$  values obtained from experimental investigations (in brackets), described in section 4.2.1.



In order to determine which of the above structural aspects is decisive for the magnitude of the singlet-triplet splitting of the complexes **10** and **10a**, TD-DFT calculations were performed for these molecules and two modified versions shown in Figure 21. Compound **10'** was designed by extending the imidazole ring of IPr to benzimidazole and in compound **10a'** the benzimidazole moiety was replaced by imidazole. All other groups were left unchanged. The compounds **10** and **10'** exhibit similarly small singlet-triplet gaps of 710 and 600 cm<sup>-1</sup>, respectively, matching well with the value of  $\Delta E(S_1-T_1) = 740 \text{ cm}^{-1}$  determined experimentally for **10** (compare section 4.2.1). For both compounds **10a** and **10a'**, large  $\Delta E(S_1-T_1)$  values of 5800 and 4200 cm<sup>-1</sup>, respectively, were obtained. These results indicate that an expansion of the  $\pi$ -system of the NHC ligand does not have any significant impact on the singlet-triplet splitting.

On the other hand, the influence of the ligand orientations relative to each other on the singlet-triplet splitting can be examined using a model compound **10''** (Figure 22), in which the isopropyl groups were removed from the IPr ligand. Using this model compound allows for systematic variation of the torsion angle between the planes of the ligands  $\angle N-C-Cu-N$  without encountering steric hindrance from the adjacent py<sub>2</sub>-BMe<sub>2</sub> ligand. The N-C-Cu-N torsion angle of **10''** was then fixed at values between 0° and 100° in steps of 10° for a DFT ground state geometry optimization. These calculations showed that the spatial distribution of the HOMO changes with the variation of the torsion angle from being almost exclusively localized on the copper ion and the py<sub>2</sub>-BMe<sub>2</sub> for an N-C-Cu-N torsion angle of 0°, to being significantly extended also onto the imidazole ring at an angle of 90°. This is in contrast to the LUMO, which is localized

on the 2,5-diphenylimidazole NHC ligand independently of the torsion angle. (Compare Figure 22.)

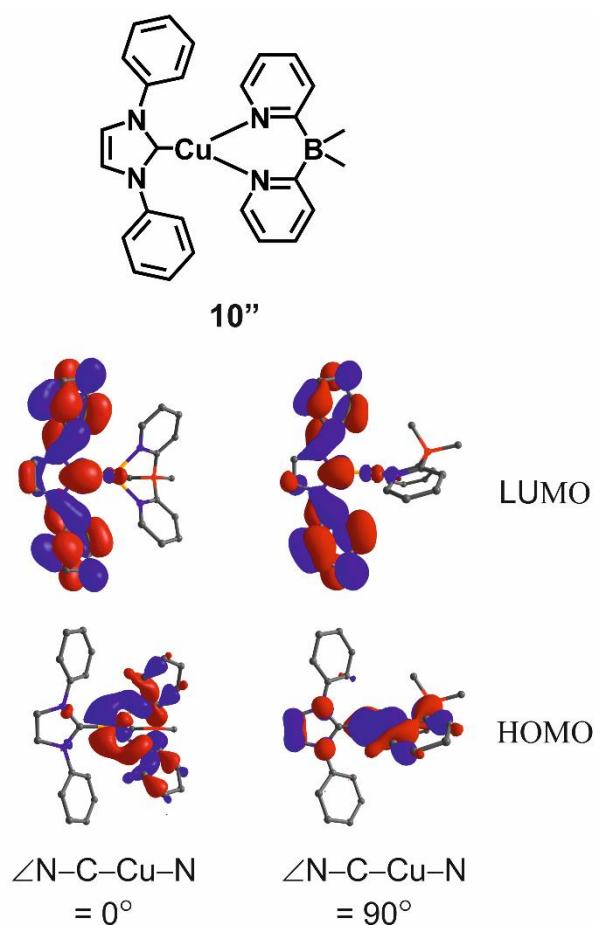


**Fig. 22** Chemical formula of the model compound **10''** and HOMOs and LUMOs of **10''** displayed for a torsion angle between the planes of the ligands  $\angle N-C-Cu-N$  of  $0^\circ$  and  $90^\circ$ , respectively. [45]

The difference in the HOMO distribution is due to the angular relation between the metal d and imidazole  $\pi$ -orbitals. When the NHC and  $py_2$ -BMe<sub>2</sub> ligands are coplanar, the two sets of orbitals are orthogonal and thus do not electronically couple to each other. However, in the perpendicular orientation, the orbitals have the appropriate symmetry to conjugate and delocalize over both ligands. Consequently, spatial overlap between the HOMO and LUMO is small when the torsion angle  $\angle N-C-Cu-N$  is  $0^\circ$ , whereas a significant spatial overlap exists with  $\angle N-C-Cu-N$  of  $90^\circ$ . Since the lowest

excited singlet  $S_1$  and triplet  $T_1$  states are largely comprised from transitions between these frontier orbitals, variations of the degree of overlap will strongly alter the exchange interaction and thus, the value of  $\Delta E(S_1-T_1)$ . According to these model calculations, the magnitude of the singlet-triplet splitting in the studied three-coordinate complexes displays a minimum for the torsion angle between the two ligands of  $0^\circ$  giving a small value (calculated  $\Delta E(S_1-T_1) = 540 \text{ cm}^{-1}$ ) and reaches a maximum ( $\Delta E(S_1-T_1) = 4700 \text{ cm}^{-1}$ ), when the ligands are perpendicular towards each other. (Figure 23) [45]

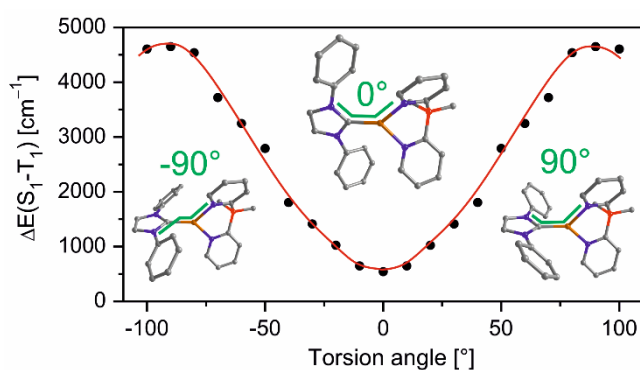


**Fig. 23** Dependence of the  $\Delta E(S_1-T_1)$  splitting on the torsion between the two ligands in the model compound **10''** as obtained from TD-DFT calculations. Adapted with permission from [45]. Copyright (2014) American Chemical Society.

Summing up, the case study presented in this section reveals a strong dependence of  $\Delta E(S_1-T_1)$  on the orientation of the two ligands towards each. In this regard, it should be mentioned that for a different compound (the  $\text{py}_2\text{-BMe}_2$  ligand was replaced by phenanthroline) quantum mechanical calculations do not show any significant  $\Delta E(S_1-T_1)$  dependence on the torsion angle, though the down- and up-ISC (RISC) rates vary distinctly. [199] Obviously, for engineering of emitters with optimized TADF properties, angle dependences have to be taken into account in different contexts, i.e.

with respect to steric control to reduce excited state distortions that induce non-radiative relaxations (section 3) and the above mentioned effects.

## 5. Singlet-triplet splitting and fluorescence rate

As already discussed above, thermally activated delayed fluorescence represents a promising way to reduce emission decay times as the emission occurs from the thermally populated spin-allowed  $S_1 \rightarrow S_0$  transition in contrast to the mostly very weak  $T_1 \rightarrow S_0$  transitions. The TADF decay time strongly depends on the energy splitting  $\Delta E(S_1-T_1)$  between the first excited singlet  $S_1$  and triplet  $T_1$  state. The smaller this energy separation is, the more effective is the thermal population of the  $S_1$  state at ambient temperature. A pronounced population of the  $S_1$  state leads to a shorter emission decay time. Consequently, as discussed above, many efforts have been made to minimize the singlet triplet-splitting in order to increase the TADF efficiency. The smallest splitting reported so far is as low as  $270 \text{ cm}^{-1}$  (compound **1** [5]). However, for this compound, the decay time of the  $S_1$  state was as long as 570 ns [5]. This raises the question, whether it is sufficient to focus on the minimization of the energy splitting. In fact, in this section, we will show that the transition dipole moment  $\vec{\mu}(S_1 \rightarrow S_0)$  and hence, the radiative decay rate  $k^r(S_1)$  of the  $S_1 \rightarrow S_0$  transition represents another important criterion. In particular, this rate should be as large as possible to achieve a short TADF decay time. (Compare section 2.) We will show that this is not the case, as a small singlet-triplet energy splitting is bought at the cost of a small  $S_1 \rightarrow S_0$  oscillator strength (radiative rate).

### 5.1 Theoretical considerations

In this section, we will present a qualitative model that may explain why a small splitting between the lowest singlet and triplet state  $\Delta E(S_1-T_1)$  is related to a small radiative rate

$k^r(S_1)$  of the  $S_1 \rightarrow S_0$  transition. The model is based on the assumption that the states  $S_1$  and  $T_1$  can be approximated by a one-electron transition from HOMO  $\varphi_H$  to LUMO  $\varphi_L$ , such that further excited singlet and triplet states are lying substantially higher in energy. In this simple model, we also assume that non-radiative relaxation processes or intermolecular interactions can be neglected, and that a common set of real orbitals is chosen for the states  $S_0$ ,  $S_1$ , and  $T_1$ .

In such a situation, one can obtain both  $\Delta E(S_1-T_1)$  and  $k^r(S_1)$  from integrals over the product of HOMO  $\varphi_H$  and LUMO  $\varphi_L$ . This product

$$\rho_{H,L}(\vec{r}) = \varphi_H(\vec{r}) \cdot \varphi_L(\vec{r}) \quad (7)$$

is called the "transition density". The radiative rate  $k^r(S_1)$  may be obtained from the electric dipole transition moment  $\vec{\mu}(S_1-S_0)$  given approximately by  $\vec{\mu}_{H,L}$  defined as

$$\vec{\mu}_{H,L} = e \int \varphi_H(\vec{r}) \vec{r} \varphi_L(\vec{r}) d^3r = e \int \rho_{H,L}(\vec{r}) \vec{r} d^3r \quad (8)$$

Thus, the radiative rate for spontaneous (prompt) emission is given by (see [200], p.159 and Appendix A)

$$\begin{aligned} k_r(S_1) &= C_k \nu^3 n^3 |\vec{\mu}(S_1 - S_0)|^2 \\ &= 2C_k \nu^3 n^3 |\vec{\mu}_{H,L}|^2 \\ &= 2e^2 C_k \nu^3 n^3 \left| \int \rho_{H,L}(\vec{r}) \vec{r} d^3r \right|^2 \end{aligned} \quad (9)$$

Here,  $C_k$  is a numerical constant given by  $16\pi^3/(3\epsilon_0 h c^3)$  with  $\epsilon_0$  the vacuum permittivity,  $h$  Planck's constant, and  $c$  the velocity of light. In this equation,  $\nu = \Delta E(S_1-S_0)/h$  is the

transition frequency and  $n$  is the refractive index. Thus, we see that the radiative rate is essentially related to the square of the transition density.

The energy separation  $\Delta E(S_1-T_1)$  between  $S_1$  and  $T_1$ , on the other hand, is well approximated by twice the exchange integral  $K_{H,L}$  for HOMO and LUMO. ([143], p. 86)

Thus, we have

$$\Delta E(S_1 - T_1) \approx 2K_{H,L} \quad (10)$$

where the exchange integral  $K_{H,L}$  for HOMO  $\varphi_H$  and LUMO  $\varphi_L$  can be expressed in terms of the transition density  $\rho_{H,L}$ :

$$\begin{aligned} K_{H,L} &= c_K \int \varphi_H(\vec{r}_1)\varphi_L(\vec{r}_2) \frac{1}{|\vec{r}_2 - \vec{r}_1|} \varphi_H(\vec{r}_2)\varphi_L(\vec{r}_1) d^3r_1 d^3r_2 \\ &= c_K \int \varphi_H(\vec{r}_1)\varphi_L(\vec{r}_1) \frac{1}{|\vec{r}_2 - \vec{r}_1|} \varphi_H(\vec{r}_2)\varphi_L(\vec{r}_2) d^3r_1 d^3r_2 \\ &= c_K \int \rho_{H,L}(\vec{r}_1) \frac{1}{|\vec{r}_2 - \vec{r}_1|} \rho_{H,L}(\vec{r}_2) d^3r_1 d^3r_2 \end{aligned} \quad (11)$$

Here,  $c_K = e^2/(4\pi\epsilon_0)$  is a numerical constant.

Note that the exchange integral can be interpreted as the electrostatic interaction of the transition density  $\rho_{H,L}$  with itself. The important observation is that also the exchange integral is quadratically dependent on the transition density. (See eq. (11).)

The common quadratical dependence on the transition density already explains qualitatively why small  $\Delta E(S_1-T_1)$  and small  $k^r(S_1)$  are related: A small transition density implies that both  $\Delta E(S_1-T_1)$  and  $k^r(S_1)$  are small.

We will discuss qualitatively several reasons, why the transition density is small. For this discussion, we assume a Linear Combination of Atomic Orbitals (LCAO) type description of HOMO and LUMO: Each molecular orbital (MO) is a linear combination of basis functions (AOs) that are multiplied by the so-called MO coefficients. The AOs are centered at the atomic nuclei of the molecule under consideration. There are several reasons why the transition density may be small:

#### *Exponential tails*

Due to the exponential decay of the basis functions, the transition density vanishes outside a small spatial region where some atoms supporting HOMO and LUMO are close. This region is particularly small if HOMO and LUMO do not have supporting atoms in common (charge transfer situation).

#### *Small MO coefficients*

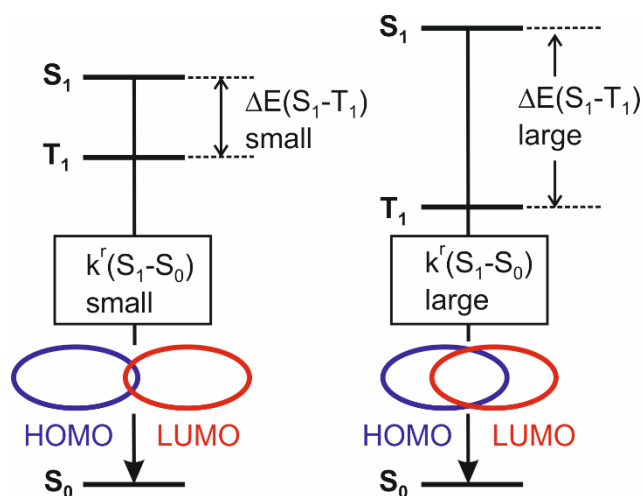
The MO coefficients can be small even in the small region mentioned above in the case that the main contributions to HOMO and LUMO are well separated in space. For normalized basis functions (AOs), small MO coefficients imply that the contributions of the AOs with such coefficients to be unimportant in the transition density. If the MO coefficients for HOMO or LUMO are small or even zero for neighboring atoms, next-nearest neighbor contributions have to be considered. These, however, are small due to the exponential decay of the AOs. Note that the MO coefficients depend on the geometry of the state under consideration. Of special importance in this context are the angular dependencies as discussed in section 4.2.2. This implies that the shape and

the spatial overlap of HOMO and LUMO change as a function of the torsion angle of the involved ligand(s).

Both reasons for small transition densities are depicted schematically in Figure 24 as "small overlap" of HOMO and LUMO.

Thus, the transition density is small in absolute value in spatial regions where at least one of the two orbitals  $\varphi_H$  and  $\varphi_L$  is small in absolute value. If the HOMO and LUMO are large in spatial regions that do not overlap, then the transition density is nothing but the product of the exponentially decaying tails of HOMO and LUMO, and this implies that the transition density is small.<sup>8</sup>

In order to illustrate this further, we display HOMO and LUMO orbitals of complex **8** that have been computed in the  $T_1$  geometry using the B3LYP density functional. (Figure 25) It is seen that in most spatial regions at least one of the two orbitals is vanishing which means that the transition density is only of importance in a small region where both orbitals are not vanishing. Note that in Figure 25, the product of orbitals is twenty times enlarged as compared to the contour amplitudes of HOMO and LUMO.



<sup>8</sup> We note that the modified overlap  $O = \int |\varphi_H| |\varphi_L| dV$  is a quantitative measure for the spatial overlap. [201]



**Fig. 24** Schematic illustration of the correlation of energy splitting  $\Delta E(S_1-T_1)$  between first excited singlet  $S_1$  and triplet  $T_1$  state and the radiative decay rate  $k^r(S_1 \rightarrow S_0)$  on the spatial overlap of HOMO and LUMO.

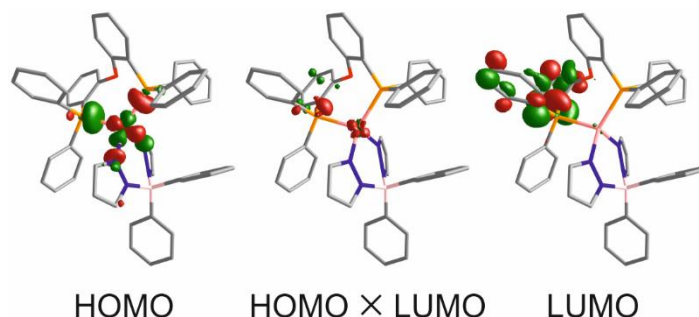


**Fig. 25** HOMO and LUMO orbitals (isovalue 0.05) of  $\text{Cu}(\text{pop})(\text{pz}_2\text{Bph}_2)$  **8** as computed in the  $T_1$  geometry at the B3LYP/def2-svp level of theory [150,151]. In the middle of the diagram, the transition density  $\rho_{H,L}$ , given by the product of the frontier orbitals HOMO  $\times$  LUMO, is displayed (twenty times enlarged with an isovalue of 0.0025). The transition density is only non-vanishing in the region where both HOMO and LUMO do not vanish.

Instead of using an LCAO-type description of HOMO and LUMO, the smallness of the transition density may also be described by representing the MOs by linear combinations of orbitals localized in different spatial regions. Within such an approach, the intensities of charge-transfer bands of ferrous, ferric, and cuprous phenanthroline complexes were explained.[202,203]

In conclusion, the presented qualitative model clearly shows that the  $\Delta E(S_1-T_1)$  value and the transition rate of the prompt fluorescence  $k^r(S_1 \rightarrow S_0)$  are related and that both quantities depend quadratically on the transition density, as defined in eq. (7). A general analytical relation between these quantities could not be given. However, an experimentally based correlation, as discussed in the next section, will show that such a relation exists for many Cu(I) complexes with low lying charge transfer transitions.

## 5.2 Experimental correlation of $\Delta E(S_1-T_1)$ and $S_1 \rightarrow S_0$ allowedness

In order to experimentally investigate the question raised in the previous section, the decay time of the first excited singlet  $S_1$  as well as the energy separation between the singlet and triplet state have been determined for many Cu(I) compounds in the last years. These results, deduced from measurements of the emission decay time in dependence of the temperature  $T$  (see section 4), are summarized in Table 5 and reveal an interesting trend that will be discussed in the following.

**Table 5:** Energy splitting  $\Delta E(S_1-T_1)$  between the first excited singlet  $S_1$  and triplet  $T_1$  state, the decay time of the singlet state  $\tau(S_1)$ , the photoluminescence quantum yield at ambient temperature  $\Phi_{PL}(300\text{ K})$ , and the radiative rate  $k^r(S_1 \rightarrow S_0) = k^r(S_1)$  (calculated according to eq. (3)).

	Compound	$\Delta E(S_1-T_1)$ [cm <sup>-1</sup> ]	$\tau(S_1)$ [ns]	$\Phi_{PL}$ (300 K)	$k^r(S_1)$ [10 <sup>6</sup> s <sup>-1</sup> ]	Ref.
1	Cu <sub>2</sub> I <sub>2</sub> [MePyrPHOS](PPh <sub>3</sub> ) <sub>2</sub>	270	570	0.97	1.7	[5]
2	Cu(dppb)(pz <sub>2</sub> Bph <sub>2</sub> )	370	180	0.70	3.9	[67]
3	[Cu(μ-Cl)(PNMe <sub>2</sub> ) <sub>2</sub> ]	460	210	0.45	2.1	[73]
4	[Cu(μ-Br)(PNMe <sub>2</sub> ) <sub>2</sub> ]	510	110	0.65	5.9	[73]
5	[Cu(μ-I)(PNMe <sub>2</sub> ) <sub>2</sub> ]	570	90	0.65	7.2	[73]
6	Cu <sub>2</sub> Cl <sub>2</sub> (dppb) <sub>2</sub>	600	70	0.35	5.0	[69]
7	[Cu(μ-I)(PNpy)] <sub>2</sub>	630	100	0.65	6.5	[73]
8	Cu(pop)(pz <sub>2</sub> BPh <sub>2</sub> )	650	170	0.9	5.3	[2, 63]
9	Cu(pop)(tmbpy) <sup>+</sup>	720	160	0.55	3.4	[72]
10	(IPr)Cu(py <sub>2</sub> -BMe <sub>2</sub> )	740	160	0.76	4.8	[45]
11	[Cu(PNP <sup>i</sup> Bu)] <sub>2</sub>	786	138	0.57	4.1	[38]
12	Cu <sub>2</sub> I <sub>2</sub> (MePyrPHOS)(dpph)	830	190	0.88	4.6	[5]
13	Cu <sub>2</sub> Cl <sub>2</sub> (N <sup>^</sup> P) <sub>2</sub>	930	40	0.92	23	[44]
14	CuCl(PPh <sub>3</sub> ) <sub>2</sub> (4-Mepy)	940	47	0.99	21	[74]
15	Cu(dmp)(phanephos) <sup>+</sup>	1000	40	0.80	20	[61]
16	Cu(pop)(pz <sub>4</sub> B)	1000	80	0.9	11	[63]
17	CuBr(PPh <sub>3</sub> ) <sub>2</sub> (4-Mepy)	1070	41	0.95	23	[74]
18	CuI(PPh <sub>3</sub> ) <sub>2</sub> (4-Mepy)	1170	14	0.66	47	[74]
19	Cu(pop)(pz <sub>2</sub> BH <sub>2</sub> )	1300	10	0.45	45	[4, 63]

Figure 26 displays the experimentally determined data from Table 5, showing a plot of  $k^r(S_1)$  versus  $\Delta E(S_1-T_1)$ . Indeed, it is seen that with decreasing  $\Delta E(S_1-T_1)$  also the allowedness of the  $S_1 \rightarrow S_0$  transition (radiative decay rate  $k^r(S_1)$ ) decreases. This might have an important consequence on the emission decay time of a TADF complex at ambient temperature, as can be illustrated by a very simple consideration using eq. (1). As has been shown in a simple estimate using the experimental fit curve displayed in Figure 26 and the expression giving the  $\tau(\text{TADF})$  based on eq. (1), a minimum TADF decay time of several  $\mu\text{s}$  is obtained. [204]

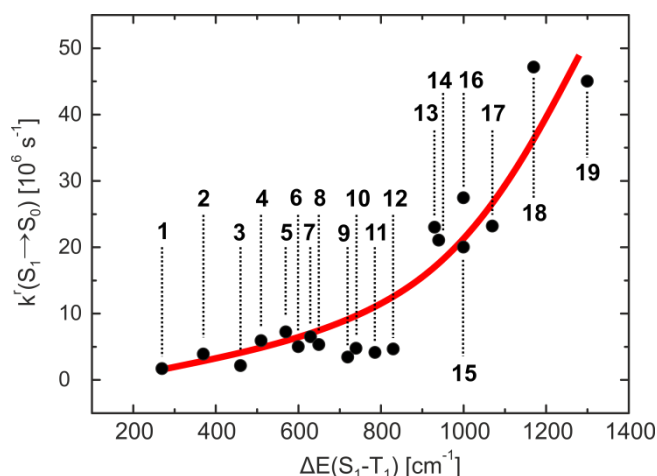


**Fig. 26** Radiative decay rate  $k^r(S_1)$  of the  $S_1 \rightarrow S_0$  transition plotted versus the energy splitting  $\Delta E(S_1-T_1)$  between the first excited singlet  $S_1$  and triplet  $T_1$  state. The data points are taken from Table 5. The fit curve represents an exponential function as guide for the eye.

The simple model presented explains the experimental results. Thus, its basic assumption of energetically (from higher lying states) well separated  $S_1$  and  $T_1$  states derived from a HOMO-LUMO excitation seems to describe the basic physics of the systems under consideration. However, it does not contain effects induced by

configuration interaction (CI). By these interactions higher lying singlets with higher oscillator strengths mixing to the  $S_1$  state can increase the radiative rate  $k^r(S_1)$ . To investigate Cu(I) complexes exhibiting such CI effects is outside the scope of the present article but may be a fruitful topic for further research. Moreover, the role of spin-orbit coupling is not taken into account in the approach of this section, but it will be shown in the following section that SOC can induce an effective reduction of the overall emission decay time at ambient temperature.

## 6. Combined TADF and phosphorescence – Importance of spin-orbit coupling

Emitter compounds that are applied in OLEDs should exhibit not only high emission quantum yields, but also emission decay times as short as possible, especially, to reduce roll-off effects [112] and to avoid bond-dissociation reactions leading to decomposition of the emitter molecules. [113-115]. In section 4 and in Ref [67], it was shown that the energy separation  $\Delta E(S_1-T_1)$  between the charge transfer states of  $^1MLCT$  ( $S_1$ ) and  $^3MLCT$  ( $T_1$ ) character has crucial importance for a short decay time  $\tau(TADF)$  of the thermally activated delayed fluorescence. However, with decreasing  $\Delta E(S_1-T_1)$ , the oscillator strength of the  $S_0 \leftrightarrow S_1$  transition decreases and thus, the radiative decay time  $\tau(S_1)$  increases. Accordingly,  $\tau(TADF)$  cannot be diminished as preferred. (Compare eq. (1)) This restricting dependence has already been addressed in section 5. Nevertheless, a promising approach to overcome this limitation will be presented in this section. [44, 45, 145]

### Case study based on $Cu_2Cl_2(N^*P)_2$ 13.

An overall faster radiative decay of an emitter showing TADF can be obtained by opening an *additional* radiative decay path from the lowest triplet state. Such a path represents the  $T_1 \rightarrow S_0$  phosphorescence. However, for most Cu(I) complexes, this path is ineffective mainly due to very weak spin-orbit coupling (SOC) of the  $T_1$  state to higher lying singlet states. As a consequence, the phosphorescence decay time is of the order of several hundred  $\mu\text{s}$  and even up to ms. [2,4,5,38,61,65,69,72,73] On the other hand, development of complexes that experience large SOC with respect to the lowest triplet state is not unrealistic. Thus, in this case study, we present properties of the brightly luminescent dinuclear complex  $\text{Cu}_2\text{Cl}_2(\text{N}^*\text{P})_2$  **13** [44,145] (chemical formula shown in Figure 27) exhibiting efficient TADF from the  $S_1$  state *and* direct phosphorescence from the  $T_1$  state both being in a thermal equilibrium. [44] The phosphorescence contributes significantly to the emission even at ambient temperature due to efficient SOC that induces distinct radiative decay from the  $T_1$  state.

A first insight into the electronic structure of  $\text{Cu}_2\text{Cl}_2(\text{N}^*\text{P})_2$  **13** is obtained by DFT and TD-DFT calculations carried out for an optimized  $T_1$  geometry. These allow us to assign the lowest singlet and triplet state as  $^1\text{MLCT}$  ( $S_1$ ) and  $^3\text{MLCT}$  ( $T_1$ ) state, respectively, with an energy separation of  $\Delta E(S_1-T_1) = 940 \text{ cm}^{-1}$  (0.11 eV).<sup>9</sup> This value is small enough to expect a TADF behavior for this compound.

The powder material exhibits a very high emission quantum yield of  $\phi_{\text{PL}} = 92\%$  at ambient temperature. The emission spectrum with a peak maximum at  $\lambda_{\text{max}} = 485 \text{ nm}$  is very broad showing a halfwidth of about  $5 \cdot 10^3 \text{ cm}^{-1}$  (0.62 eV). This is consistent with the MLCT character of the corresponding transition. Upon cooling to  $T \approx 120 \text{ K}$ , the emission red-shifts by  $\Delta\lambda = 25 \text{ nm}$  ( $10^3 \text{ cm}^{-1}$ ; 0.12 eV) to  $\lambda_{\text{max}} = 510 \text{ nm}$ . Further cooling

---

<sup>9</sup> The calculations were carried out using the B3LYB functional with the def2-svp basis set. Previously, it was already shown that applying this method, reliable results were obtained. [205,206]

to  $T = 1.3$  K does not induce any significant spectral change apart from a slight reduction of the halfwidth. Again, no detailed spectral information can be resolved. [44] The red shift is consistent with the TADF behavior, since the TADF is frozen out at low temperature, and thus, only the energetically lower lying phosphorescence is maintained. Again, a deeper insight into the electronic structure of the complex is obtained from the analysis of the emission decay behavior.

Figure 27 displays the temperature dependence of the emission decay time over a temperature range of  $1.3 \text{ K} \leq T \leq 300 \text{ K}$ . The decay at a given temperature is mono-exponential in the whole range. At  $T = 1.3$  K, the emission decay is very long amounting to  $\tau = 3.3$  ms. This is related to a very low transition probability of the lowest triplet substate I to the electronic ground state. With increasing temperature up to  $T \approx 20$  K, the decay time shortens drastically to less than  $\approx 50 \mu\text{s}$ . In this temperature range, properties of the individual substates I, II, and III of the  $T_1$  state are displayed. This behavior is determined by a relatively large zero-field splitting (ZFS) of the  $T_1$  state. [59,180,181] (See below.) With further temperature increase, the decay reaches a plateau near  $T = 50$  K with a decay time of about  $43 \mu\text{s}$  and then, from  $T > 150$  K, decreases to  $8.3 \mu\text{s}$  at  $T = 300$  K. As the emission quantum yield is almost constant over the entire temperature range above  $T \approx 4$  K [44], the decrease of the decay time is assigned to be a consequence of a successive population of higher lying energy states with growing temperature. Above  $T \approx 150$  K, thermal activation of a short-lived state, the  $^1\text{MLCT}$  ( $S_1$ ) state, occurs and becomes dominant towards ambient temperature, giving the TADF.

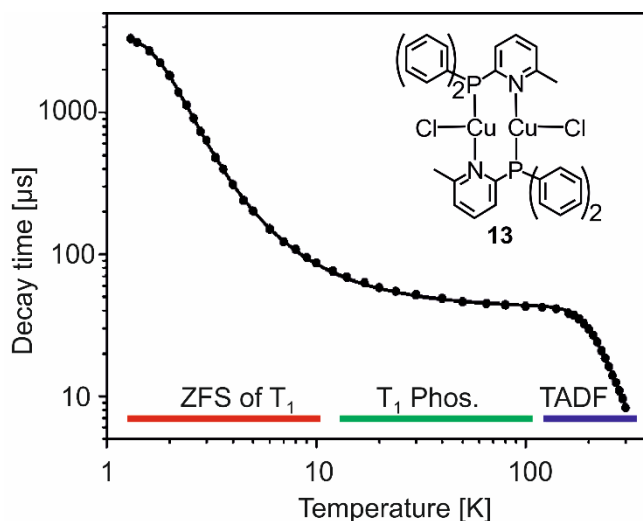


**Fig. 27.** Temperature dependence of the emission decay time of  $\text{Cu}_2\text{Cl}_2(\text{N}^*\text{P})_2$  **13** (powder) and fit curve according to eq. (5). The emission decays mono-exponentially in the whole temperature range. Adapted with permission from [44]. Copyright (2015) American Chemical Society.

A fit of the measured decay time data using eq. (5) gives a very good match (Figure 27) and one obtains the individual decay times and energy separations of the involved states (Figure 28). The splittings of the  $T_1$  state are  $\Delta E(\text{II-I}) = 7 \text{ cm}^{-1}$  and  $\Delta E(\text{III-I}) = 15 \text{ cm}^{-1}$ . A correspondingly large ZFS splitting of  $\Delta E(\text{ZFS}) = 15 \text{ cm}^{-1}$  is unprecedented for Cu(I) complexes investigated so far. This splitting is a consequence of relatively strong SOC from higher lying singlet state(s) (not the  $S_1$  state [2,4,5,57,183,184]). For a more general discussion see section 7. For comparison, the  $\Delta E(\text{ZFS})$  values determined for the compounds **10** and **10a** (section 4.2.1 and [45]) amount to 4-5  $\text{cm}^{-1}$ , which already represent relatively large values as compared to most other Cu(I) compounds.

The emission decay times of the triplet substates of  $\text{Cu}_2\text{Cl}_2(\text{N}^*\text{P})_2$  **13** are determined to  $\tau(\text{I}) = 3.5 \text{ ms}$ ,  $\tau(\text{II}) = 30 \text{ } \mu\text{s}$ , and  $\tau(\text{III}) = 26 \text{ } \mu\text{s}$ , which tells us that the mixing of singlet character to the different triplet substates by SOC is extremely small to substate I, but significant to the substates II and III. The fit gives also the energy separation between the triplet and singlet state of  $\Delta E(\text{S}_1\text{-T}_1) \approx \Delta E(\text{S}_1\text{-I}) = 930 \text{ cm}^{-1}$  (0.115 eV). This value

corresponds very well to the value deduced from the difference of the emission maxima at  $T = 77\text{ K}$  and  $300\text{ K}$  ( $1000\text{ cm}^{-1}$ ) as well as from TD-DFT calculations ( $940\text{ cm}^{-1}$ ). [44] The  $S_1$  decay time is determined to be  $\tau(S_1) = 40\text{ ns}$ . However, this prompt emission was not observed directly. Obviously, the ISC time is much faster than  $40\text{ ns}$ . [81,120,123,124,133] This leads to a fast depopulation of the  $S_1$  state resulting in a population of the lower lying triplet state  $T_1$ . Thus, the prompt fluorescence is (almost) quenched. The time constant of  $40\text{ ns}$  or, more exactly, the related radiative decay rate, amounting to  $k^r(S_1) = k^r(S_1 \leftrightarrow S_0) = 2.3 \cdot 10^7\text{ s}^{-1}$  (according to eq. (3) and  $\phi_{\text{PL}} = 92\%$ ), corresponds to the probability of the transition between the excited singlet state  $S_1$  and the electronic ground state  $S_0$ .

The energy separations and decay times as obtained from the fitting procedure are summarized in the energy level diagram shown in Figure 28.

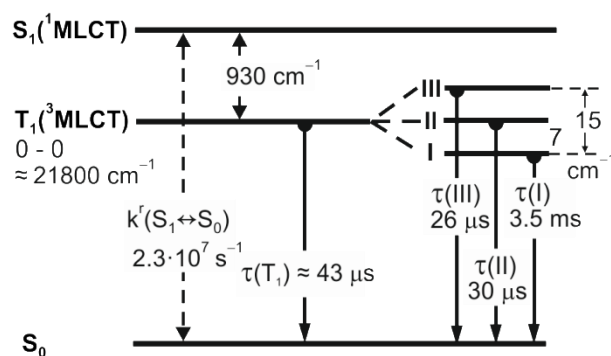


**Fig. 28** Energy level diagram for  $\text{Cu}_2\text{Cl}_2(\text{N}^3\text{P})_2$  **13** (powder). The triplet state exhibits a total zero-field splitting of  $\Delta E(\text{ZFS}) = 15\text{ cm}^{-1}$ . The individual values of the ZFS energies and decay times are determined by a fitting procedure using the data of Figure 27 and eq. (5). Also the  $\Delta E(S_1-T_1)$  energy separation and the fluorescence rate result from this fitting. (Compare [44]).

The relatively short  $T_1$  decay time of  $\tau(T_1) \approx 43\text{ }\mu\text{s}$ , corresponding to a radiative decay rate of  $k^r(T_1) = 2.1 \cdot 10^4\text{ s}^{-1}$ , allows us to conclude that the ambient temperature emission



is composed of the  $T_1$  state emission as phosphorescence and the  $S_1$  state emission as TADF. Thus, two decay paths lead to a combined emission. This behavior is illustrated by discussing the temperature-dependent interplay between TADF and phosphorescence. (Compare [73].) The TADF intensity that originates from the singlet state  $S_1$  is denoted as  $I(S_1)$  and the phosphorescence intensity from the triplet state  $T_1$  as  $I(T_1)$ , respectively, with the total emission intensity of

$$I(\text{total}) = I(S_1) + I(T_1). \quad (12)$$

$I(S_1)$  is proportional to the population of the singlet state  $N(S_1)$  and to the radiative rate constant  $k^r(S_1)$ :

$$I(S_1) = \alpha k^r(S_1) N(S_1) \quad (13)$$

Similarly,  $I(T_1)$  is given by

$$I(T_1) = \alpha k^r(T_1) N(T_1) \quad (14)$$

with  $\alpha$ , a constant, being equal in both equations. The radiative rates  $k^r(S_1)$  and  $k^r(T_1)$  can be expressed in terms of quantum yields and emission decay times according to eq. (3). For this rough estimate, it is assumed that the quantum yields  $\phi_{PL}(S_1)$  and  $\phi_{PL}(T_1)$  do not depend on temperature. Assuming that the populations of both states follow a Boltzmann distribution (fast equilibration), we obtain

$$\frac{I(T_1)}{I_{\text{tot}}} = \left[ 1 + \frac{k^r(S_1)g(S_1)}{k^r(T_1)g(T_1)} e^{-\frac{\Delta E(S_1-T_1)}{k_B T}} \right]^{-1} = \left[ 1 + \frac{\Phi_{PL}(S_1)\tau(T_1)}{3\Phi_{PL}(T_1)\tau(S_1)} e^{-\frac{\Delta E(S_1-T_1)}{k_B T}} \right]^{-1} \quad (15)$$

$g(S_1) = 1$  and  $g(T_1) = 3$  are the degeneracy factors for the singlet and the triplet states, respectively. Using  $I(T_1) = I_{\text{tot}} - I(S_1)$  one obtains:

$$\frac{I(S_1)}{I_{\text{tot}}} = 1 - \left[ 1 + \frac{\Phi_{\text{PL}}(S_1)\tau(T_1)}{3\Phi_{\text{PL}}(T_1)\tau(S_1)} e^{-\frac{\Delta E(S_1-T_1)}{k_B T}} \right]^{-1} \quad (16)$$

By use of the eqs. (15) and (16) and the fit parameters determined for  $\text{Cu}_2\text{Cl}_2(\text{N}^{\wedge}\text{P})_2$  **13** with  $\Delta E(S_1-T_1) = 930 \text{ cm}^{-1}$ ,  $\tau(S_1) = 40 \text{ ns}$ ,  $\tau(T_1) = 43 \text{ }\mu\text{s}$  and assuming  $\phi_{\text{PL}}(S_1) = 0.92$  measured at 300 K [44] and  $\phi_{\text{PL}}(T_1) = 0.97$  measured at 77 K [44], temperature dependent TADF and phosphorescence ratios can be visualized as plotted in Figure 29. At temperatures below  $T \approx 120 \text{ K}$ , only a  $T_1 \rightarrow S_0$  phosphorescence occurs. With temperature increase, the phosphorescence intensity decreases, while the  $S_1 \rightarrow S_0$  TADF grows in. At  $T = 300 \text{ K}$ , about 80% of the emission is of TADF and the remaining 20% of phosphorescence character. For completeness, it is mentioned that both types of emission decay with the same decay time due to fast thermalization between the  $S_1$  and  $T_1$  states following a Boltzmann distribution.

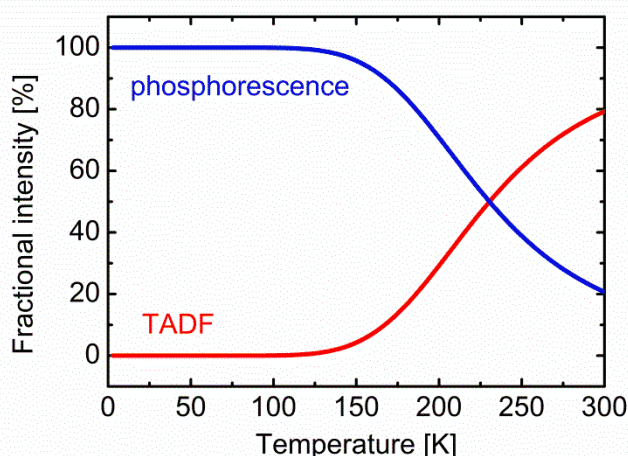


**Fig. 29** Simulation of the fractional emission intensities for  $\text{Cu}_2\text{Cl}_2(\text{N}^{\wedge}\text{P})_2$  **13** (powder). The emission occurs as TADF and phosphorescence, respectively. The calculations were carried out according to eqs. (15) and (16). Compare [44,73].

The discussion presented above, demonstrates that the emission decay time of  $\tau(300\text{ K}) = 8.3\ \mu\text{s}$  is not determined by the TADF process alone but additionally by a phosphorescence process. The corresponding total rate is expressed by

$$k(300\text{ K}) = k(T_1) + k(\text{TADF}) \quad (17a)$$

or

$$k(300\text{ K}) = \tau(300\text{ K})^{-1} = \tau(T_1)^{-1} + \tau(\text{TADF})^{-1} \quad (17b)$$

With the measured value of  $\tau(300\text{ K}) = 8.3\ \mu\text{s}$  and  $\tau(T_1) = 43\ \mu\text{s}$ , we obtain  $\tau(\text{TADF}) = 10.3\ \mu\text{s}$ . Accordingly, the additional radiative  $T_1 \rightarrow S_0$  path leads to a significant reduction of the emission decay time by about 20% compared to the TADF-only process. Such a behavior can improve the emission properties of materials dedicated for a use in OLEDs. In particular, the additional radiative decay path may be useful for a reduction of saturation effects at high current densities and for an increase of the device stability. The corresponding property is related to a combined singlet harvesting and triplet harvesting mechanism. Meanwhile, a number of other Cu(I) compounds have been identified that show similar effects of combined phosphorescence and TADF (compare compound **10** [45] and compounds described in Ref. [5]). The process of the combined emission is illustrated in Figure 30.

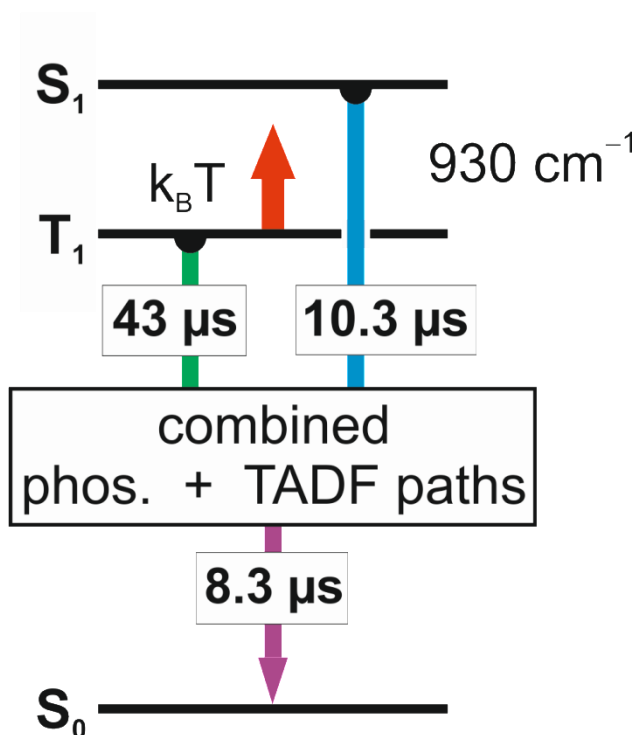


**Fig. 30** Emission decay paths for  $\text{Cu}_2\text{Cl}_2(\text{N}^{\text{P}})_2$  **13** (powder) at ambient temperature occurring as phosphorescence ( $43 \mu\text{s}$ ) and TADF ( $10.3 \mu\text{s}$ ) giving a combined (shortened) emission decay time of  $8.3 \mu\text{s}$ . Adapted with permission from [44]. Copyright (2014) American Chemical Society.

However, most Cu(I) compounds studied so far exhibit long-lived phosphorescence (e.g.  $\tau(T_1) > 200 \mu\text{s}$ ). [2,4,39,67-69,72,73] In this situation, the phosphorescence decay path does not contribute significantly to the overall emission at ambient temperature.

## 7 The triplet state and spin-orbit coupling – A simple approach for Cu(I) compounds

In this section, we present a simple approach that allows for fast screening of Cu(I) compounds with respect to short radiative phosphorescence decay times for the development of materials showing both efficient ambient-temperature phosphorescence and TADF. This approach is based on easily accessible DFT calculations without applying of sophisticated time-dependent calculations that include SOC explicitly.

For Cu(I) compounds, effects of SOC on the lowest triplet state (or more exactly the triplet  $T_1$  substates) are mostly not very distinct. This is not only related to the relatively small SOC constant of copper with  $\xi = 857 \text{ cm}^{-1}$  [108] compared to that of iridium with  $\xi = 3909 \text{ cm}^{-1}$ , but essentially to the extent of mixing of adequate, energetically higher lying singlet states. In a simplified perturbational approach, the radiative rate  $k^r(T_1 \rightarrow S_0)$  for the triplet state  $T_1$  can be expressed by [2,4,183,192,207]

$$k^r(T_1 \rightarrow S_0) \approx \text{const} \cdot \frac{|\langle S_m | H_{SO} | T_1 \rangle|^2}{|E(T_1) - E(S_m)|^2} \cdot |\langle S_0 | e\vec{r} | S_m \rangle|^2 \quad (18)$$

Herein,  $H_{SO}$  is the SOC operator. It is assumed that one higher lying singlet state  $S_m$  couples dominantly to the state  $T_1$ , i. e. to at least to one  $T_1$  triplet substate.  $E(S_m)$  and  $E(T_1)$  are the (unperturbed) energies of the (pure) singlet state  $S_m$  and the (pure) triplet state  $T_1$ , respectively.

A consideration of the energy denominator and its magnitude is particularly helpful. Presumably, SOC with the energetically most proximate singlet state of adequate character represents a leading contribution to the radiative rate. Therefore, eq. (18) is showing, for simplicity, only one mixing singlet state, being the state  $S_m$ , although, in general, several singlet states may contribute to the allowedness of the  $T_1 \rightarrow S_0$  transition and thus to the corresponding rate  $k^r(T_1 \rightarrow S_0)$ .

Eq. (18) contains also the dipole matrix element  $\langle S_0 | e\vec{r} | S_m \rangle$  with the dipole operator  $e\vec{r}$ . Accordingly, the radiative rate  $k^r$  of a transition from a triplet state  $T_1$  (or a triplet substate) to the singlet ground state depends on the allowedness (oscillator strength or

molar extinction coefficient) of the singlet-singlet transition  $S_0 \rightarrow S_n$ , whereby  $S_n$  is the singlet state that mixes with  $T_1$  via direct SOC.<sup>10</sup>

Quantum mechanical considerations show that SOC between a triplet state  $T_1$  and a singlet state  $S_1$  both stemming from the same orbital configuration vanishes. [2,4,5,57,183,184,187-192], but mixing with a higher lying state can be significant. This important message for Cu(I) complexes is illustrated by use of a simplified model. (Figure 31)

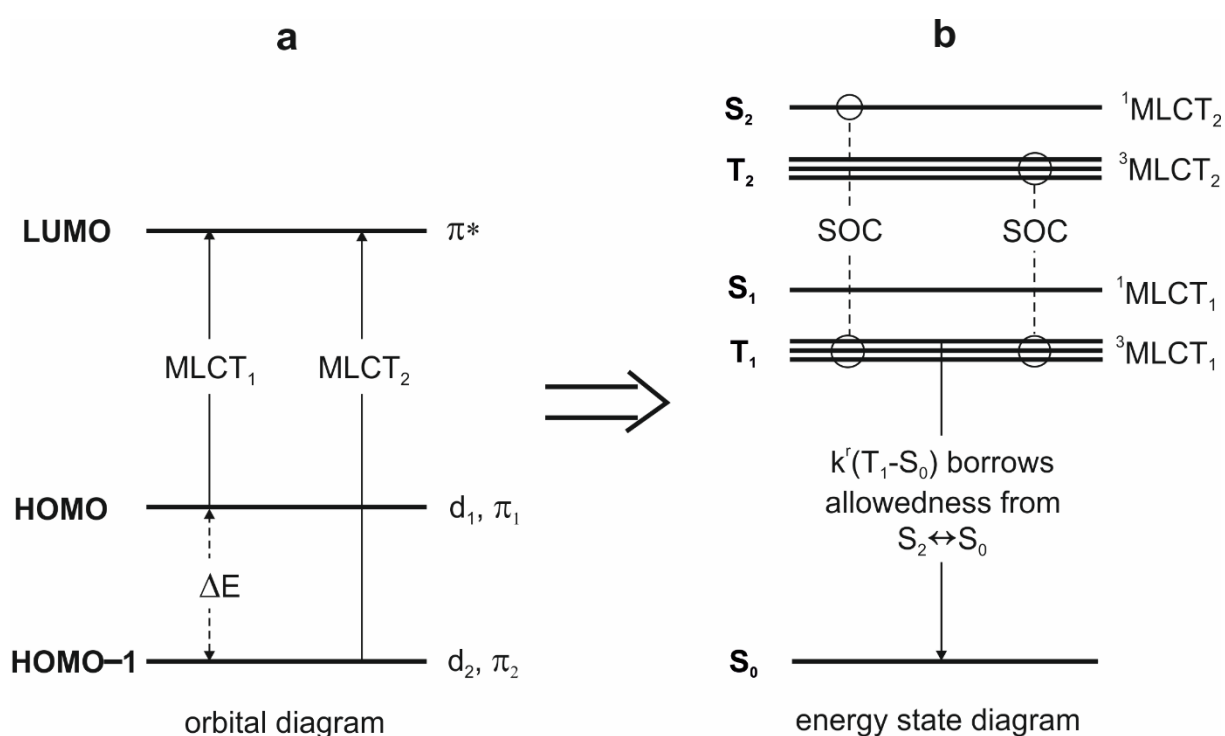


**Fig. 31** Frontier orbitals (a) and energy level diagram (b) for a simplified discussion. The dominating (direct) SOC routes that are important for the zero-field splitting and the radiative rate of the  $T_1$  state are shown schematically. Compare [2,4,183,184].

Figure 31a displays an orbital energy diagram for a model complex, showing only the frontier orbitals HOMO-1, HOMO, and LUMO. In particular, it is assumed that *different* Cu(I) 3d-orbitals, denoted as  $d_1$  and  $d_2$ , contribute to HOMO and HOMO-1,

<sup>10</sup> In this qualitative discussion, we do not describe details with respect to the individual coupling routes for each triplet substate, but see [2,4,183,184].

respectively.<sup>11</sup> The LUMO represents a ligand  $\pi^*$ -orbital. Corresponding MOs are easily generated by DFT calculations (compare Figures 3, 6, 9, 16, 22, and 25.).

In the scope of this model, two *different* MLCT transitions are possible. Each of them leads to one  $^1\text{MLCT}$  and one  $^3\text{MLCT}$  state. Accordingly, a four-state energy level diagram results, as shown in Figure 31b.

If we take into account that (i) SOC is dominantly induced by the metal d-orbitals (and not by  $\pi$ - or  $\pi^*$ -orbitals of the organic ligands), (ii) only one-center integrals on the metal contribute with large coupling constants, and (iii) a d-orbital cannot couple with itself, [2,4,5,57,183,184,187-192], we obtain relevant SOC paths. Accordingly, since SOC between the two lowest states resulting from the same orbital transition can be ignored, only two coupling routes are relevant for the  $T_1$  state, as marked in Figure 31b. In particular, SOC between the  $S_2$  ( $^1\text{MLCT}_2$ ) state and the  $T_1$  ( $^3\text{MLCT}_1$ ) state will induce allowedness to the  $T_1 \rightarrow S_0$  transition. As a consequence, a distinct phosphorescence decay path is opened in addition to the thermally activated path via  $S_1$  (TADF).

For example, for  $\text{Cu}_2\text{Cl}_2(\text{P}^*\text{N})_2$  **13**, this model seems to be adequate. HOMO-1 and HOMO contain contributions from different d-orbitals. The energy separation between these MOs amounts to only 0.378 eV, as determined by DFT calculations. (Table 6, below) This leads to a significant mixing of singlet character to the triplet state and thus, to a reduced overall emission decay time, as displayed in Figure 30.

For completeness, it is mentioned that the two SOC routes shown in Figure 31b govern also the zero-field splittings of the  $T_1$  state and the decay rates of the individual substates. [2,4,57,183,184] Obviously, for  $\text{Cu}_2\text{Cl}_2(\text{P}^*\text{N})_2$  **13** with  $\Delta E(\text{ZFS}) = 15 \text{ cm}^{-1}$ ,

---

<sup>11</sup> For most Cu(I) complexes, this approach is justified. If, however, HOMO-1 does not contain a corresponding d-orbital contribution, it has to be replaced by the next nearest occupied MO with the required d-orbital character.

these SOC routes are significant. However, details concerning the coupling paths between the triplet substates and higher lying states are not in the focus of the approach presented in this section. (For example, compare [57]).

In summary, the discussions show that SOC is responsible for different, though related effects. It induces the ZFS of and the radiative decay from the lowest triplet state  $T_1$  (or from the substates) to the electronic ground state  $S_0$ . A detailed discussion of this correlation is presented in Ref. [2,4,57,184].

We want to simplify the model further. To lowest order, the energy difference between singly excited states can be approximated by the energy difference of the corresponding orbitals. Thus, for a qualitative trend, it seems to be justified to replace the energy separation  $|E(T_1) - E(S_m)|$  between the  $T_1$  state and the SO-coupling  $S_m$  state<sup>12</sup> by the coarsely related energy separation  $\Delta E(\text{HOMO} - \text{HOMO}-n)$ . This model can easily be applied to a large number of Cu(I) compounds. In Figure 32, the experimentally determined phosphorescence decay rates  $k(T_1) = k'(T_1 \rightarrow S_0)$  are plotted versus the energy separation  $\Delta E(\text{HOMO} - \text{HOMO}-n)$ , resulting from simple DFT calculations. The data used for the plot of Figure 32 are summarized in Table 6. Interestingly, even in this very simplified approach, a fit of the experimental data displays a quadratic dependence – as expected from eq. (18) – according to

$$k'(T_1 \rightarrow S_0) = \text{const} [\Delta E(\text{HOMO} - \text{HOMO}-1)]^{-2} \quad (19)$$

$k'(T_1 \rightarrow S_0)$  is the experimental radiative triplet decay rate determined by use of the low-temperature decay time in the region of the plateau.

---

<sup>12</sup> For most Cu(I) complexes, the coupling singlet state is state  $S_2$ , but in some cases, it is a higher lying singlet state. For example, for compound **2**, the state  $S_6$  is responsible for mixing. However, this state results also from the HOMO-1 to LUMO transition. [67]



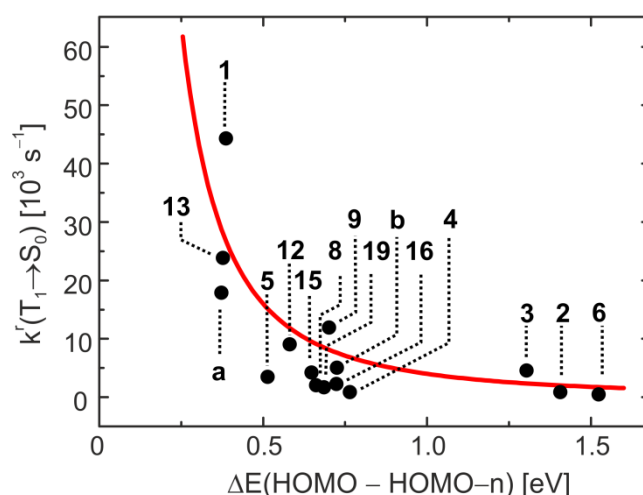


**Fig. 32** Phosphorescence rate  $k(T_1)$  plotted versus the energy separation between HOMO, containing a contribution of  $d_1$  character, and the next molecular orbital HOMO- $n$  with distinct metal- $d$  contribution, however, different from  $d_1$ . Usually  $n = 1$ . Numeric data are listed in Table 6. The red line represents a fit with an inverse quadratic dependence according to eq. (19).

**Table 6.** Energy differences  $\Delta E(\text{HOMO} - \text{HOMO}-n)$  between the highest occupied molecular orbital with metal  $d$  and the next nearest occupied molecular orbital with different  $d$ -orbital character compared to phosphorescence decay rates.

Compound <sup>a</sup>	$\Delta E(\text{HOMO} - \text{HOMO}-n)$ [eV] <sup>b</sup>	$n^c$	$\tau(T_1)$ [ $\mu\text{s}$ ] <sup>d</sup>	$k^r(T_1 \rightarrow S_0)$ [ $\text{s}^{-1}$ ] <sup>e</sup>	
$\text{Cu}_2\text{I}_2[\text{MePyrPHOS}](\text{Pph}_3)_2$	<b>1</b>	0.387	1	23	$43 \cdot 10^3$
$\text{Cu}_2\text{Cl}_2(\text{N}^{\wedge}\text{P})_2$	<b>13</b>	0.378	1	43	$23 \cdot 10^3$
$\text{Cu}_2\text{I}_2[\text{N}3^{\wedge}\text{P}]_3^f$	<b>a</b>	0.373	1	56	$18 \cdot 10^3$
$\text{Cu}(\text{tmbpy})(\text{POP})^+$	<b>9</b>	0.702	1	84	$5.6 \cdot 10^3$
$\text{Cu}_2\text{I}_2(\text{MePyrPHOS})(\text{dpph})$	<b>12</b>	0.582	1	109	$7.0 \cdot 10^3$
$\text{Cu}(\text{dmp})(\text{pop})^+^g$	<b>b</b>	0.726	1	200	$2.0 \cdot 10^3$
$[\text{Cu}(\mu\text{-Cl})(\text{PNMe}_2)]_2$	<b>3</b>	1.304	1	250	$4.0 \cdot 10^3$
$\text{Cu}(\text{dmp})(\text{phanephos})^+$	<b>15</b>	0.648	1	240	$2.9 \cdot 10^3$
$[\text{Cu}(\mu\text{-I})(\text{PNMe}_2)]_2$	<b>5</b>	0.514	3	290	$3.4 \cdot 10^3$
$\text{Cu}(\text{pop})(\text{pz}_4\text{B})$	<b>16</b>	0.724	1	450	$2.2 \cdot 10^3$
$\text{Cu}(\text{pop})(\text{pz}_2\text{BPh}_2)$	<b>8</b>	0.662	1	500	$2.0 \cdot 10^3$
$\text{Cu}(\text{pop})(\text{pz}_2\text{BH}_2)$	<b>19</b>	0.686	1	610	$1.6 \cdot 10^3$
$\text{Cu}(\text{dppb})(\text{pz}_2\text{BPh}_2)$	<b>2</b>	1.407	1	1200	$0.83 \cdot 10^3$
$[\text{Cu}(\mu\text{-Br})(\text{PNMe}_2)]_2$	<b>4</b>	0.765	1	1200	$0.8 \cdot 10^3$
$\text{Cu}_2(\text{dppb})_2\text{Cl}_2$	<b>6</b>	1.524	2	2200	$0.2 \cdot 10^3$

a. molecular formulas presented in Figure 2.

b. orbital energies were obtained from DFT calculations on molecules in the  $T_1$  optimized geometries at the B3LYP/def2-svp theory level. (Compare also [205,206])

c.  $n$  refers to the  $n$ -th occupied orbital (HOMO -  $n$ ) with a  $d$  character being different from that in the HOMO.

d. emission decay time in the plateau range. (Compare Figures 11 and 27).

e. radiative rate of the  $T_1 \rightarrow S_0$  transition calculated from  $\tau(T_1)$  and the emission quantum yield according to eq. (3).

f.  $Cu_2I_2[N_3^{\wedge}P]_3$  = tris(1-*n*-butyl-5-diphenylphosphino-1,2,4-triazole)-dicopperdiiodide. [63,208]

g compare Table 2.

It becomes obvious that at large energy separation, for example of  $\Delta E > 1.5$  eV, the triplet decay rate is very small, e.g. for compound **2** with  $k^r(T_1 \rightarrow S_0) = 0.83 \cdot 10^3 \text{ s}^{-1}$  [67]).

This shows that SOC with respect to the  $T_1$  state is very weak. With a decrease of  $\Delta E(\text{HOMO} - \text{HOMO}-n)$  to  $\approx 0.4$  eV, the phosphorescence rate increases drastically, for example, for compound **1** to  $k^r(T_1 \rightarrow S_0) = 4.8 \cdot 10^4 \text{ s}^{-1}$  [5]), representing an increase (relative to compound **2**) by a factor of almost 60.

Obviously, the presented very simple model, being based only on DFT calculations without the need of sophisticated extensions to SOC-TD-DFT theory, treating explicitly the spin-orbit coupling [209-213], may be helpful in designing new materials that show efficient phosphorescence in addition to TADF at ambient temperature. This is a promising approach to reduce the overall emission decay and thus, saturation effects of an electroluminescent device.

## 8. Concluding summary

In this contribution, we present a series of Cu(I) compounds that show a large diversity of photophysical properties. These do not only open access to important applications, especially, in the field of light generation in OLEDs, but also stimulate progress in scientific research due to the possibility of chemical tuning of electronic energy states with respect to their energy positions, separations, SOC routes, oscillator strength, etc.. This is particularly interesting regarding understanding and engineering of compounds with specific luminescence properties, such as emission colors, quantum yields, or decay times. Since the focus of this study lies on understanding and improving

processes of TADF materials, we present compounds that cover a wide range of TADF-related properties as displayed in Table 7.

It is obvious that the energy separation  $\Delta E(S_1-T_1)$  between the lowest excited singlet and triplet states governs the radiative TADF decay time  $\tau(\text{TADF})$ . For OLED applications, this decay should be as short as possible.  $\Delta E(S_1-T_1)$  is determined by the exchange interaction and accordingly by the spatial overlap of HOMO and LUMO as well as by their angular distributions. In the series discussed,  $\Delta E(S_1-T_1)$  varies from 270 to 1300  $\text{cm}^{-1}$  and indeed, the compounds with the smallest values exhibit the shortest  $\tau(\text{TADF})$  decay time. (Table 7) Interestingly, this holds even though the triplet decay time belongs to the largest values observed so far with  $\tau(T_1) = 1200 \mu\text{s}$  (compare compound **2**, section 4.1). On the other hand with decreasing  $\Delta E(S_1-T_1)$ , the decay time of the  $S_1$  fluorescence, from fitting of the  $\tau(T)$  data, increases and reaches a value of  $\tau(S_1) = 570 \text{ ns}$  for compound **1** with  $\Delta E(S_1-T_1) = 270 \text{ cm}^{-1}$ . Thus, and according to eq. (1), it may be possible that a lower limit for  $\tau(\text{TADF})$  might exist for “traditional” Cu(I) complexes. (Section 5) However, other mechanisms are suited to shorten the overall (radiative) decay time. In particular, “tuning-in” of an additional phosphorescence decay path is successful (section 6), since the triplet decay time  $\tau(T_1)$  can become as short as almost 20  $\mu\text{s}$  if SOC is efficient enough. (Table 7) A simple approach, how to understand the related SOC routes is presented in section 7. For completeness, it is remarked that also the properties of the singlet  $S_1$  state can be modified by inducing mixing with other higher lying singlet(s) by configuration interaction. These effects are not studied in this contribution, but it is indicated that the overall (radiative) decay time can efficiently be pushed down. Interestingly, values being similarly short as the triplet decay time reported for the attractive OLED emitter Ir(ppy)<sub>3</sub> [60] may be obtained.

The main trends discussed in this contribution refer to emission decay times, such as the triplet decay  $\tau(T_1)$ , the singlet decay  $\tau(S_1)$ , and the TADF decay  $\tau(\text{TADF})$  at ambient temperature. We also worked out trends how the compounds' chemical structures and their environments, in particular the rigidity, govern the emission quantum yields. Thus, values of  $\phi_{\text{PL}}$  of almost 100% are obtained even for ambient temperature. (Table 7).

In conclusion, the discussed properties and trends demonstrate the high potential of Cu(I) compounds in the field of luminescence behavior, TADF properties, and OLED applications.

**Table 7** Photophysical data for Cu(I) compounds (powders)

Compound		$\lambda_{\max}^a$	$\lambda_{\max}^a$	$\phi_{\text{PL}}^b$	$\phi_{\text{PL}}^b$	$\tau^c$	$\tau^c$	$\tau^d$	$\tau^e$	$\Delta(S_1-T_1)$ [cm <sup>-1</sup> ]	Ref.
		[nm]	[nm]	[%]	[%]	[ $\mu\text{s}$ ]	[ $\mu\text{s}$ ]	[ $\mu\text{s}$ ]	[ns]		
		300 K	77 K	300 K	77 K	300 K	77 K	T <sub>1</sub> →S <sub>0</sub>	S <sub>1</sub> →S <sub>0</sub>		
Cu <sub>2</sub> I <sub>2</sub> [MePyrPHOS)(Pph <sub>3</sub> ) <sub>2</sub>	<b>1</b>	511	520	97	≈100	5.0	20	23	570	270	[5]
Cu(dppb)(pz <sub>2</sub> Bph <sub>2</sub> )	<b>2</b>	535	535 <sup>f</sup>	70	≈100	3.3	300	1200	180	370	[67]
[Cu(μ-Cl)(PNMe <sub>2</sub> ) <sub>2</sub> ]	<b>3</b>	506	513	45	≈100	6.6	220	250	210	460	[73]
[Cu(μ-Br)(PNMe <sub>2</sub> ) <sub>2</sub> ]	<b>4</b>	490	498	65	≈100	4.1	930	1200	110	510	[73]
[Cu(μ-I)(PNMe <sub>2</sub> ) <sub>2</sub> ]	<b>5</b>	464	471	65	≈100	4.6	270	290	90	570	[73]
Cu <sub>2</sub> Cl <sub>2</sub> (dppb) <sub>2</sub>	<b>6</b>	545	545	35	52	3.0	2200	2200	70	600	[69]
[Cu(μ-I)(PNpy)] <sub>2</sub>	<b>7</b>	465	465	65	≈100	5.6	250	250	100	630	[73]
Cu(pop)(pz <sub>2</sub> Bph <sub>2</sub> )	<b>8</b>	464	474	90	≈100	13	500	500	170	650	[65]
Cu(tmbpy)(pop) <sup>+</sup>	<b>9</b>	555	575	55	47	11	87	84	160	720	[72]
(IPr)Cu(py <sub>2</sub> -BMe <sub>2</sub> )	<b>10</b>	475	490	76	91	11	34	34	160	740	[45]
[Cu(PNP <sup>t</sup> Bu)] <sub>2</sub> <sup>g</sup>	<b>11</b>	512	523	57	--	11	336	343	79	790	[38]
Cu <sub>2</sub> I <sub>2</sub> (MePyrPHOS)(dpph)	<b>12</b>	519	558	88	76	24	109	110	190	830	[5]
Cu <sub>2</sub> Cl <sub>2</sub> (N <sup>^</sup> P) <sub>2</sub>	<b>13</b>	485	510	92	97	8.3	44	42	40	930	[44]
CuCl(Pph <sub>3</sub> ) <sub>2</sub> (4-Mepy)	<b>14</b>	468	488	99	82	9.4 <sup>h</sup>	36 <sup>h</sup>	34	47	940	[74]
Cu(dmp)(phanephos) <sup>+</sup>	<b>15</b>	530	562	80	70	14	240	240	40	1000	[61, 67]
Cu(pop)(pz <sub>4</sub> B)	<b>16</b>	447	452	90	≈100	22	450	450	80	1000	[2, 65]
CuBr(Pph <sub>3</sub> ) <sub>2</sub> (4-Mepy)	<b>17</b>	467	477	95	95	15 <sup>h</sup>	52 <sup>h</sup>	50	41	1070	[74]
CuI(Pph <sub>3</sub> ) <sub>2</sub> (4-Mepy)	<b>18</b>	455	458	66	76	9.5 <sup>h</sup>	52 <sup>h</sup>	49	14	1170	[74]
Cu(pop)(pz <sub>2</sub> BH <sub>2</sub> )	<b>19</b>	436	456	45	≈100	20	610	610	10	1300	[4, 65]

a. Emission maximum,

b. Emission quantum yield measured with an integrating sphere (Hamamatsu C9920-02),

c. Overall emission decay time,

d. Emission decay time in the plateau range,

e. S<sub>1</sub> decay time (from a fit, compare section 4.1),

f. The emission at 77 K is dominated by TADF,

g. Measured in a vapor-deposited film containing the complex [Cu(PNP<sup>t</sup>Bu)]<sub>2</sub> **11** and 1,1-bis(4-(N,N-di-p-tolylamino)phenyl)cyclohexane (DAPC) host matrix. [38]

h. The emission decay behavior strongly deviated from a mono-exponential decay. The data were fitted by an averaging procedure.

## Appendix A

In this appendix, we discuss why the electric dipole transition moment  $\vec{\mu}(S_1-S_0)$  for an excited singlet state  $S_1$ , resulting from a HOMO-LUMO excitation, and the ground state  $S_0$  may be expressed by the electric dipole transition moment  $\mu_{H,L}$  between the orbitals HOMO  $\phi_H$  and LUMO  $\phi_L$  as given in eq. (8).

This is a consequence of the fact that the electric dipole operator for the electrons with charge  $q = -e$  is a one-particle operator given by

$$\vec{\mu} = \sum_i \vec{\mu}(i) = \sum_i q \vec{r}(i) \quad (\text{A.1})$$

where the summation is over all  $n$  electrons of the state under consideration and  $\vec{r}(i)$  is the position vector of the  $i$ -th electron. Note that  $\vec{\mu}$  is a spin-independent operator.

We assume for simplicity that we have a restricted spin basis such that for each spatial orbital  $x$ , there is a spin orbital with spatial orbital  $x$  and spin function  $\alpha$ , and a spin orbital for  $x$  with spin function  $\beta$ . We denote the spin orbital  $x\beta$  by  $\bar{x}$  and the spin orbital  $x\alpha$  for simplicity also by  $x$ , whenever it is clear from the context whether a spatial or a spin orbital is meant. Furthermore, we assume that the ground state singlet  $|\Psi\rangle = |S_0\rangle$  is a closed shell determinant such that each occupied spatial orbital carries an  $\alpha$  and a  $\beta$  spin, i.e.  $|S_0\rangle = |a\bar{a}b\bar{b}\dots\rangle$ . Occupied orbitals are denoted by  $a, b, \dots$  and unoccupied orbitals<sup>13</sup> by  $r, s, \dots$ . Spatial orbitals are assumed to be orthonormal.

Since a singly excited singlet state  $|S(a \rightarrow r)\rangle = |{}^1\Psi_a^r\rangle$  for spatial orbitals  $a$  and  $r$ , is a linear combination ([143], p. 103)

$$|{}^1\Psi_a^r\rangle = (|\Psi_{\bar{a}}^r\rangle + |\Psi_a^r\rangle)/\sqrt{2} \quad (\text{A.2})$$

---

<sup>13</sup> Unoccupied orbitals are often also called virtual orbitals.

where on the right hand side  $\Psi_{\bar{a}}^{\bar{r}}$  is the determinant where the spin orbital  $\bar{a}$  is replaced by  $\bar{r}$  in  $\Psi$ . Using ([143], p. 97)

$$\langle \Psi_b^s | Q | \Psi \rangle = \langle s | q | b \rangle \quad (\text{A.3})$$

for any spin orbitals  $b$  and  $s$  and any one-particle operator  $Q = \sum_i q(i)$ , we obtain

$$|\langle S_1(\varphi_H \rightarrow \varphi_L) | \bar{\mu} | S_0 \rangle|^2 = 2 |\bar{\mu}_{H,L}|^2 = 2 |\langle \varphi_L | \bar{\mu} | \varphi_H \rangle|^2 \quad (\text{A.4})$$

since  $\langle \bar{r} | \bar{r} | \bar{a} \rangle = \langle r | \bar{r} | a \rangle$  due to spin-independence of  $\bar{\mu}$ .

### Acknowledgments

We acknowledge funding of our research by the Germany Ministry of Education and Research (BMBF) in the scope of the NEMO (FKN 13N10619) as well as the cyCESH (FKN 13N12668) project and the European Union's Horizon 2020 research and innovation programme under the Marie Skłodowska-Curie grant agreement No. 645628. Furthermore, we thank our cooperation partners and friends for fruitful collaborations. This includes the research groups around Prof. Dr. Mark E. Thompson and Prof. Dr. Peter I. Djurovich (University of Southern California, Los Angeles, USA), Prof. Dr. Neil Robertson (University of Edinburgh, Edinburgh, United Kingdom), Prof. Dr. Lars Wesemann and Prof. Dr. Hermann Mayer (University of Tübingen, Tübingen, Germany), Prof. Dr. Chensheng Ma (Shenzhen University, China), Prof. Dr. Wai-Ming Kwok (The Hong Kong Polytechnic University, Hong kong), and Prof. Dr. Uwe Monkowius (Johannes Kepler University Linz, Austria) In addition, we thank the German Academic Exchange Service (DAAD) and the Bavaria California Technology Center (BaCaTec) for giving us the opportunity to establish and maintain these collaborations.

### References:

- 
- [1] H. Yersin (Ed.), *Highly Efficient OLEDs with Phosphorescent Materials*, Wiley-VCH, Weinheim, 2008.
- [2] H. Yersin, A. F. Rausch, R. Czerwieniec, in *Physics of Organic Semiconductors*, W. Brütting, C. Adachi (Eds.); Wiley-VCH: Weinheim, Germany, 2012; p 371.
- [3] W. Brütting, C. Adachi, C. (Eds.), *Physics of Organic Semiconductors*, Wiley-VCH: Weinheim, Germany, 2012.
- [4] H. Yersin, A. F. Rausch, R. Czerwieniec, T. Hofbeck, T. Fischer, *Coord. Chem. Rev.* 255 (2011) 2622.
- [5] M. J. Leitl, D. M. Zink, A. Schinabeck, T. Baumann, D. Volz, H. Yersin, *Top. Curr. Chem.* 374 (2016) DOI: 10.1007/s41061-016-0019-1.
- [6] F. Dumur, *Org. Electron.* 21 (2015) 27.
- [7] S. Keller, A. Pertegás, G. Longo, L. Martínez, J. Cerdá, J. M. Junquera-Hernández, A. Prescimone, E. C. Constable, C. E. Housecroft, E. Ortí, H. J. Bolink, *J. Mater. Chem. C* 4 (2016) 3857.
- [8] R. D. Costa, D. Tordera, E. Ortí, H. J. Bolink, J. Schönle, S. Graber, C. E. Housecroft, E. C. Constable, J. A. Zampese, *J. Mater. Chem.* 21 (2011) 16108.
- [9] H. J. Bolink, E. Coronado, R. D. Costa, E. Ortí, M. Sessolo, S. Graber, K. Doyle, M. Neuburger, C. E. Housecroft, E. C. Constable, *Adv. Mater.* 20 (2008) 3910.
- [10] N. Armaroli, G. Accorsi, M. Holler, O. Moudam, J.-F. Nierengarten, Z. Zhou, R. T. Weigh, R. Welter, *Adv. Mater.* 18 (2006) 1313.
- [11] Q. S. Zhang, Q. G. Zhou, Y. X. Cheng, L. X. Wang, D. G. Ma, X. B. Jing, F. Wang, *Adv. Funct. Mater.* 16 (2006) 1203.
- [12] C. Bizzarri, C. Strabler, J. Prock, B. Trettenbrein, M. Ruggenthaler, C.-H. Yang, F. Polo, A. Iordache, P. Brügge, L. De Cola, *Inorg. Chem.* 53 (2014) 10944.
- [13] S. Medina-Rodríguez, F. J. Orriach-Fernández, C. Poole, P. Kumar, A. de la Torre-Vega, J. F. Fernández-Sánchez, E. Baranoff, A. Fernández-Gutiérrez, *Chem. Commun.* 51 (2015) 11401.
- [14] C. S. Smith, C. W. Branham, B. J. Marquardt, K. R. Mann, *J. Am. Chem. Soc.* 132 (2010) 14079.
- [15] C. S. Smith, K. R. Mann, *J. Am. Chem. Soc.* 134 (2012) 8786.
- [16] R. Czerwieniec, M. J. Leitl, H. Yersin, *Patents DE 102012101067 A1* (2013), *WO 2013117460 A2* (2013).
- [17] R. Czerwieniec, M. J. Leitl, T. Hofbeck, H. Yersin, *manuscript in preparation*
- [18] A. M. Prokhorov, T. Hofbeck, R. Czerwieniec, A. F. Suleymanova, D. N. Kozhevnikov, H. Yersin, *J. Am. Chem. Soc.* 136 (2014) 9637.
- [19] T. Hofbeck, Y. C. Lam, M. Kalbáč, S. Zálíš, A. Vlček Jr., H. Yersin, *Inorg. Chem.* 55 (2016) 2441.
- [20] M. Knorn, T. Rawner, R. Czerwieniec, O. Reiser, *ACS Catal.* 5 (2015) 5186.
- [21] X.-J. Tang, W. R. Dolbier, *Angew. Chem., Int. Ed.* 54 (2015) 4246.
- [22] D. B. Bagal, G. Kachkovskiy, M. Knorn, T. Rawner, B. M. Bhanage, O. Reiser, *Angew. Chem., Int. Ed.* 54 (2015) 6999.
- [23] B. Wang, D. P. Shelar, X.-Z. Han, T.-T. Li, X. Guan, W. Lu, K. Liu, Y. Chen, W.-F. Fu, C.-M. Che, *Chem. Eur. J.* 21 (2015) 1184.
- [24] Q. Yang, F. Dumur, F. Morlet-Savary, *J. Poly. J. Lalevée, Macromolecules* 48 (2015) 1972.
- [25] A. Baralle, L. Fensterbank, J.-P. Goddard, C. Ollivier, *Chem. Eur. J.* 19 (2013) 10809.
- [26] S.-P. Luo, E. Meja, A. Friedrich, A. Pazidis, H. Junge, A.E. Surkus, R. Jackstell, S. Denurra, S. Gladiali, S. Lochbrunner, M. Beller, *Angew. Chem. Int. Ed.* 52 (2013) 419.
- [27] Q. Zhang, Q. Zhou, Y. Cheng, L. Wang, D. Ma, X. Jing, F. Wang, *Adv. Mater.* 16 (2004) 432.



- 
- [28] D. M. Zink, D. Volz, T. Baumann, M. Mydlak, H. Flügge, J. Friedrichs, M. Nieger, S. Bräse, *Chem. Mater.* 25 (2013) 4471.
- [29] D. Volz, D. M. Zink, T. Bocksrocker, J. Friedrichs, M. Nieger, T. Baumann, U. Lemmer, S. Bräse, *Chem. Mater.* 25 (2013) 3414.
- [30] D. Volz, T. Baumann, H. Flügge, M. Mydlak, T. Grab, M. Bächle, C. Barner-Kowollik, S. Bräse, *J. Mater. Chem.*, 22 (2012) 20786.
- [31] M. Wallesch, D. Volz, D. M. Zink, U. Schepers, M. Nieger, T. Baumann, S. Bräse, *Chem. Eur. J.* 20 (2014) 6578.
- [32] D. Volz, Y. Chen, M. Wallesch, R. Liu, C. Fléchon, D. M. Zink, J. Friedrichs, H. Flügge, R. Steininger, J. Göttlicher, C. Heske, L. Weinhardt, S. Bräse, F. So, T. Baumann, *Adv. Mater.* 27 (2015) 2538.
- [33] M. Osawa, M. Hoshino, M. Hashimoto, I. Kawata, S. Igawa, M. Yashima, *Dalton Trans.* 44 (2015) 8369.
- [34] S. Igawa, M. Hashimoto, I. Kawata, M. Yashima, M. Hoshino, M. Osawa, *J. Mater. Chem. C* 1 (2013) 542.
- [35] M. Hashimoto, S. Igawa, M. Yashima, I. Kawata, M. Hoshino, M. Osawa, *J. Am. Chem. Soc.* 133 (2011) 10348.
- [36] Z. Liu, J. Qiu, F. Wei, J. Wang, X. Liu, M. G. Helander, S. Rodney, Z. Wang, Z. Bian, Z. Lu, M. E. Thompson, C. Huang, *Chem. Mater.* 26 (2014) 2368.
- [37] F. Wei, J. Qiu, X. Liu, J. Wang, H. Wei, Z. Wang, Z. Liu, Z. Bian, Z. Lu, Y. Zhao, C. Huang, *J. Mater. Chem. C* 2 (2014) 6333.
- [38] J. C. Deaton, S. C. Switalski, D. Y. Kondakov, R. H. Young, T. D. Pawlik, D. J. Giesen, S. B. Harkins, A. J. M. Miller, S. F. Mickenberg, J. C. Peters, *J. Am. Chem. Soc.* 132 (2010) 9499.
- [39] Q. Zhang, T. Komino, H. Shuping, S. Matsunami, K. Goushi, C. Adachi, *Adv. Funct. Mater.* 22 (2012) 2327.
- [40] G. Cheng, G. K.-M. So, W.-P. To, Y. Chen, C.-C. Kwok, C. Ma, X. Guan, X. Chang, W.-M. Kwok, C.-M. Che, *Chem. Sci.* 6 (2015) 4623.
- [41] a) H. Yersin, R. Czerwieniec, U. Monkowius, Patent DE 102010031831 A1 (2010).  
b) H. Yersin, R. Czerwieniec, U. Monkowius, Patent WO 2012010650 A1 (2011).
- [42] Q. Zhang, X.-L. Chen, J. Chen, X.-Y. Wu, R. Yu, C.-Z. Lu, *RSC Adv.* 5 (2015) 34424.
- [43] X.-L. Chen, R. Yu, Q.-K. Zhang, L.-J. Zhou, X.-Y. Wu, Q. Zhang, C.-Z. Lu, *Chem. Mater.* 25 (2013) 3910.
- [44] T. Hofbeck, U. Monkowius, H. Yersin, *J. Am. Chem. Soc.* 137 (2015) 399.
- [45] M. J. Leitl, V. A. Krylova, P. I. Djurovich, M. E. Thompson, H. Yersin, *J. Am. Chem. Soc.* 136 (2014) 16032.
- [46] M. A. Baldo, D. F. O'Brien, Y. You, A. Shoustikov, S. Sibley, M. E. Thompson, S. R. Forrest, *Nature* 395 (1998) 151.
- [47] M. A. Baldo, S. Lamansky, P. E. Burrows, M. E. Thompson, S. R. Forrest, *Appl. Phys. Lett.* 75 (1999) 4.
- [48] Y. Kawamura, K. Goushi, J. Brooks, J. J. Brown, H. Sasabe, C. Adachi, *Appl. Phys. Lett.* 86 (2005) 071104.
- [49] H. Sasabe, J. Takamatsu, T. Motoyama, S. Watanabe, G. Wagenblast, N. Langer, O. Molt, E. Fuchs, C. Lennartz, J. Kido, *Adv. Mater.* 22 (2010) 50030.
- [50] K. Li, G. S. M. Tong, Q. Wan, G. Cheng, W.-Y. Tong, W.-H. Ang, W.-L. Kwong, C.-M. Che, *Chem. Sci.* 7 (2016) 1653.
- [51] G. Cheng, S. C. F. Kui, W.-H. Ang, M.-Y. Ko, P.-K. Chow, C.-L. Kwong, C.-C. Kwok, C. Ma, X. Guan, K.-H. Low, S.-J. Suc, C.-M. Che, *Chem. Sci.* 5 (2014) 4819.
- [52] L. F. Gildea and J. A. G. Williams, Iridium and platinum complexes for OLEDs, in *Organic light-emitting diodes: materials, devices and applications*, ed. A. Buckley, Woodhead Publishing, Cambridge, 2013, pp 77-113.

- 
- [53] C. Adachi, M. A. Baldo, M. E. Thompson, S. R. Forrest, *J. Appl. Phys.* 90 (2001) 5048.
- [54] J. C. Deaton, F. N. Castellano, in: E. Zysman-Colman (ed) *Iridium(III) in optoelectronic and photonics applications*. Wiley VCH, Weinheim, Germany (in press)
- [55] H. Yersin, *Top. Curr. Chem.* 241 (2004) 1.
- [56] E. Zysman-Colman (ed) *Iridium(III) in optoelectronic and photonics applications*. Wiley VCH, Weinheim, Germany (in press).
- [57] A. F Rausch, H. H. H. Homeier, H. Yersin, *Top. Organomet. Chem.* 29 (2010) 193.
- [58] G. J. Hedley, A. Ruseckas, I. D.W. Samuel, *Chem. Phys. Lett.* 450 (2008) 292.
- [59] H. Yersin, D. Donges, *Top. Curr. Chem.* 214 (2001) 81
- [60] T. Hofbeck, H. Yersin, *Inorg. Chem.* 49 (2010), 9290.
- [61] R. Czerwieńiec, K. Kowalski, H. Yersin, *Dalton Trans.* 42 (2013) 4623.
- [62] D. Volz, M. Wallesch, C. Fléchon, M. Danz, A. Verma, J. M. Navarro, D. M. Zink, S. Bräse, T. Baumann, *Green Chem.* 17 (2015) 1988.
- [63] D. M. Zink, M. Bächle, T. Baumann, M. Nieger, M. Kühn, C. Wang, W. Klopfer, U. Monkowius, T. Hofbeck, H. Yersin, S. Bräse, *Inorg. Chem.* 52 (2013) 2292.
- [64] D. M. Zink, T. Baumann, J. Friedrichs, M. Nieger, S. Bräse, *Inorg. Chem.* 52 (2013) 13509.
- [65] a) R. Czerwieńiec, J. Yu, H. Yersin, *Inorg. Chem.* 50 (2011) 8293.  
b) R. Czerwieńiec, J. Yu, H. Yersin, *Inorg. Chem.* 51 (2012) 1975.
- [66] V. A. Krylova, P. I. Djurovich, B. L. Conley, R. Haiges, M. T. Whited, T. J. Williams, M. E. Thompson, *Chem. Commun.* 50 (2014) 7176.
- [67] R. Czerwieńiec, H. Yersin, *Inorg. Chem.* 54 (2015) 4322.
- [68] H. Yersin, R. Czerwieńiec, A. Hupfer, *Proc. SPIE* 8435 (2012) 843508.
- [69] H. Yersin, M. J. Leidl, R. Czerwieńiec, *Proc. SPIE* 9183 (2014) 91830N.
- [70] T. Gneuss, M. J. Leidl, L. H. Finger, H. Yersin, J. Sundermeyer, *Dalton Trans.* 44 (2015) 20045.
- [71] T. Gneuss, M. J. Leidl, L. H. Finger, N. Rau, H. Yersin, J. Sundermeyer, *Dalton Trans.* 44 (2015) 8506.
- [72] C. L. Linfoot, M. J. Leidl, P. Richardson, A. F. Rausch, O. Chepelin, F. J. White, H. Yersin, N. Robertson, *Inorg. Chem.* 53 (2014) 10854.
- [73] M. J. Leidl, F. R. Kühle, H. A. Mayer, L. Wesemann, H. Yersin, *J. Phys. Chem. A* 117 (2013) 11823.
- [74] H. Ohara, A. Kobayashia, M. Kato, *Dalton Trans.* 43 (2014) 17317.
- [75] D. Volz, A. F. Hirschbiel, D. M. Zink, J. Friedrichs, M. Nieger, T. Baumann, S. Bräse, C. Barner-Kowollik, *J. Mater. Chem. C* 2 (2014) 1457.
- [76] X.-L. Chen, R. Yu, X.-Y. Wu, D. Liang, J.-H. Jia, C.-Z. Lu, *Chem. Commun.* (2016) DOI: 10.1039/c6cc00809g.
- [77] L. Kang, J. Chen, T. Teng, X.-L. Chen, R. Yu, C.-Z. Lu, *Dalton Trans.* 44 (2015) 11649
- [78] A. Tsuboyama, K. Kuge, M. Furugori, S. Okada, M. Hoshino, K. Ueno, *Inorg. Chem.* 46 (2007) 1992.
- [79] A. Tsuboyama, H. Iwawaki, M. Furugori, T. Mukaide, J. Kamatani, S. Igawa, T. Moriyama, S. Miura, T. Takiguchi, S. Okada, M. Hoshino, K. Ueno, *J. Am. Chem. Soc.* 125 (2003) 27 12971.
- [80] M. Osawa, *Chem. Commun.* 50 (2014) 1801.
- [81] L. Bergmann, G. J. Hedley, T. Baumann, S. Bräse, I. D. W. Samuel, *Sci. Adv.* (2016) doi: 10.1126/sciadv.1500889.
- [82] D. M. Zink, D. Volz, L. Bergmann, M. Nieger, S. Bräse, H. Yersin, T. Baumann, *Proc. SPIE* 8829 (2013) 882907-1.
- [83] H. Yersin, U. Monkowius T. Fischer, T. Hofbeck, Patent DE 10 2009 030 475 A1 (2009).

- 
- [84] H. Yersin, U. Monkowius, T. Fischer, T. Hofbeck, T. Baumann, T. Grab, Patent EP 2 408 787 B1 (2015).
- [85] A. Kobayashi, K. Komatsu, H. Ohara, W. Kamada, Y. Chishina, K. Tsuge, H.-C. Chang, M. Kato, *Inorg. Chem.* 52 (2013) 13188.
- [86] S. Shibata, K. Tsuge, Y. Sasaki, S. Ishizaka, N. Kitamura, *Inorg. Chem.* 54 (2015) 9733.
- [87] D. M. Zink, L. Bergmann, D. Ambrosek, M. Wallesch, D. Volz, M. Mydlak, *Transl. Mater. Res.* 1 (2014) 015003.
- [88] D. Volz, M. Nieger, J. Friedrichs, T. Baumann, S. Bräse, *Inorg. Chem. Commun.* 37 (2013) 106.
- [89] H. Xia, L. He, M. Zhang, M. Zeng, X. Wang, D. Lu, Y. Ma, *Optical Mater.* 29 (2007) 667.
- [90] V. A. Krylova, P. I. Djurovich, J. W. Aronson, R. Haiges, M. T. Whited, M. E. Thompson, *Organomet.* 31 (2012) 7983.
- [91] V. A. Krylova, P. I. Djurovich, M. T. Whited, M. E. Thompson, *Chem. Commun.* 46 (2010) 6696.
- [92] L. Bergmann, D. M. Zink, S. Bräse, T. Baumann, D. Volz, *Top. Curr. Chem.* 374 (2016) DOI 10.1007/s41061-016-0022-6.
- [93] T. Nishimoto, T. Yasuda, S. Y. Lee, R. Kondo, C. Adachi, *Mater. Horiz.* 1 (2014) 264.
- [94] Q. Zhang, J. Li, K. Shizu, S. Huang, S. Hirata, H. Miyazaki, C. Adachi, *J. Am. Chem. Soc.* 134 (2012) 14706.
- [95] H. Uoyama, K. Goushi, K. Shizu, H. Nomura, C. Adachi, *Nature* 492 (2012) 234.
- [96] H. Ohkuma, T. Nakagawa, K. Shizu, T. Yasuda, C. Adachi, *Chem. Lett.* 43 (2014) 1017.
- [97] K. Goushi, K. Yoshida, K. Sato, C. Adachi, *Nature Photonics* 6 (2012) 253.
- [98] Q. Zhang, D. Tsang, H. Kuwabara, Y. Hatae, B. Li, T. Takahashi, S. Y. Lee, T. Yasuda, C. Adachi, *Adv. Mater.* 27 (2015) 2096.
- [99] P. Rajamalli, N. Senthilkumar, P. Gandeepan, P.-Y. Huang, M.-J. Huang, C.-Z. Ren-Wu, C.-Y. Yang, M.-J. Chiu, L.-K. Chu, H.-W. Lin, C.-H. Cheng, *J. Am. Chem. Soc.* 138 (2016) 628.
- [100] S. Y. Lee, C. Adachi, T. Yasuda, *Adv. Mater.* 28 (2016) 4626.
- [101] S. Y. Lee, T. Yasuda, H. Komiyama, J. Lee, C. Adachi, *Adv. Mater.* 28 (2016) 4019.
- [102] E. Zysman-Colman, S. S. Ghosh, G. Xie, S. Varghese, M. Chowdhury, N. Sharma, D. B. Cordes, A. M. Z. Slawin, I. D. W. Samuel, *ACS Appl. Mater. Interfaces* 8 (2016) 9247.
- [103] M. Y. Wong, G. J. Hedley, G. Xie, L. S. Kölln, I. D. W. Samuel, A. Pertegás, H. J. Bolink, E. Zysman-Colman, *Chem. Mater.* 27 (2015) 6535.
- [104] J. S. Ward, R. S. Nobuyasu, A. S. Batsanov, P. Data, A. P. Monkman, F. B. Dias, M. R. Bryce, *Chem. Commun.*, 2016, 52, 2612
- [105] P. L. Santos, J. S. Ward, P. Data, A. S. Batsanov, M. R. Bryce, F. B. Dias, A. P. Monkman, *J. Mater. Chem. C*, 2016, 4, 3815
- [106] P. Data, P. Pander, M. Okazaki, Y. Takeda, S. Minakata, A. P. Monkman, *Angew. Chem. Int. Ed.* 2016, 55, 5739
- [107] K. Kotwica, P. Bujak, P. Data, W. Krzywiec, D. Wamil, P. A. Gunka, L. Skorcka, T. Jaroch, R. Nowakowski, A. Pron, A. Monkman, *Chem. Eur. J.* 22 (2016) 1.
- [108] S. L. Murov, J. Carmichael, G. L. Hug, *Handbook of Photochemistry*, Marcel Dekker, New York, 2nd edn, 1993, p. 340.
- [109] D. Felder, J.-F. Nierengarten, F. Barigelletti, B. Ventura, N. Armaroli, *J. Am. Chem. Soc.* 123 (2001) 6291.
- [110] P. Breddels, P. A. M. Berdowski, G. Blasse, D. R. J. McMillin, *Chem. Soc., Faraday Trans.* 2 78 (1982) 595.
- [111] A. Tsuboyama, K. Kuge, M. Furugori, S. Okada, M. Hoshino, K. Ueno, *Inorg. Chem.* 46 (2007) 1992.
- [112] S. Reineke, K. Walzer, K. Leo, *Phys. Rev. B* 75 (2007) 125328.

- 
- [113] N. Lin, J. Qiao, L. Duan, L. Wang, Y. Qiu, *J. Phys. Chem. C* 118 (2014) 7569.
- [114] S. Schmidbauer, A. Hohenleutner, B. König, *Adv. Mater.* 25 (2013) 2114.
- [115] I. Rabelo de Moraes, S. Scholz, B. Lüssem, K. Leo, *Organic Electronics* 12 (2011) 341
- [116] D. R. McMillin, K. M. McNet, *Chem. Rev.* 98 (1998) 1201.
- [117] M. W. Mara, K. A. Fransted, L. X. Chen, *Coord. Chem. Rev.* 282-283 (2015) 2.
- [118] L. X. Chen, G. Jennings, T. Liu, D. J. Gosztola, J. P. Hessler, D. V. Scaltrito, G. J. Meyer, *J. Am. Chem. Soc.* 124 (2002) 10861.
- [119] L. X. Chen, G. B. Shaw, I. Novozhilova, T. Liu, G. Jennings, K. Attenkofer, G. J. Meyer, P. Coppens, *J. Am. Chem. Soc.* 125 (2003) 7022.
- [120] M. Iwamura, H. Watanabe, K. Ishii, S. Takeuchi, T. Tahara, *J. Am. Chem. Soc.* 133 (2011) 7728.
- [121] N. Armadori, G. Accorsi, F. Cardinali, A. Listorti, *Top. Curr. Chem.* 280 (2007) 69.
- [122] A. Lavie-Cambot, M. Cantuel, Y. Leydet, G. Jonusauskas, D. M. Bassani, N. D. McClenaghan, *Coord. Chem. Rev.* 252 (2008) 2572.
- [123] M. Iwamura, S. Takeuchi, T. Tahara, *Acc. Chem. Res.* 48 (2015) 782
- [124] S. Garakyaraghi, E. O. Danilov, C. E. McCusker, F. N. Castellano, *J. Phys. Chem. A* 119 (2015) 3181.
- [125] Z. A. Siddique, Y. Yamamoto, T. Ohno, K. Nozaki, *Inorg. Chem.* 42 (2003) 6366.
- [126] N. J. Turro, V. Ramamurthy and J. C. Scaiano, *Modern Molecular Photochemistry of Organic Molecules*, University Science Books, Sausalito, 2010, p. 130.
- [127] W. Siebrand, *J. Chem. Phys.* 46 (1967) 440.
- [128] G. W. Robinson, R. P. Frosch, *J. Chem. Phys.* 38 (1963) 1187.
- [129] C. A. Parker, C. G. Hatchard, *Trans. Faraday Soc.* 57 (1961) 1894.
- [130] C. A. Parker, C. G. Hatchard, *J. Phys. Chem.* 66 (1962) 2506.
- [131] J. P. Heritage, A. Penzkofer, *Chem. Phys. Lett.* 44 (1976) 76.
- [132] E. P. Ippen, C. V. Shank, R. L. Woerner, *Chem. Phys. Lett.* 46 (1977) 20.
- [133] C. Ma, W.-M. Kwok, R. Czerwiec, H. Yersin, *manuscript in preparation*
- [134] W. Helfrich, W. G. Schneider, *J. Chem. Phys.* 44 (1966) 2902.
- [135] a) H. Yersin, U. Monkowius; German patent DE 10 2008 033563 (2008); European patent EP 2297276B1.  
b) H. Yersin, internal filing, University of Regensburg (2006).
- [136] K. Masui, H. Nakanotani, C. Adachi, *Org. Electron.* 14 (2013), 2721.
- [137] M. Inoue, T. Serevičius, H. Nakanotani, K. Yoshida, T. Matsushima, S. Juršėnas, C. Adachi, *Chem. Phys. Lett.* 644 (2016), 62.
- [138] R. Coehoorn, H. van Eersel, P. A. Bobbert, R. A. J. Janssen, *Adv. Funct. Mater.* 25 (2015) 2024.
- [139] R. W. Harrigan, G. A. Crosby, *J. Chem. Phys.* 59 (1973) 3468.
- [140] G. D. Hager, G.A. Crosby, *J. Am. Chem. Soc.* 97 (1975) 7031.
- [141] T. Azumi, C.M. O'Donnell, S.P. McGlynn, *J. Chem. Phys.* 45 (1966) 2735.
- [142] P. W. Atkins, *Quanta. A Handbook of Concepts*, 2nd ed.; Oxford University Press: Oxford, U.K., 1991.
- [143] A. Szabo, N. S. Ostlund. *Modern quantum chemistry*. McGraw-Hill, New York, 1989-
- [144] R. Czerwiec, A. M. El-Naggar, A. A. Albassam, I. V. Kityk, M. Graf, H. Yersin, *J Mater Sci: Mater Electron.* 26 (2015) 8394.
- [145] a) H. Yersin, U. Monkowius, T. Hofbeck, Patent DE 102011080240 A1 (2013). b) H. Yersin, U. Monkowius, T. Hofbeck, Patent WO 2013017675 A1 (2013).
- [146] a) R. Czerwiec, H. Yersin, Patent DE 102013100181 (2013). b) R. Czerwiec, H. Yersin, WO 2014108430 (2014).
- [147] H. Yersin, U. Monkowius, R. Czerwiec, J. Yu, Patent DE 102008048336 A1 (2008).  
b) H. Yersin, U. Monkowius, R. Czerwiec, J. Yu, Patent WO 2010031485 A1 (2009).

- 
- [148] G. Capano, M. Chergui, U. Rothlisberger, I. Tavernelli, T. J. Penfold, *J. Phys. Chem. A* 118 (2014) 9861.
- [149] C. E. McCusker, F. N. Castellano, *Inorg. Chem.* 52 (2013) 8114.
- [150] A. D. Becke, *J. Chem. Phys.* 98 (1993) 5648.
- [151] F. Weigend, R. Ahlrichs, *Phys. Chem. Chem. Phys.* 7 (2005) 3297.
- [152] S.-M. Kuang, D. G. Cuttell, D. R. McMillin, P. E. Fanwick, R. A. Walton, *Inorg. Chem.* 41 (2002) 3313.
- [153] D. G. Cuttell, S.-M. Kuang, P. E. Fanwick, D. R. McMillin, R. A. Walton, *J. Am. Chem. Soc.* 124 (2002) 6.
- [154] P. C. J. Kamer, P. W. N. M. van Leeuwen, J. N. H. Reek, *Acc. Chem. Res.* 34 (2001) 895.
- [155] L. Zhang, B. Li, Z. Su, *Langmuir* 25 (2009) 2068.
- [156] A. Kaeser, M. Mohankumar, J. Mohanraj, F. Monti, M. Holler, J.-J. Cid, O. Moudam, I. Nierengarten, L. Karmazin-Brelot, C. Duhayon, B. Delavaux-Nicot, N. Armaroli, J.-F. Nierengarten, *Inorg. Chem.* 52 (2013) 12140.
- [157] L.-Y. Zou, Y.-X. Cheng, Y. Li, H. Li, H.-X. Zhang, A.-M. Ren, *Dalton Trans.* 43 (2014) 11252.
- [158] I. Andrés-Tomé, J. Fyson, F. Baiao Dias, A. P. Monkman, G. Iacobellis, P. Coppo, *Dalton Trans.* 41 (2012) 8669.
- [159] C. L. Linfoot, P. Richardson, T. E. Hewat, O. Moudam, M. M. Forde, A. Collins, F. White, N. Robertson, *Dalton Trans.* 39 (2010) 8945.
- [160] G. Capano, U. Rothlisberger, I. Tavernelli, T. J. Penfold, *J. Phys. Chem. A* 119 (2015) 7026.
- [161] T. J. Penfold, S. Karlsson, G. Capano, F. A. Lima, J. Rittmann, M. Reinhard, M. H. Rittmann-Frank, O. Braem, E. Baranoff, R. Abela, I. Tavernelli, U. Rothlisberger, C. J. Milne, M. Chergui, *J. Phys. Chem. A*, 117 (2013) 4591.
- [162] U. Rössler, H. Yersin, *Phys. Rev. B* 26 (1982) 3187.
- [163] G. Gliemann, H. Yersin, *Struct. Bond.* 62 (1985) 87.
- [164] a) H. Yersin, R. Czerwieniec, U. Monkowius, J. Yu, German patent DE 102008048336 A1 (2010). b) H. Yersin, R. Czerwieniec, U. Monkowius, J. Yu, international patent WO 2010031485 A1 (2010).
- [165] M. Iwamura, S. Takeuchi, T. Tahara, *Phys. Chem. Chem. Phys.* 16 (2014) 4143.
- [166] P. A. Papanikolaou, N. V. Tkachenko, *Phys. Chem. Chem. Phys.* 15 (2013) 13128.
- [167] S. J. Strickler, R. A. Berg, *J. Chem. Phys.* 37 (1962) 814.
- [168] A. F. Rausch, U. V. Monkowius, M. Zabel, H. Yersin, *Inorg. Chem.* 49 (2010) 7818.
- [169] D. N. Kozhevnikov, V. N. Kozhevnikov, M. M. Ustinova, A. Santoro, D. W. Bruce, B. König, R. Czerwieniec, T. Fischer, M. Zabel, H. Yersin, *Inorg. Chem.* 48 (2009) 4179.
- [170] T. Fischer, R. Czerwieniec, T. Hofbeck, M. M. Osminina, H. Yersin, *Chem. Phys. Lett.* 486 (2010) 53.
- [171] D. Donges, J. K. Nagle, H. Yersin, *Inorg. Chem.* 36 (1997) 3040.
- [172] W. Humbs, H. Yersin, *Inorg. Chim. Acta* 265 (1997) 139.
- [173] A. Bossi, A. F. Rausch, M. J. Leitzl, R. Czerwieniec, M. Whited, P. Djurovich, H. Yersin, M. E. Thompson, *Inorg. Chem.* 52 (2013) 12403.
- [174] H. Yersin, D. Donges, J. K. Nagle, R. Sittus, M. Glasbeck, *Inorg. Chem.* 39 (2000) 770.
- [175] J. Schmidt, H. Wiedenhofer, A. von Zelevsky, H. Yersin, *J. Phys. Chem.* 99 (1995) 226.
- [176] H. Yersin, W. Humbs, J. Strasser, *Coord. Chem. Rev.* 159 (1997) 325.
- [177] W. Humbs, H. Yersin, *Inorg. Chem.* 35 (1996) 2220.
- [178] W. J. Finkenzeller, P. Stöbel, H. Yersin, *Chem. Phys. Lett.* 397 (2004) 289.
- [179] R. Czerwieniec, W. J. Finkenzeller, T. Hofbeck, A. Starukhin, A. Wedel, H. Yersin, *Chem. Phys. Lett.* 468 (2009) 205.
- [180] H. Yersin, J. Strasser, *Coord. Chem. Rev.* 208 (2000) 331.

- 
- [181] H. Yersin, W. Humbs, J. Strasser, *Top. Curr. Chem.* 191 (1997) 153.
- [182] D. S. Tinti, M. A. El-Sayed, *J. Chem. Phys.* 54 (1971) 2529.
- [183] H. Yersin, W. J. Finkenzeller, in H. Yersin (Ed.), *Highly Efficient OLEDs with Phosphorescent Materials*, Wiley-VCH, Weinheim, 2008, p. 1.
- [184] A. F. Rausch, H. H. H. Homeier, P. I. Djurovich, M. E. Thompson, H. Yersin, *Proc. of SPIE*, 6655 (2007) 66550F-1.
- [185] G. Blasse, D. R. McMillin, *Chem. Phys. Lett.* 70 (1980) 1.
- [186] J. R. Kirchhoff, R. E. Gamache, Jr., M. W. Blaskie, A. A. Del Paggio, R. K. Lengel, D. R. McMillin, *Inorg. Chem.* 22 (1983) 2380.
- [187] M. A. El-Sayed, *J. Chem. Phys.* 38 (1963) 2834.
- [188] T. Azumi, H. Miki, *Top. Curr. Chem.* 191 (1997) 1.
- [189] H. Miki, M. Shimada, T. Azumi, J. A. Brozik, G. A. Crosby, *J. Phys. Chem.* 97 (1993) 11175.
- [190] S. Kimachi, R. Satomi, H. Miki, K. Maeda, T. Azumi, *J. Phys. Chem. A* 101 (1997) 345.
- [191] S. Obara, M. Itabashi, F. Okuda, S. Tamaki, Y. Tanabe, Y. Ishii, K. Nozaki, M.-A. Haga, *Inorg. Chem.* 45 (2006) 8907.
- [192] Z. A. Siddique, T. Ohno, K. Nozaki, T. Tsubomura, *Inorg. Chem.* 43 (2004) 663.
- [193] P. Coppens, J. Sokolow, E. Trzop, A. Makal, Y. Chen, *J. Phys. Chem. Lett.* 4 (2013) 579.
- [194] A. F. Rausch, M. E. Thompson, H. Yersin, *Chem. Phys. Lett.* 468 (2009) 46.
- [195] W. J. Finkenzeller, T. Hofbeck, M. E. Thompson, H. Yersin, *Inorg. Chem.* 46 (2007) 5076.
- [196] A. Rausch, M. E. Thompson, H. Yersin, *J. Phys. Chem. A* 113 (2009) 5927.
- [197] H. Wiedenhofer, S. Schützenmeier, A. von Zelewsky, H. Yersin, *J. Phys. Chem.* 99 (1995) 13385.
- [198] R. Czerwieńiec, T. Hofbeck, O. Crespo, A. Laguna, M. Concepción-Gimeno, H. Yersin, *Inorg. Chem.* 49 (2010) 3764.
- [199] J. Föllner, M. Kleinschmidt, C. M. Marian (2016) *submitted*.
- [200] J. L. McHale. *Molecular Spectroscopy*. Prentice-Hall, Upper Saddle River, NJ, 1999.
- [201] T. J. Penfold, *J. Phys. Chem. C* 119 (2015), 13535–13544
- [202] P. Day, N. Sanders, *J. Chem. Soc. A* (1967) 1536.
- [203] C. C. Phifer, D. R. McMillin, *Inorg. Chem.*, 25 (1986) 1330.
- [204] M. J. Leitl, PhD. Thesis: Photophysical characterizations of OLED relevant Cu(I) complexes exhibiting thermally activated delayed fluorescence (TADF). Universität Regensburg (2015).
- [205] A. Jesser, M. Rohrmüller, W. G. Schmidt, *J. Comput. Chem.* 35 (2014) 1.
- [206] T. A. Niehaus, T. Hofbeck, H. Yersin, *RSC Adv.* 5 (2015) 63318.
- [207] S. P. McGlynn, T. Azumi, M. Kinoshita, *Molecular Spectroscopy of the Triplet State*, Prentice-Hall, Englewood Cliffs, NJ, 1969.
- [208] A. Schinabeck, M. J. Leitl, D. M. Zink, T. Baumann, H. Yersin, *manuscript in preparation*
- [209] F. Franco de Carvalho, I. Tavernelli, *J. Chem. Phys.* 143 (2015) 224105.
- [210] M. Kleinschmidt, C. van Wüllen, C. M. Marian, *J. Chem. Phys.* 142 (2015) 094301.
- [211] R. Heydová, E. Gindensperger, R. Romano, J. Sýkora, A. Vlček, Jr., S. Zališ, C. Daniel, *J. Phys. Chem. A* 116 (2012) 11319.
- [212] Y. Harabuchi, J. Eng, E. Gindensperger, T. Taketsugu, S. Maeda, C. Daniel, *J. Chem. Theory Comput.* (2016) DOI: 10.1021/acs.jctc.6b00080.
- [213] C. Gourlaouen, C. Daniel, *Dalton Trans.* 43 (2014) 17806.